LBL--14864

DE83 000519

TWO-PION CORRELATIONS IN HEAVY ION COLLISIONS

William Allen Zajc

Ph.D. Thesis

August 1982

Nuclear Science Division
Lawrence Berkeley Laboratory
University of California
Berkeley, CA 94720

This work was supported by the Director, Office of Energy Research, Division of Nuclear Physics of the Office of High Energy and Nuclear Physics of the U.S. Department of Energy under Contract DE-AC03-76SF00098.

TABLE OF CONTENTS

	ABSTRACT	v
	ACKNOWLEDGEMENTS	vii
I.	INTRODUCTION	1
	A. Objectives of Relativistic Heavy Ion Physics	1
	B. The Pion Source in RHIC	3
	C. Organization of this Thesis	4
II.	INTENSITY INTERFEROMETRY	5
	A. Introduction	5
	B. The Origins of Bose-Einstein Statistics	5
	C. The Work of Hanbury-Brown--Twiss	11
	D. Intensity Interferometry in Particle Physics	18
III.	EXPERIMENTAL APPARATUS	27
	A. Beam Transport and Monitoring	27
	B. The Spectrometer	29
	1. The JANUS Magnet	29
	2. Scintillation Counters	30
	3. Multi-wire Proportional Chambers	31
	C. Fast Electronics	31
IV.	DATA ANALYSIS	34
	A. First Pass: Effective Edge Approximation	35
	B. Second Pass: Chebyshev Parametrization	38
	1. Discussion of the Method	38
	2. Results of Chebyshev Parametrization	40
	3. Final Event Selection	44

IV. DATA ANALYSIS (Continued) .....

C. Third Pass: Generation of the Correlation Function .. 46

D. Fourth Pass: Fitting the Correlation Function 55

V. RESULTS 60

A. Single Particle Spectra 60

B. Two Pion Data 66

1. Orientation 66

2. Results of the Fitting Procedure 68

3. Discussion of the Source Sizes 74

4. Implications for Coherence 78

VI. CONCLUSIONS AND FUTURE RESEARCH 80

Appendix A: IONIZATION CHAMBER CALIBRATION 82

Appendix B: TRACKING METHODS 84

Appendix C: MONTE CARLO METHODS 88

Appendix D: MEAN MULTIPLICITY DISTRIBUTIONS 96

Appendix E: BACKGROUND FLUCTUATIONS 101

Appendix F: GAMOW COULOMB CORRECTIONS 108

Appendix G: THE INTERPRETATION OF GAUSSIAN SOURCE PARAMETERS . 113

REFERENCES 117

FIGURE CAPTIONS 127

FIGURES 131

TWO-PION CORRELATIONS IN HEAVY ION COLLISIONS

by

William Allen Zajc

ABSTRACT

An application of intensity interferometry to relativistic heavy ion collisions is reported. Specifically, the correlation between two like-charged pions is used to study the reactions Ar+KCl$\rightarrow 2\pi^{\pm}$ +X and Ne+NaF$\rightarrow 2\pi^{-}$ +X. Source sizes are obtained that are consistent with a simple geometric interpretation. Lifetimes are less well determined but are indicative of a faster pion production process than predicted by Monte Carlo cascade calculations. There appears to be a substantial coherent component of the pion source, although measurement is complicated by the presence of final state interactions.

Additionally, the generation of spectra of uncorrelated events is discussed. In particular, the influence of the correlation function on the background spectrum is analyzed, and a prescription for removal of this influence is given. A formulation to describe the statistical errors in the background is also presented.

Finally, drawing from the available literature, a self-contained introduction to Bose-Einstein correlations and the Hanbury-Brown--

Twiss effect is provided, with an emphasis on points of contact between classical and quantum mechanical descriptions.

ACKNOWLEDGEMENTS

To paraphrase H. F. Judson, author of The Eighth Day of Creation, "Intellectual debts differ from all others, in that they are a pleasure to acknowledge." Having accumulated a large number of debts, intellectual and otherwise, I feel particularly well qualified to testify as to the accuracy of this statement. Since the work that follows is lengthy, I've deliberately placed the acknowledgements at the beginning of this thesis. Thus, if the reader tires quickly, he will still be aware of those who have made this work possible.

All of the following have contributed in some fashion to the experiments discussed here: J.A. Bistirlich, R.J. Bossingham, H.R. Bowman, C.W. Clawson, K.M. Crowe, K.A. Frankel, O. Hashimoto, J.G. Ingersoll, M. Koike, J.P. Kurck, W.J. McDonald, C.J. Martoff, J.P. Miller, D.J. Murphy, J.O. Rasmussen, J.P. Sullivan, P.T. Truöl, and E. Yoo. They represent the collective "we" used in the remainder of this thesis. However, any mistakes in presentation or interpretation of the data are mine alone.

I would now like to expand on contributions that might be categorized as above and beyond the call of duty:

First, Jim Bistirlich has been an invaluable source of wire-chamber expertise for this and many other experiments. In addition, much of the mechanical engineering necessary for this experiment has been performed under his supervision. I would also like to thank Jim

for many interesting conversations concerning data analysis and other matters.

Thanks go to Osamu Hashimoto, who performed the disagreeable but essential task of producing magnetic field data from the output tapes of the magnetic mapper. Further work along these lines was conducted by Jim Kurck, who provided a valuable set of programs for manipulating the resulting data files. The analysis code for the first pass through the data tapes was largely the work of Jim Miller. Although there are depths of these programs best left unplumbed, I would have been lost without them. While on the subject of programming assistance, I would like to thank Dean Chacon for his work on graphics and fitting routines.

A truly impressive amount of work was performed by John Sullivan, who maintained and developed the on-line acquisition programs for this experiment, often bringing order to chaos in the process.

Carl Clawson played an essential role in explaining the mysteries of UNIX to me. He gladly provided me in minutes with what would have taken me days to find out on my own, or weeks with the help of the consultants.

Peter Truoi regularly showed me how much one can accomplish through a combination of insight and hard work. More than once he rescued this project from some foolish mistake I was intent on elevating to new physics. Peter also developed and maintained the fast electronics during the data-taking.

Nearly all of the computations reported here were performed without charge on the HISS VAX, the use of which is gratefully acknowledged. In particular, I wish to thank Mark Bronson, Chuck McParland, and Jack Engelage.

I would like to thank Miklos Gyulassy for directing our attention to the potential of two-pion correlations for heavy ion physics. Valuable conversations with R. Glauber, S. Koonin, A. Pais, J. Polchinski Sr., and E. Purcell are also gratefully acknowledged.

The members of my thesis committee have played an important role, not only in this thesis, but in my development as a physicist. Owen Chamberlain has taught me that there is a simple explanation for everything, and that the job of a physicist is to know it. John Rasmussen has been a continual source of new ideas, and by example has shown me the importance of imagination in doing science. Finally, Ken Crowe has shown me, again by example, that nothing gets done without determination, and a lot of it. Ken has been the driving force behind this work, as well as behind my transformation from a directionless second-year graduate student to an experimental physicist.

I would also like to thank my fellow graduate students, mentioned above, for those occasions where drinking beer and bemoaning the life of a student were the only entertainment. Veterans of this include Jeff Martoff, Carl Clawson, Roy Bossingham, Jim Kurck, and John Sullivan. (In this matter, Jim Miller is an honorary graduate student.)

None of this work, nor my higher education, would have been possible without the continual support of my parents, Norbert and Daphne Zajc. During my years at home, they always provided an atmosphere conducive to learning; during my long years away from home their faith in me was a source of strength.

Finally, it is very certain that I never would have started on my research career were it not for my wife Cynthia. Among the many other extraordinarily valuable things she has contributed to my life, it was at her instigation that we obtained our dog Meatball, who was essential to me in finishing this work. It is to them that this thesis is dedicated.

This work was supported by the Director, Office of Energy Research, Division of Nuclear Physics of the Office of High Energy and Nuclear Physics of the U.S. Department of Energy under Contract DE-AC03-76SF00098.

CHAPTER I

INTRODUCTION

A. Objectives of Relativistic Heavy Ion Physics

The systematic study of relativistic heavy ion collisions (RHIC) became possible in 1974, with the advent of the Berkeley Bevalac. Prior to this, cosmic rays provided the only source of relativistic nuclei, which made experimental control of the energy and mass of the projectile impossible. The Bevalac provided experimenters with beams up to A = 57, with energies ranging from 50-2100 A·MeV.

It was expected that a number of unusual phenomena could be observed with this new facility. For example, the first three papers of the High Energy Heavy Ion Summer Study of 1974[1] discuss shock waves, highly excited nuclear matter, and density isomers. It was also hoped that one could determine the nuclear equation of state, thereby obtaining the energy per nucleon $W(\rho,T)$ for densities ρ exceeding normal nuclear density and for temperatures $T>0$. In addition to the intrinsic interest in $W(\rho,T)$, knowledge of this quantity is essential to theoretical studies of supernovae and neutron stars. Further practical benefits were predicted for such fields as cosmic rays (of course), atomic physics at high Z, creation of neutron rich isotopes, etc.

In the ensuing years of experimentation and theoretical study, many of these practical results have indeed been obtained. However,

the search for exotic physics has been largely unrewarded. Single-particle spectra of all reaction products are smoothly varying, with the exception of the well-understood Coulomb enhancement of π^- yield observed near beam velocity by Sullivan et al.[2] Determination of the nuclear equation of state has thus far proved impossible, due to finite particle effects, incomplete equilibration, large single-scattering components, etc. Furthermore, vastly different assumptions regarding the reaction dynamics lead to quite similar final states, thus allowing a variety of models to predict single-particle cross-sections to within a factor of two. As emphasized in a recent review by Nagamiya and Gyulassy,[3] the actual physics for single-particle observables lies in understanding and reducing this factor of two.

An alternative (and complementary) approach to the refinement of existing single-particle measurements is the study of multi-particle spectra and correlations. For example, the in-plane/out-of-plane two-proton correlation has proven valuable in resolving the various processes that produce protons in a given phase space region.[4] Other forms of two-proton analysis may probe the size and shape of the mid-rapidity proton source.[5,6] The ultimate limit of multi-particle measurements is the global analysis of all (charged) particles. For instance, the authors of Ref. 7 show that the eigenvalues of the kinetic flow tensor

$$F_{ij} = \sum_{\beta} \frac{1}{2m_{\beta}} p_i(\beta) \cdot p_j(\beta)$$

are useful parameters to describe the flow patterns of heavy-ion

collisions. (Here m_β and $p_i(\beta)$ are the mass and i-th momentum component, respectively, of the β-th particle.)

A particularly interesting two-particle state is that for two like-charged pions. Because two like pions obey Bose statistics, the two-pion relative momentum spectrum provides a sensitive tool for exploring the properties of the pion source. This thesis describes a series of experiments designed to determine the pion source parameters through the use of intensity interferometry. In the next section, we begin by considering the pion production mechanism in RHIC.

B. The Pion Source in RHIC

Pion production in relativistic heavy ion collisions has been extensively studied, both experimentally and theoretically. (See Ref. 3 and the papers cited therein.) There are several reasons for this attention. First, pions are produced in abundance at RHIC energies (0.5-2.1 A·GeV). For example, at 1.8 A·GeV, nearly 60% of the NN total cross section goes into pion production. Secondly, both pion production via the dominant (resonant) reaction $NN \rightarrow N\Delta$ and the pion-nucleon interaction $\pi N \rightarrow \pi N$ are well understood at a (nearly) fundamental level. Furthermore, the σ-model, a phenomenological prescription for incorporating the effects of higher-order meson exchange and chiral invariance, has led to the prediction of novel states of nuclear matter,[8] and of the pion field (See, e.g., the results of Ref. 9) Finally, since $m_\pi << m_N$, and since pions are bosons, one is led to consider the possibility of coherent pion radiation,[10] i.e., the creation of a "classical" pion field through

bremmstrahlung of the nucleons. This would be an interesting object indeed! Since two-pion interferometry is capable of measuring both the space-time extent of pion production and the degree of coherence of the pion field, it is a valuable method for clarifying pion production processes in RHIC.

C. Organization of this Thesis

Chapter II contains an explication of intensity interferometry. Since this technique is often "explained" by reference to the Hanbury-Brown--Twiss effect, and since the HBT effect itself is often the subject of considerable confusion, a fairly extensive discussion is devoted to the origins of the Bose-Einstein interference and to classical explanations of the HBT effect, as well as its application to particle physics. Chapter III describes the experimental apparatus used to measure our two-pion events, while Chapter IV details the analysis of these data. Results are presented in Chapter V, with conclusions and directions for future research given in Chapter VI. There are several appendices containing detailed descriptions of various results, methods, and calculations.

Unless otherwise noted, natural units are used in this work, that is, $\hbar=c=1$.

CHAPTER II

INTENSITY INTERFEROMETRY

A. Introduction

Intensity interferometry uses the correlations between identical particles (usually bosons) to determine properties of the particle source and/or emission process. In optics, this technique is often referred to as the Hanbury-Brown--Twiss (HBT) effect; in particle physics it is known as the Goldhaber-Goldhaber-Lee-Pais (GGLP) effect. This chapter is intended to provide a roughly (but not rigorously) historical introduction to these methods by emphasizing the physical origins of like-particle interference.

We begin by considering intensity fluctuations since the need for Bose-Einstein statistics (it and Fermi-Dirac statistics are the ultimate source of all multi-particle interference phenomena) first arose from such considerations. Much of the next section is taken directly from the excellent article by A. Pais[11] entitled "Einstein and the Quantum Theory."

B. The Origins of Bose-Einstein Statistics

Note: this section uses units such that $\hbar$ and c appear explicitly.

The systematic study of fluctuation phenomena in statistical mechanics was pioneered by Einstein. In 1904, he applied his result

for the mean-square fluctuation in energy

$$\left\langle (\Delta E)^2 \right\rangle = kT^2 \frac{\partial E}{\partial T} \qquad \text{(II.1)}$$

to the total energy of a blackbody oven at temperature T with volume V,

$$E(T) = V\int p(\nu,T)d\nu = 4\sigma T^4 V \quad , \qquad \text{(II.2)}$$

to obtain

$$\left\langle (\Delta E)^2 \right\rangle = 16k\sigma VT^5 \quad . \qquad \text{(II.3)}$$

(Here σ is the Stefan-Boltzmann constant.) The meaning of this result becomes apparent when we use Wien's displacement law $hc/\lambda_{max} = \eta kT$; $\eta \sim 2.8$, to express ξ, the relative energy fluctuations, in terms of λ_{max}, the most probable wave-length in the blackbody spectrum:

$$\xi = \frac{\left\langle (\Delta E)^2 \right\rangle}{(E(T))^2} = \frac{60\eta^3}{8\pi^5} \cdot \frac{\lambda_{max}^3}{V} \sim \frac{1}{2} \cdot \frac{\lambda_{max}^3}{V} \qquad \text{(II.4)}$$

Thus, for small T, it is possible for ξ to be arbitrarily large. This should be contrasted with the case for an ideal (classical) gas of N particles, where $E(T) = \frac{3}{2}NkT$ implies $\xi = \frac{2}{3N} \sim O(\frac{1}{N})$, independent of temperature. As one might guess from the presence of λ_{max} in Eq. II.4, the large fluctuations for the blackbody results from the wave nature of the photons. This may not appear suprising until one recalls that the usual derivation of the Planck's law requires attributing particle-like properties to the radiation field. This, one of the first hints at complementarity, was further elucidated in 1909 by Einstein, again by considering the fluctuations of blackbody radiation. This time he restricted the analysis to the fluctuations of

the energy density $\rho(\nu,T)vd\nu$ within a small sub-volume v and frequency interval ν. Here we present a slightly simplified argument by examining the mean-square dispersion in photon number for <u>one</u> cavity mode k. In equilibrium we have

$$\bar{n}_k = \frac{1}{\exp(\frac{\epsilon}{kT}) - 1} \tag{II.5}$$

where $\epsilon = h\nu_k$. One may then readily calculate $\langle(\Delta n_k)^2\rangle$, either by relating $\bar{n}_k$ to the mean energy of the mode and using eqn II.1 or by explicitly calculating

$$\langle(\Delta n_k)^2\rangle = \langle n_k^2\rangle - \bar{n}_k^2$$

for a quantized oscillator. In either case, one obtains

$$\langle(\Delta n_k)^2\rangle = \bar{n}_k + \bar{n}_k^2 \tag{II.5}$$

which is the essential result of this section.

As we shall see, the two terms on the RHS of Eqn. II.6 reflect the particle and wave aspects, respectively, of photon number fluctuations. The first term is precisely what one would obtain from a distribution of classical particles with mean $\bar{n}$ obeying Poisson statistics, i.e., $\langle(\Delta n)^2\rangle = \bar{n}$. The second term, $\bar{n}^2$, is proportional to the number density squared and thus is an interference term, as expected from a wave interpretation.[12]

While we have derived this result for blackbody radiation, the form is a general one. To see how it arises in a different context, consider a phototube with efficiency ξ illuminated by a light beam of

fixed (for now) intensity I. The mean number of counts n in an interval T is then $n = \xi IT$. Since we have somehow fixed the intensity, n is constant in time, so the distribution of actual counts m detected in time T is given by a Poisson distribution:

$$P(m|n) = \frac{(n)^m}{m!} e^{-n}.$$

In practice, however, one (usually) finds that the intensity I, and thus n, are themselves fluctuating quantities. Thus to find the total dispersion in the number of counts m, we must also average over the distribution of n's. Denoting such double averaging by $\langle\langle \ldots \rangle\rangle$, and using the results for the first two moments of a Poisson distribution with fixed n, viz. $\langle m \rangle = n$, and $\langle m^2 \rangle = n^2 + n$, we obtain

$$\begin{aligned} \langle\langle (\Delta m)^2 \rangle\rangle &= \langle\langle m^2 \rangle\rangle - \langle\langle m \rangle\rangle^2 \\ &= \langle n^2 + n \rangle - \langle n \rangle^2 \\ &= \bar{n} + \left[\overline{n^2} - \bar{n}^2 \right], \end{aligned} \tag{II.7}$$

where a bar indicates the result of averaging over the distribution of n. Rewriting in terms of intensity, this result is

$$\overline{(\Delta m)^2} = \bar{n} + \xi^2 T^2 \left[\langle I^2(t) \rangle - \bar{I}^2 \right] \tag{II.8}$$

Thus far, the only content of Eqns. II.7 and II.8 is mathematical; they simply reflect the results of performing a double average. We now introduce the physics of the argument by exploring the origin of the intensity fluctuations. First note that if I(t) is

produced by the output of one oscillator,

$$I(t) = \tfrac{1}{2}\epsilon_0 c \left| E_0 e^{(i\omega_0 t + i\phi(t))} \right|^2 ,$$

then, regardless of the variation of the $\phi(t)$, the intensity is fixed, $\langle I^2(t) \rangle = \bar{I}^2$, and we recover the counting statistics of a simple Poisson. This is not an artificial example, e.g., a gain-stabilized laser is well approximated by such a description. If, however, I(t) is formed by the superposition of many sources j

$$I(t) = \tfrac{1}{2}\epsilon_0 c \left| \sum_{j=1}^{j=N} E_0 e^{(i\omega_0 t + i\phi_j(t))} \right|^2 , \qquad \text{(II.9)}$$

and if the ϕ_j's are time-varying in a mutually incoherent fashion (as in collision broadening, for example), then the relative phases add in random walk fashion, there are large fluctuations in intensity (over the time scale of the ϕ_j's variation), and one can easily show[13] that $\langle I^k(t) \rangle = k! \cdot \bar{I}^k$. In this case, we have $(\Delta m)^2 = \bar{n} + \bar{n}^2$, in accord with Eqn. II.6. Since this limit depends essentially on the linear addition of the electric fields, the use of the expression 'wave noise' for the second term is justified.

We now return to our chronological development. In 1924, Bose showed that eqn. II.5 could be derived through the machinery of conventional statistical mechanics, provided one regarded the photons as indistinguishable particles. In the same year, Einstein boldly extended Bose's result to the molecular gas, by using the density of states appropriate for massive (non-relativistic) particles and

requiring particle conservation. He showed in 1925[14] that these modifications did not affect the (particle + wave) form of the fluctuations. Therefore, he concluded that this must

> express indirectly a certain hypothesis on a mutual influence of the molecules which for the time being is of a quite mysterious nature...
>
> One can interpret part of the fluctuations in an analogous way by attributing to a gas some kind of radiation in a suitable way, and by calculating the interference fluctuations. I go into further details because I believe that this is more than an analogy.
>
> Mr. L. de Broglie has shown, in a very remarkable thesis, how one can attribute a wave field to a material particle...

Thus, for Einstein, Bose statistics implied wave mechanics, not vice versa.

It is natural to ask "Why did Einstein not discover the HBT effect?" (Here HBT effect is defined as the use of photon fluctuations in a light beam to determine the size of the source.) Einstein was obviously intimately acquainted with all details of photon fluctuation phenomena. In addition, much of his later life was devoted to pondering the apparent paradoxes of quantum theory; the interference of photons produced from opposite sides of a star is a (less subtle) cousin to the Einstein-Podolsky-Rosen paradox. Of course, this is the sort of question that will never be definitively answered. One response,[15] however, that is certainly consistent with all known facts, is that Einstein was indeed aware of the HBT effect but regarded it as a trivial consequence of photon statistics.

C. The Work of Hanbury-Brown--Twiss

This section describes the application of intensity interferometry to astronomy, as pioneered by Hanbury-Brown and Twiss. Also in this section we present a derivation of the HBT result based solely on classical considerations, as well as an argument by Purcell that clarifies the role of photon counting in the HBT effect. An extensive (and very readable) account of the HBT technique may be found in The Intensity Interferometer by Hanbury Brown.[16]

In 1949, Hanbury Brown, Jennison, and Das Gupta[17] measured the angular size of the radio sources Cygnus A and Cassiopeia A by comparing the noise correlations between two separated antennas. Since this method was based on firmly established radio frequency techniques (the theory of bandwidth-limited Gaussian noise as detected by a square-law detector, see, e.g. Lawson and Uhlenbeck[18]), their result occasioned little controversy. The extension of these methods to the optical domain, however, was quite a different matter.

The following objections (among others) were raised: 1.) In his quantum mechanics text[19] Dirac states "Interference between two different photons never occurs." 2.) Two laboratory experiments had been performed that failed to observe correlations in the photon count rate.[20,21] 3.) For optical frequencies, the shot noise (i.e., the particle-like photon number fluctuations) would far exceed the wave noise. In the radio source case, the wave noise is the greater of the two, and indeed is solely responsible for the noise correlations.

It is instructive to examine these objections point by point. The first criticism simply results from quoting out of context. Dirac made this statement with reference to double-slit photon diffraction experiments, to refute the erroneous interpretation that diffraction results from the interference of two photon "waves". In fact, the diffraction persists to intensities so low that the chance of finding two photons simultaneously in the apparatus is negligible.[22]

The second objection would appear to be more substantial, based as it is on physical evidence. Here the fault is not a conceptual one, rather it is an experimental one. While the data as reported by these experiments are correct, it is possible to show (see, e.g. Purcell[23]) from the stated values of the resolving time and bandwidth (for both experiments), that their sensitivity is such that hundreds of years of observation time would be required to see the HBT enhancement.

The third point is a real one, although again it is dispensed with through suitable design of the measuring apparatus. It is certainly true that for visible light the shot noise is the dominant source of fluctuations. The "trick" lies in the construction of a detector that is sensitive only to the wave noise; this is precisely what Hanbury Brown and Twiss did.

Finally, one might attempt to meet all objections of principle by the following reasoning (an argument by intimidation): First, the existence of noise correlations was established beyond doubt at radio

frequencies. To apply the technique to electromagnetic radiation at other frequencies (higher or lower) we simply note that, according to Bohr,[24]

> The typical features of electromagnetic fields do not depend on scale, since the two fundamental constants- the velocity of light c and the quantum of action h- do not allow any fixation of quantities of dimensions of a length or time interval.
>
> (Emphasis added)

We now turn to a classical analysis of an idealized HBT experiment, as given by Hanbury Brown.[16] Consider the situation shown in Fig. 1, where two sources P1 and P2 are separated by a distance 2R. They may be regarded, for instance, as two atoms emitting light on opposite limbs of a star, radiating with frequencies ω_1 and ω_2, and with random phases ϕ_1 and ϕ_2, respectively. The light in each arm of the detector first passes through a polarizer, so that we may add the electric fields algebraically, not vectorially. This is simply for mathematical convenience. It next strikes an optical filter such that the light that is transmitted satisfies $\omega_1 \cong \omega_2 \cong \omega$; the degree to which this condition is satisfied determines the spectrum of beat frequencies that our system must be capable of measuring. Assume that the sum of their signals is detected at both points A and B; both detectors are assumed to give an output proportional to the local intensity of radiation, i.e., proportional to the square of the electric field. (A phototube has this property.) The output of each detector is passed through the low-pass filters f_i; as we shall see,

these filters must be designed to pass frequencies in the typical range of $\omega_1 - \omega_2$ while rejecting both dc and high frequencies $\geq \omega$. The photocurrent at A is then given by

$$i_A = K_A\left[E_1\sin(\omega_1 t_{A1}+\phi_1) + E_2\sin(\omega_2 t_{A2}+\phi_2)\right]^2 \quad , \qquad \text{(II.10)}$$

where K_A is some constant of proportionality incorporating all relevant detector properties. Similarly,

$$i_B = K_B\left[E_1\sin(\omega_1 t_{B1}+\phi_1) + E_2\sin(\omega_2 t_{B2}+\phi_2)\right]^2$$

Writing $\omega_1 t_{A1}+\phi_1 \equiv A1$, and so on, we may write i_A as

$$\begin{aligned} i_A &= K_A\left[E_1^2\sin^2(A1) + 2E_1E_2\sin(A1)\sin(A2) + E_2^2\sin^2(A2)\right] \qquad \text{(II.11)} \\ &= K_A\Big\{ E_1^2\sin^2(A1) + E_1E_2\left[\cos(A1-A2) - \cos(A1+A2)\right] + E_2^2\sin^2(A2) \Big\} \\ &= \tfrac{1}{2}K_A\Big\{ (E_1^2+E_2^2) - E_1^2\cos^2(2A1) - E_2^2\cos^2(2A2) - 2E_1E_2\cos(A1+A2) \\ &\qquad + 2E_1E_2\cos(A1-A2) \Big\} \end{aligned}$$

This result contains five terms. The first is just the average dc current from the two sources in the absence of interference. The filter f can easily be designed so that this current is not passed. The next three terms oscillate at the sum frequencies of the two sources and thus are of order 2ω; a low pass filter will remove them. The remaining term is the output current of f, denoted $f(i_A)$; it has

a time dependence $\sim \omega_1 - \omega_2$ and thus may be regarded as a slowly varying beat frequency. A similar expression is obtained for $f(i_B)$ by letting A→B everywhere.

The key insight of Hanbury Brown and Twiss was to form the product of $f(i_A)$ and $f(i_B)$ in a correlator C, before performing any further data processing. The correlator C produces an output signal proportional to the product of the two input currents. Therefore,

$$i_C = f(i_A)\cdot f(i_B) \tag{II.12}$$

$$= K_A K_B E_1^2 E_2^2 \left[\cos(A1-A2)\cdot\cos(B1-B2)\right]$$

$$= K_A K_B E_1^2 E_2^2 \left\{ \cos\left[(A1-A2) + (B1-B2)\right] + \cos\left[(A1-A2) - (B1-B2)\right]\right\}$$

Expanding the arguments of the cosines,

$$(A1-A2) \pm (B1-B2) = \omega_1(t_{A1} \pm t_{B1}) - \omega_2(t_{A2} \pm t_{B2}) + \left[(\phi_1-\phi_2) \pm (\phi_1-\phi_2)\right] \tag{II.13}$$

Since the sources 1 and 2 are assumed independent, ϕ_1 and ϕ_2 are mutually random variables, so that an ensemble average over terms linearly proportional to them gives no contribution. Therefore, the first term in eqn II.10, which from the results of eqn. II.11 contains a cosine of $\phi_1-\phi_2$, must vanish over long observation times. On the other hand, the second term is independent of the phases! Thus,

the time-averaged i_C is proportional to only this last term:

$$i_C = K_A K_B E_1^2 E_2^2 \cos\left[\omega_1(t_{A1}-t_{B1}) - \omega_2(t_{A2}-t_{B2})\right]. \qquad \text{(II.14)}$$

$$\cong K_A K_B E_1^2 E_2^2 \cos\left\{\omega\left[(t_{A1}-t_{B1}) - (t_{A2}-t_{B2})\right]\right\}$$

Specializing for convenience to the specific geometry illustrated in Fig. 1, where A is on a line perpendicular to the line joining P1 and P2, and B is slightly displaced parallel to the same line, we find for the quantity in square brackets above (the difference of the differences in path length)

$$\left[(t_{A1}-t_{B1}) - (t_{A2}-t_{B2})\right] = \left[(t_{A1}-t_{A2}) - (t_{B1}-t_{B2})\right] \qquad \text{(II.15)}$$

$$= \left\{(\quad 0 \quad) - \left[\sqrt{D^2+(d-R)^2} - \sqrt{D^2+(d+R)^2}\right]\right\}$$

$$\cong 2R\frac{d}{D}$$

Therefore, one can write for the final form of i_C:

$$i_C = K\cos(\omega\frac{2Rd}{D}) = K\cos(2\pi\frac{d\theta}{\lambda}) \qquad \text{(II.16)}$$

That is, the noise in the two channels will be correlated provided $\frac{d\theta}{\lambda} \lesssim 1$, where θ is the angular size of the star. For $\lambda \cong 5000$ Å, this requires d ~ 100 m per msec of arc.

This argument, while straightforward, may be sufficiently complicated algebraically that the physics is no longer manifest. Qualitatively, the HBT effect results as follows: A star consists of a

macroscopically large number N of independent radiators, whose electric fields add linearly. (Eqn II.9 is an example of such a sum.) Since the phases ϕ_i are mutually incoherent, this produces an intensity subject to large fluctuations over time. However, these fluctuations cannot occur over arbitrarily short times. Rather, there exists a time scale given by the inverse bandwidth of the light admitted to our system. (This is true since the bandwidth $\Delta\nu$ determines the range of frequencies that can beat against each other to create a time-varying intensity envelope.) Thus if we measure the noise at time t, then again at time $t + \tau$, it is unlikely to have had changed very much if $\tau < \frac{1}{\Delta\nu}$. Similarly, referring again to Figure 1, if B is sufficiently close to A, the noise profile, created by the sum over the phase of arrival times t_{Bi} for each independent source i, will not be drastically different from the corresponding sum conducted at the point A. Only as d becomes significantly greater then $\frac{D\lambda}{R}$ will the noise at B become different from that at A.

To complete this section, a derivation due to Purcell[23] is given that makes clear the connection between two-channel correlated noise and eqn II.6 of the previous section. We present here a version of this argument specialized to detectors of zero resolving time; again this is for simplicity only. Consider a light beam of one polarization with intensity such that a phototube placed in the beam counts $\bar{n}$ photons per unit time. If the light is from a chaotic source (e.g., a thermal one), the fluctuations in this rate are given by eqn II.6, i.e., $\left\langle (\Delta n)^2 \right\rangle = \bar{n}(1 + \bar{n})$. Split the beam with a half-silvered mirror

so that one beam contains an intensity of $\overline{n_1}$, the other contains $\overline{n_2}$, with $\overline{n} = \overline{n_1} + \overline{n_2}$. The fluctuations in each of the split beams are also governed by eqn II.6 However, we could connect our phototube outputs for 1 and 2 together (count in the OR mode) and demand that we recover the fluctuations resulting from a total of $\overline{n}$ photons. Mathematically,

$$\left\langle (\Delta n)^2 \right\rangle = \overline{n}(1 + \overline{n}) \qquad \text{(II.17)}$$

$$= (\overline{n_1} + \overline{n_2}) + (\overline{n_1} + \overline{n_2})^2$$

but

$$\left\langle (\Delta n)^2 \right\rangle = \left\langle [\Delta(n_1 + n_2)]^2 \right\rangle$$

$$= \left\langle (\Delta n_1)^2 \right\rangle + \left\langle (\Delta n_2)^2 \right\rangle + 2\left\langle \Delta n_1 \cdot \Delta n_2 \right\rangle$$

Substituting $\overline{n_1}(1 + \overline{n_1})$ for n_1's mean-square dispersion, and similarly for n_2's, one obtains:

$$\left\langle \Delta n_1 \cdot \Delta n_2 \right\rangle = \overline{n_1} \cdot \overline{n_2} \qquad \text{(II.18)}$$

Thus, the fluctuation formula for Bose-Einstein statistics leads directly to correlated noise counting rates, without the need for the intermediary classical wave picture.

D. Intensity Interferometry in Particle Physics

This section develops selected aspects of Bose-Einstein statistics as applied to particle physics. This material is intended to be introductory only; most results specific to RHIC are deferred until Chapter Five. Here we will show that correlations between identical

pions are determined by the properties, in particular, the space-time extent, of the pion source, thus providing a strong analogy to the role of photon correlations in the HBT effect. However, while analogous to the HBT technique, in another sense two-pion correlations are complementary, in that the correlations appear in the relative energy-momentum of the detection process, rather than in the distribution in space and time of arrival at the detector positions.[25,26] Similarly, while the derivations of the previous section relied upon either classical wave interference or (non-classical) particle number fluctuations, the approach here will be dominated by quantum mechanical indistinguishability, which in turn implies symmetrization of the wave function. Nevertheless, it should be remembered that these are all different methods of describing the same physical phenomena.

The first application of intensity interferometry to particle physics was made in 1960 by Goldhaber, Goldhaber, Lee, and Pais[27] (GGLP). They studied the distribution of opening angles between pions from the annihilation of 1.05 GeV/c $\bar{p}$'s on protons in a propane bubble chamber. It was found that the mean opening angle for like pion pairs was significantly smaller than that for unlike pion pairs. GGLP explained this in the framework of the Fermi statistical model,[28] with the additional requirement of symmetrization between like particles. To see how this comes about, consider first the expression for the differential cross section $d\sigma$ to produce N particles from a reaction with total four-momentum P_{TOT}:

$$d\sigma = C_N P_N(\Omega) \cdot \prod_{i=1}^{i=N} \left[\frac{V}{(2\pi)^3} \cdot \frac{d^3 p_i}{2E_i} \right] \delta^4 \left(P_{TOT} - \sum_{i=1}^{i=N} p_i \right) \quad . \tag{II.19}$$

Here C_N is a normalization constant, V is the quantization volume, and $p_i = (E_i, \vec{p}_i)$ is the four-momentum of the i-th particle. The product in brackets, along with the delta-function, is simply the available N-body phase space. $P_N(\Omega)$ represents the probability that all N particles are simultaneously in the reaction volume Ω, thus

$$P_N(\Omega) = \int_\Omega \cdots \int_\Omega d\vec{r}_1 \cdots d\vec{r}_N |\Psi_N|^2 \tag{II.20}$$

If one assumes the N particles are statistically independent, the wave function Ψ_N is then the product of plane waves:

$$\Psi_N = \prod_{i=1}^{i=N} \frac{e^{i\vec{p}_i \cdot \vec{r}_i}}{\sqrt{V}}$$

In this case, it is apparent that $P_N(\Omega) = (\Omega/V)^N$. What GGLP showed was that the distribution of pion pair opening angles required modifying Ψ_N by symmetrizing the product wave function between like pion pairs. After doing so, the phase-space integrals were evaluated via Monte-Carlo integration, leading to good agreement with the observed opening angle distributions for values of the reaction volume radius R between $0.5\frac{\hbar}{m_\pi c}$ and $0.75\frac{\hbar}{m_\pi c}$, or roughly between .7 and 1.0 fm. (It is interesting to note that in his 1950 paper,[28] Fermi makes explicit note of neglecting like-particle symmetrization requirements. It does no disservice to the authors of Ref. 27 to suggest that, had the available data warranted such a treatment, Fermi himself may have made a GGLP-style analysis of meson correlations.)

Further $\bar{p}p$ experiments[29-31] at higher energies found radii similar to those obtained by GGLP. Bartke et al.[32] were the first to examine the mean opening angle as a function of the relative momentum between the pions. Again, they found $R \cong 1$ fm, in this case for the reaction $\pi p \rightarrow p 4\pi^+ 3\pi^-$. The extension to hadron-hadron reactions with three and even four identical pions in the final state was performed by Boesebeck et al.[33]

All of the above experiments relied on some variant of a Monte-Carlo integration over the phase space of the N - 2 "other" particles in a N particle event. This procedure becomes increasingly burdensome as the CM-energy, and hence the event multiplicity, increases. One may turn this fault into a virtue by taking the $N \rightarrow \infty$ limit, i.e., by applying the techniques of statistical mechanics. For example, Knox[34] showed that the multiplicity distribution of pions in p+p reactions at 405 GeV is not Poisson, but is well described by assuming the pions form a partially degenerate boson gas. However, precisely because the statistical assumption appears valid, more detailed dynamical information is difficult to obtain by such integral methods.

Fortunately, Kopylov and Podgoretskii, in an extensive series of articles,[35-41] showed that this difficulty may be avoided through use of the two-pion correlation function, roughly defined as

$$C_2(\vec{p}_1,\vec{p}_2) = \frac{\sigma \frac{d^6\sigma}{dp_1^3 dp_2^3}}{\frac{d^3\sigma}{dp_1^3}\frac{d^3\sigma}{dp_2^3}} \qquad \text{(II.21)}$$

Under appropriate conditions, it can be shown that:

$$C_2(\vec{p}_1,\vec{p}_2) = C_2(\vec{q},q_0); \qquad \text{(II.22)}$$

$$\vec{q} = \vec{p}_2 - \vec{p}_1 \quad ,$$

$$q_0 = |E_2 - E_1| \quad ,$$

and that C_2 is proportional to a constant plus the absolute square of the Fourier transform of the space-time distribution of pion sources, i.e.,

$$C_2(\vec{q},q_0) \propto 1 + |\tilde{\rho}(\vec{q},q_0)|^2 \qquad \text{(II.23)}$$

We may understand this result qualitatively by applying the rules of quantum mechanics for indistinguishable events to the experiment illustrated in Fig. 2. Assume that a detector located at $\vec{x}_1$ measures a pion of momentum $\vec{p}_1$ in coincidence with the detection of a pion of momentum $\vec{p}_2$ at location $\vec{x}_2$. (The requirement of a coincidence in time is not needed to insure some condition like $\Delta E \cdot \Delta t \simeq \hbar$. The resolving time must simply be adequate to assure us that the detected pions came from the same nuclear collision, which in turn implies that their wave-packets were once very near each other.) If the source of the pions has some non-zero space-time extent, there are two ways that such a two-pion event may occur: Either a pion with $\vec{p}_1$ was emitted at $\vec{r}_1$ and a pion with $\vec{p}_2$ was

emitted at $\vec{r}_2$, or the pion with $\vec{p}_1$ was emitted at $\vec{r}_2$ while the pion with $\vec{p}_2$ was emitted at $\vec{r}_1$. These two alternative histories of the system are, in general, indistinguishable. Therefore, we must add the amplitudes before squaring the matrix element. Writing $p_i x_j = \vec{p}_i \cdot \vec{x}_j - E_i t_j$, and assuming the pions are described by plane-wave states, the amplitude for a two-pion event is given by:

$$\Psi(\vec{p}_1,\vec{p}_2) \propto \frac{1}{\sqrt{2}}\left\{ e^{ip_1(x_1-r_1)} \cdot e^{ip_2(x_2-r_2)} + e^{ip_1(x_1-r_2)} \cdot e^{ip_2(x_2-r_1)} \right\} \tag{II.24}$$

We note in passing that adding the amplitudes for indistinguishable processes has led us automatically to write a wave function symmetric under the particle interchange $r_1 \leftrightarrow r_2$, thereby making contact with the approach of GGLP. The probability is then proportional to

$$|\Psi(\vec{p}_1,\vec{p}_2)|^2 = 1 + \cos\left[(p_2-p_1)(r_1-r_2)\right] \tag{II.25}$$

Assuming the pion sources act independently, and are distributed in space and time according to a distribution function $\rho(\vec{r},t)$, the result for the two-pion counting rate is found by integrating over the distribution of pion production sites r_1:

$$P(\vec{p}_1,\vec{p}_2) = \int d^4r_1 d^4r_2 \rho(\vec{r}_1,t_1)\rho(\vec{r}_2,t_2)|\Psi(\vec{p}_1,\vec{p}_2)|^2 \tag{II.26}$$

$$= 1 + |\tilde{\rho}(\vec{q},q_0)|^2,$$

where $\tilde{\rho}$, $\vec{q}$, and q_0 are as given above.

As an example, assume the distribution of sources is described by a Gaussian in space and time, that is, $\rho(\vec{r},t) \propto e^{-r^2/R^2 - t^2/\tau^2}$.

The correlation function is then given by

$$C_2(\vec{q},q_0) = 1 + e^{-q^2R^2/2 - q_0^2\tau^2/2} \qquad \text{(II.27)}$$

Thus, for large momentum and/or energy differences, C_2 approaches one. It shows an enhancement for relative momenta $q \simeq \frac{1}{R}$ and for relative energies $q_0 \simeq \frac{1}{\tau}$. It is just when these conditions are satisfied that the Heisenberg relations insure that the alternative propagation paths are truly indistinguishable. This provides another quantum mechanical interpretation of the classical HBT effect, since when (see Eqn. II.16) $\frac{d\theta}{\lambda} \leq 1$ we can no longer tell which photon came from which side of the star. Also note that for any source density function that satisfies

$$\rho_2(\vec{r}_1,t_1;\vec{r}_2,t_2) = \rho(\vec{r}_1,t_1)\cdot\rho(\vec{r}_2,t_2) \qquad \text{(II.28)}$$

with

$$\int \rho(\vec{r},t)d^4r = 1$$

we have $C_2(\vec{q}=0,q_0=0) = 2$, in accord with the general rule that the probability of finding two identical bosons in the same state is twice that for non-identical particles.[42]

Since Kopylov's and Podgoretskii's initial suggestion, correlation function methods have become an accepted if not widespread tool of hadron-hadron physics,[43-53] and recently e^+e^- annihilation,[55] where a 2-pion correlation function has also been measured. Generally, the sizes and lifetimes so obtained are consistent with $R = c\tau = 1$ fm. (See Ref. 56 for a recent review.) In RHIC, both

theoretical[57,58] and experimental[59-62] work indicates that two-pion measurements are capable of providing valuable information about the pion source. This thesis describes the results of such an experiment.

We close this chapter with two observations. First, the results of this section should make it clear that intensity interferometry is not unique to bosons. Had we considered, in the derivation of Eqn II.24, the simultaneous detection of two fermions (in the same spin state), the plus sign in the amplitude would have been replaced by a minus sign in this and the following equations, leading to an anti-correlation at small relative momentum. Such an effect has been predicted[5,63,64] and observed[6] for two protons emitted in heavy ion collisions. In this case, however, the effect of anti-symmetrization is outweighed by the final state coulomb and strong interactions between the two protons. It should also be apparent that correlations between fermions is limited to the particle regime; there are no (macroscopic) fermion "waves" since Fermi statistics prevents the occupation number of any one mode from ever exceeding two (including the spin degeneracy).

As our second observation, we note that the discussion of the properties of $C_2(\vec{q},q_0)$ is a heuristic one in that many potentially complicating factors have been neglected. For instance, the final state interactions between the two pions, and between the pions and the residual matter of the collision, have been neglected.[58] A more fundamental complication is the assumption of statistically indepen-

dent emission of pions by a distributed source. This is clearly an approximation based on the relative scale of the pion wavelength vs. the spatial extent of the source that must be examined case by case. Finally, the fact that pions are bosons implies that it is (in principle) possible to construct states of the field that exhibit classical properties. For example, if the source of the pion field may be treated as c-number, the resulting pion state is a coherent one of indefinite particle number. Such a state would show no GGLP effect, even though the role of Bose-Einstein statistics has been fully incorporated in its construction. (The optical analog of this pion state is the field from a gain-stabilized laser, which was shown in the Section B of this chapter to exhibit classical, not Bose-Einstein, particle-number fluctuations.) Many authors[58,65-70] have examined the possibility of coherence and its experimental signature in two pion interferometry. The interpretation of present evidence, however, is complicated by experimental systematics,[48] and by unobserved dynamic effects,[71] it therefore remains inconclusive.

CHAPTER III

EXPERIMENTAL APPARATUS

The experiments described in this thesis are high-resolution studies of pion correlations from the reactions 1.8 A·GeV $^{40}Ar + KCl \rightarrow 2\pi^{\pm} + X$ and 1.8 A·Gev $^{20}Ne + NaF \rightarrow 2\pi^{-} + X$. We elected to measure pion pairs in a relatively small region of phase space with high statistics and good (absolute and relative) momentum resolution; in this sense our results are complementary to streamer-chamber measurements[59,61] at this energy. In particular, we studied pions emitted near 90 degrees in the center-of-mass, since at this angle the effects of strong and Coulomb interactions with the spectator nuclear matter are most susceptible to analysis.[72] Such pions appear near 40 degrees in the laboratory with momenta peaked about 300 MeV/c. Therefore, they may be momentum analyzed by simple magnetic spectrometer systems. This chapter provides a brief description of the experimental hardware and on-line data acquisition software. The discussion of off-line analysis is presented in Chapter IV.

A. Beam Transport and Monitoring

All measurements were made at the Berkeley Bevalac. Fully stripped 8.5 A·MeV ^{20}Ne or ^{40}Ar from the SuperHILAC are injected into the main ring of the Bevatron, where they are accelerated to 1.8 A·GeV. At this energy, the repetition rate is 10 pulses per

minutes. Following resonant extraction, the beam is transported to our target via a conventional beamline of magnetic dipoles and quadrupoles. The final quads are located approximately 5 meters upstream from the target; typical beam spots are 1 cm. x 1 cm.

The targets are chosen to provide an essentially equal-mass system with respect to the projectile, i.e, a KCl target is used for ^{40}Ar beams and a NaF target for ^{20}Ne beams. The difference between the resulting nuclear systems and the exactly symmetrical case is expected to be small. In particular, pion source size parameters should not be affected since they are determined by geometric, not isotopic, properties. A target thickness between 0.5 and 1.0 gm/cm^2 provides a good compromise between the conflicting requirements of high event rate and low multiple scattering in the target.

The beam intensity is monitored by an ionization chamber located at the end of the vacuum pipe, approximately one meter from our target. The output current is measured by a Ortec 439 current integrator, which converts the ion chamber current to pulses that are read by a CAMAC scaler. The ion chamber calibration is obtained from a fit to all previous measurements by our group and others, performed over a wide variety of energies and intensities. The response is linear and in excellent agreement with the calculated calibration. Further details are presented in Appendix A. Typical intensities range from 10^8 ^{40}Ar per spill to nearly 10^9 ^{20}Ne per spill; a spill is slightly less than one second.

B. The Spectrometer

A plan view of the spectrometer is shown in Fig. 3. Pions produced in the target have their incoming trajectories determined by the two small MWPCs, are bent by the magnetic field, and then pass through the two large MWPCs, thus defining their outgoing trajectories. A lead collimator, 30cm from the beamline and 20cm thick, has an opening angle of 10 degrees, centered about 45 degrees with respect to the beam axis. Due to the target spot size, the range of accepted pion laboratory angles is from 37 degrees to 53 degrees. Immediately following the lead wall are two trigger counters S1 and S2; they provide the START signal for time-of-flight measurements. Behind MWPC4 is an two-layer array of counters, first B1 to B10, followed by A1 to A8. The geometric overlap of A_i with B_j segments the active area of MWPC4 into 17 strips AB_k, $k = 1 \rightarrow 17$. Two-pion events are defined by requiring two separate AB combinations in coincidence; such a coincidence is also the STOP for the time-of-flight. Further details are presented in the "Fast Electronics and Computer" section of this chapter. A cylindrical array of tag counters surrounds the target to provide event-multiplicity information. We now present a more detailed description of the individual components of the spectrometer system.

B.1. The JANUS Magnet

The magnet used (JANUS) is a standard Bevatron H-magnet with a 55.9cm x 167.6cm (22" x 66") pole-tip. The gap is shimmed to 21.5cm to allow insertion of MWPC2 between the pole-tips. All runs were

made with a 9.0 kilogauss field, which corresponds to a current of roughly 500 amperes. The field was measured indirectly by monitoring the voltage drop across a shunt resistor, and directly via a Hall probe located on the bottom pole-tip. The field varied by less than .2% from run to run.

B.2. Scintillation Counters

The active area of S1 was 27cm x 20.3cm, with a thickness of 5 mm. S2 measured 32cm x 15.2cm, with a 7mm thickness. Both were viewed with XP2020 phototubes equipped with active bases designed for high count rate enviroments. Typical counting rates for S1•S2 were a few times 10^5 per second; individual rates, particularly for S1 were even higher.

All AB counters were 5mm thick, with a vertical active height of 30.5cm. Three different widths (33cm, 19.1cm, and 9.5cm) were used to create the staggered hodoscope array as shown in Fig. 3. These counters were equipped with RCA 8575 two-inch phototubes, mounted in the LBL standard base assembly.

The small tag counters T_i, $i = 1 \rightarrow 14$ measure 47cm x 12cm, are 3mm thick, and are mounted in a cylindrical array of radius 30cm just downstream of the target. Each has an angular width of roughly 22.5 degrees so that complete azimuthal coverage would require 16 counters. The two counters in the direction of JANUS are missing, since, if present, the pions accepted in the spectrometer would pass through their additional mass, greatly decreasing our momentum reso-

lution. The T counters use EMI 9843B integral tube and base assemblies. Each set of three T counters is covered by one C counter, with active area 57cm x46cm and thickness 1cm. The C-counters are viewed with RCA 8575 phototubes. 50 mil of copper are placed before the T-counters, and $\frac{1}{8}$" of copper after them, to reduce the background from soft x-rays, heavy fragments, etc.

B.3. Multi-wire Proportional Chambers

The four MWPCs form the heart of the spectrometer, since they provide the spatial information for each pion trajectory. The two small chambers MWPC1 and MWPC2 are identical; each has an active area of 30.2cm x 14.2cm and three planes of sense wires at 45^{o}, 90^{o}, and 0^{o} with respect to the horizontal. Similarly, the two large chambers MWPC3 and MWPC4 are identical; each has an active area of 200cm x 25cm with three planes of sense wires at $+30^{o}$, 90^{o}, and -30^{o} with respect to the horizontal. Aside from the differing sense-plane angles between the small and large MWPCs, the internal details of all four chambers are the same: the sense-planes are separated by 1.4cm, the wire separation is 2mm, and each chamber has an effective mass for multiple scattering of roughly 35 mg/cm^2. All wires are read out with the modular electronics system described in Ref. 73.

C. Fast Electronics

Fig. 4 illustrates the overall flow of control in defining an event. The sequence begins when two pions pass through S1 and S2.

The thresholds on these counters are set to correspond to twice minimum ionizing pions, thus providing a strong bias towards two-pion events. Two signals are taken from S2; the first passes through a high-threshold discriminator $S2_{high}$ to enforce the above requirement; the second fires a low-level discriminator $S2_{low}$ which defines the timing of the coincidence signal $S = S1 \cdot S2_{low} \cdot S2_{high} \cdot (\text{MASTER GATE})$. This process reduces time slewing from pulse-height variation to a minimum. It is important to do so since since S determines the timing of our event.

Each geometrically allowed AB combination is provided with a coincidence circuit. Fig. 4 shows only two of these, $A_i \cdot B_j$ and $A_l \cdot B_m$. In reality, there are 17 such combinations. A majority logic box creates the signal $\prod = (AB)_k \cdot (AB)_n$, $k \neq n$, i.e., $\prod$ means two different elements of the AB array have fired, indicating a pair of pions has successfully traversed the spectrometer. A single-pion trigger is simply set by reducing the majority level requirement to one, so that only one AB-combination is required.

A final requirement for a event is the signal FO = Fast Out from the MWPC's. Due to restrictions in the MWPC electronics, this signal is defined as

$$FO = (f_1+f_2+f_3) \cdot (f_4+f_5+f_6) \cdot f_7 \cdot f_8 \cdot f_9 f_{10} \cdot f_{11} \cdot f_{12}$$

where f_i is the fast out for the i-th plane. (The planes are numbered in the order they are traversed, thus plane #1 is the first plane in MWPC1 while plane #12 is the last plane in MWPC4.) The important point here is that any one of the three planes in MWPC1

(and similarly for MWPC2) is sufficient to (help) create a FO. Therefore, it is imperative that the inefficiencies of these planes be very low to prevent a high trigger rate on useless events.

The event definition is thus EV = S·∏·FO. When this condition is satisfied, A WRITE gate is sent to the MWPC electronics, enabling the read-out of struck wires. A signal is also sent to the CAMAC, initiating the read-out of all TDC, ADC, and pattern word data for that event. Simultaneously, the fast electronics is gated off to prevent further triggers until all data has been read. (This enters the EV definition through S.)

The readout of the CAMAC is controlled by a Micro-programmed Branch Driver (MBD) operating the Los Alamos data acquisition system "Q".[74] The MBD writes the event data into a 800 word buffer of a PDP-11/45. When this buffer is full (typically it contains 3-5 events), the Q system writes it to magnetic tape. The maximum acquisition rate is approximately 200 events per spill due to tape-speed limitations.

CHAPTER IV

DATA ANALYSIS

This chapter contains a step-by-step description of the off-line data analysis procedures. The data written to tape by the on-line data acquisition system pass through four levels of analysis. The first level, performed on the PDP-11 used for data acquisition, selects all reasonable candidates for a n-pion event, where n is greater than or equal to the trigger requirement for that particular run. This process, known as "pruning", writes an output tape which is then analyzed on a VAX system by a second level of routines. At this stage, all good events are found, momentum analyzed, and written to a tertiary file for further processing. This file is then used by the third level of programs to create the correlation function, which in turn is processed by the fourth level of programs to obtain pion source parameters by fitting various distributions to the correlation function so derived.

We now turn to a more detailed examination of each of these steps. Since observation of the Bose-Einstein enhancement depends in an essential fashion on the data analysis, the discussion, particularly for the third level, will be quite extensive. Many of the conclusions presented in the following sections are based on the results of a Monte Carlo written to simulate the spectrometer system. The details of this Monte Carlo code are presented in Appendix C.

A. First Pass: Effective Edge Approximation

Analysis begins by finding all hits in the four MWPC's. Under ideal conditions, a charged particle passing through one of our MWPC's will fire at least one wire in each of the three sense planes. These three wires then form a triangle, localizing the trajectory to 1-2mm. However, operating conditions, particularly for MWPC1 and 2, are far from ideal, in that they are exposed to a flux of charged particles of 10^5-10^6 s^{-1}. The plane-by-plane efficiency is then substantially less than 100%. This fact, combined with the restriction on the Fast Out requirement mentioned in the "Fast Electronics" section of Chapter III, implies that many of our otherwise good two-pion triggers will have only two of three wires present per hit in a given MWPC. It is therefore necessary that all two-wire crossings in the MWPC's also be considered as hits, provided that these crosses are unambiguously determined, i.e., that they are not the vertices of a large triangle.

Once all hits are found, track selection begins by considering all possible ingoing rays to the spectrometer, and all outgoing rays from the spectrometer. An ingoing ray is defined as a combination of any hit in MWPC1 with any hit in MWPC2. Similarly, an outgoing ray is defined as any hit in MWPC3 combined with any hit in MWPC4. The ingoing rays, projected back to the target, are required to originate from within 10cm of the nominal beam-spot location. The outgoing rays are required to have an exit angle less than the minimal entrance angle to the spectrometer, i.e., they must correspond to a

potential trajectory for a charged particle bent in the appropriate direction.

Each ingoing ray is then paired with each outgoing ray to determine if they lie on an allowed trajectory through the magnet. This determination is made using a simple geometric requirement in the effective edge approximation, as described in Appendix B. The effective edge is calculated via three separate prescriptions. The first uses an analytic result[75] for the additional distance beyond the pole-tip edge L_{eff} over which the field is considered constant (See also Figure 6):

$$L_{eff} = \frac{d}{2\pi}\left[2 - \ln\left(\frac{4}{1+s}\right)\right] .$$

In this expression s is a solution to

$$s = \tan\left(s - \frac{\pi h}{d}\right),$$

h is the vertical distance between the pole-tip surface and the center of one of the coils, and d is the gap. The second method of obtaining L_{eff} uses the Monte Carlo to calculate actual trajectories using the full field map. For a track of momentum p, traversing a pole-tip of width 2L with a central field of B_o, the effective edge is then given by

$$2(L + L_{eff}) = \frac{p|\sin\theta_{out} - \sin\theta_{in}|}{\frac{e}{c}B_o} \qquad \text{(IV.1)}$$

where θ_{in} and θ_{out} are the entrance and exit angles, respectively, to the field region. (See Appendix B for further details.) Finally, one may define the effective edge as that point where the field falls to

half the central value. For the JANUS magnet, these three methods agree to within 1mm.

Once the effective edge has been calculated, Eqn. IV.1 may be inverted to give the momentum as a function of θ_{in} and θ_{out}. These angles, of course, are obtained from the MWPC information. Such a procedure is accurate to about 1.5%. This number is not the momentum resolution; it simply represents the intrinsic accuracy of the effective edge approximation for ideal trajectories as compared to propagation in the complete field map. In practice, the fact that MWPC2 lies within the fringing field means that the measured θ_{in} is not identical to the asymptotic value; this effect degrades the accuracy of the method to roughly 2.5%.

Once a candidate trajectory is obtained, and its momentum calculated, the motion in the vertical plane is checked for consistency with the effects of vertical focusing from the fringe field. Specifically, the hits in the first two MWPC's are used to predict the vertical location of the hits in the last two MWPC's. This is done using simple first-order ray optics; the actual calculation is found in Appendix B. A cut is then made on the difference between the actual and the calculated vertical position in MWPC3 and MWPC4.

If the number of surviving candidates is greater than or equal to the trigger requirement (i.e., at least one track for a singles run, at least two tracks for a two-pion run), the event is written to an output tape for further processing. The number of pruned events ranges from 5 to 15% of our on-line triggers, depending on MWPC

efficiency. The major sources of bad events are inadequate chamber information and single-pion events simulating two-pion event signatures in the AB array by creation of delta rays, which then fire an adjacent counter.

B. Second Pass: Chebyshev Parametrization

The output of the pruning program is a tape containing one record for each event. The event record consists of all the original event information, i.e., hit wires, and ADC's and TDC's for all the counters. Additionally, the tracking program specifies which wires are associated with each good trajectory candidate it finds. The purpose of the second stage of analysis is to calculate the momentum and initial target position of each track as accurately as possible, as well as making further cuts on the data based on initial position at the target ($\equiv \vec{x}_{TARG}$), counter pulse heights, time-of-flights, etc. The algorithm chosen to calculate the derived quantities such as momentum and target location is based on a Chebyshev parametrization of known (Monte Carlo) trajectories. Since this method is well described elsewhere,[76,77] only the rudiments of the technique will be presented here.

B.1. Discussion of the Method

Assume that a Monte Carlo describing a spectrometer has generated a set of N events labeled by β, $\beta = 1$ to N, written as $\vec{Z}_\beta = [\vec{X}_\beta, \vec{Y}_\beta]$. Here X is used to denote the independent quantities, and Y the dependent quantities. For example, for real events in our

spectrometer, the set of struck wires for a track define $\vec{X} = (X_1, X_2, \ldots, X_{12})$, and quantities such as $\vec{P}$ and $\vec{x}_{TARG}$ form $\vec{Y}$. (In the Monte Carlo, of course, this role is reversed.) What we seek is some algorithm that, given $\vec{X}$, returns $\vec{Y}$, that is, $\vec{Y} = \mathbf{F}(\vec{X})$. To do so, the dependence of $\vec{Y}$ upon $\vec{X}$ observed in the Monte Carlo events is used to parameterize this dependence for a general $\vec{X}$.

This parametrization is in terms of a set of reduced variables, obtained by the following prescription: First choose the origin for the $\vec{X}$'s at their center-of-gravity, that is, form

$$\vec{x} = \vec{X} - \langle \vec{X} \rangle \ , \tag{IV.2}$$

where the average is over the set of N Monte Carlo events. Then perform a principal component analysis on the $\vec{x}_\beta$'s to find the most significant linear combinations of x-basis components. This defines a new basis of event vectors $\vec{\xi}_\beta$ in terms of a real orthogonal matrix $\mathbf{A}$:

$$\vec{\xi}_\beta = \mathbf{A} \cdot \vec{x}_\beta \tag{IV.3}$$

A benefit of the principal component analysis is that the first component of ξ is the most significant, i.e., shows the most variation over the data set, followed by the second component, and so on. It is often the case that not all components of $\vec{x}$ are independent; then the least significant components of ξ are fixed. For example, if we take $\vec{x}$ as the set of twelve reduced wire numbers for a trajectory through our spectrometer (i.e., one hit per sense plane), then there are at most eight independent components of $\vec{\xi}$, since specifying the

wire numbers of any two sense planes in a MWPC essentially determines the wire number of the third sense plane, to within small corrections due to parallax, finite spatial resolution, etc. Thus, components $9 \rightarrow 12$ of $\vec{\xi}$ should show no variation over the data set, and Eqn. IV.2 insures that they are in fact near zero. The $\vec{\xi}$'s are then further transformed to restrict their variation to the interval $[-1,1]$, i.e., for each component i,

$$p_i = \frac{\xi_i}{\max\left[|\xi_i|\right]} \qquad \text{(IV.4)}$$

The maximum is taken over the set of Monte Carlo events.

Once the $\vec{p}$'s are found, an expansion in Chebyshev polynomials is used to parametrize the dependence of the $\vec{Y}$'s upon the $\vec{X}$'s. If the first m components of $\vec{p}$ are used in the expansion, we have

$$\vec{Y}(\vec{X}) = \sum_{i_1,i_2,\ldots,i_m} \vec{C}(i_1,i_2,\ldots,i_m) T_{i_1}(p_1) T_{i_2}(p_2) \ldots T_{i_m}(p_m) \qquad \text{(IV.5)}$$

where $T_m(t)$ is a Chebyshev polynomial of order m. Chebyshev polynomials are used for the expansion since they minimize the maximum deviation of the fit from each data point, rather than some "global" quantity such as chi-squared. This is precisely the property we desire for parametrizing tracks, i.e., we seek a good approximation to the $\vec{Y}$'s for <u>each</u> event.

B.2. Results of Chebyshev Parametrization

In practice, a guess for the various Y_β's is first made. The Chebyshev parametrization is then made for the <u>difference</u> between the

guess and actual value. For example, a first guess to the momentum is given by inverting the effective edge formula Eqn IV.1. Provided the guess introduces no pathological biases, this procedure results in a much more rapid convergence of the above series.

The coefficients of the Chebyshev series are determined by considering 500 Monte Carlo events, distributed preferentially over the boundaries of the JANUS spectrometer acceptance. Since the Chebyshev parametrization has the mini-max property only over the interval [-1,1], the physical acceptance boundaries must be slightly expanded in selecting the Monte Carlo events. This insures that the reduced variables ξ_β encountered for real events will always be within the applicable range of the fit. The fitted quantities are the spherical components of the initial momentum vector (in the laboratory system) $\vec{P}$, and the initial x and y coordinates at the target. (The orientation of the coordinate system is shown in Fig. 3) An expansion of roughly 25 terms suffices to obtain the accuracy given in Table 1 below:

Table 1		
Results from the Chebyshev Parametrization of Ideal Monte Carlo Tracks		
Quantity	$\langle$(MC-fit)$\rangle$	$\langle$(MC-fit)$^2\rangle$
$\lvert\vec{p}\rvert$ (MeV/c)	-0.01	2.46
θ (degrees)	6.43×10^{-5}	0.060
ϕ (degrees)	3.19×10^{-5}	0.040
x^{init} (cm.)	1.60×10^{-4}	0.253
y^{init} (cm.)	1.60×10^{-3}	0.077

The above results are for ideal Monte Carlo tracks, i.e., stochastic effects such as multiple scattering and energy loss have been turned off. Thus, Table 1 provides an indication of the intrinsic accuracy of the Chebyshev fit. Inclusion of multiple scattering and energy loss in the target (here assumed to be 1 gm/cm^2 KCl), S1 and S2 counters, MWPC's and the air determines the actual resolution obtained for the fitted quantities. These are shown in Table 2 below:

Table 2

Resolution for Fitted Quantities in Presence of Energy Loss and Multiple Scattering

Quantity	$\langle$(actual-fit)$\rangle$	$\langle$(actual-fit)$^2\rangle$
$\lvert\vec{p}\rvert$ (MeV/c)	3.74	3.79
θ (degrees)	0.042	1.01
ϕ (degrees)	5.63×10^{-3}	1.39
x^{init} (cm.)	-0.053	1.09
y^{init} (cm.)	0.046	0.893

Note that, due to multiple scattering and energy loss in the target and the S counters, the momentum of a typical pion is reduced by not quite 4 MeV/c. Nonetheless, the momentum resolution $\frac{\Delta\lvert\vec{p}_{LAB}\rvert}{\lvert\vec{p}_{LAB}\rvert}$ is, as a function of $p_{LAB} \equiv \lvert\vec{p}_{LAB}\rvert$, everywhere less than 4%, as shown in Fig. 9. Also shown in Fig. 9 is the absolute resolution, i.e., $\sigma_p \equiv \langle(\Delta p_{LAB})^2\rangle^{1/2}$. The behavior of σ_p as a function of p_{LAB} demonstrates the two sources of error in momentum analysis. At low values of p_{LAB}, σ_p is dominated by multiple scattering. As p_{LAB} increases, the multiple scattering becomes negligible. However, high rigidity pions are bent less by our spectrometer, so that 2mm spatial resolution of the MWPC's becomes important in determining the actual trajectory. The total contribution of these two competing effects is minimized for 250 MeV/c $\lesssim p_{LAB} \lesssim$ 450 Mev/c, which is the interval where the majority of our pions are found.

More relevant to the two-pion analysis is the resolution for relative momentum in the CM system. Various measures of this are presented in Figs. 10 and 11, as a function of the relative momentum. These results will be further discussed in the next chapter.

B.3. Final Event Selection

Several cuts are applied to each track found by the pruning program. First, the trajectory is projected to the AB-counter plane, and the expected AB-combination is predicted. The actual combination that was hit is required to agree with this prediction to within ±1 combination (to allow for finite spatial resolution, multiple scattering, measurement errors,etc.). The ADC for the A and B counters, and the TDC for the combination must be consistent with the signature of a pion in these counters. This eliminates protons (a problem only for π^+ runs) and out-of-time pions (a problem only at the highest beam intensities). For the surviving tracks, a Chebyshev fit is then made to the initial momentum $\vec{p}$ and the initial position at the target $\vec{x}_{TARG}$. Additionally, the information in the first three MWPC's is used to predict the location of the hit for this trajectory in MWPC4. Further cuts are then made as follows:

The initial production point $\vec{x}_{TARG}$ must be within the limits of the beam spot on the target. A typical x and y distribution of $\vec{x}_{TARG}$ is shown in Fig. 12. The distribution is roughly Gaussian, and consistent with the observed beam spot location and size for that run. Thus, the mean value of x_{TARG} reflects the fact that the beam was known to be approximately 2-3cm nearer JANUS than the

nominal beam-line axis. As an example, the cuts used for the distributions of Fig. 12 were $-1.2\text{cm} \leq x_{TARG} \leq 6.8\text{cm}$ and $-3.0\text{cm} \leq y_{TARG} \leq 3.0\text{cm}$. Next, based on the fit to the initial angle of the pion, a cut is made to eliminate all pions that would have passed through the lead collimator. Finally, the predicted value of the MWPC4 hit is compared to the actual value, and a cut is made on this quantity.

The above cuts are applied independently to each track in an event. In addition, two cuts are made on the relative orientation of the two-pion events. The first such cut requires that the tracks be separated by some distance R_{sep} in all four MWPC's. This cut insures that the cross-finding procedure described in Section A of this chapter has not somehow created a second track from the wires of a single particle event. Variation of R_{sep} thus provides some indication of the frequency of fake track generation. Normally, R_{sep} is set to 1.5cm. A second cut is made on the separation at the target of the two tracks, i.e., on $\vec{x}_{sep} = \vec{x}_{TARG_1} - \vec{x}_{TARG_2}$. Presumably, the distribution of $\vec{x}_{sep}$ will be narrower for two pions created in the same nuclear collision than for two pions created in separate collisions at different points in the target. We may test this hypothesis by forming the $\vec{x}_{sep}$ distribution for real two-pion events, and comparing it to the distribution generated by taking $\vec{x}_{TARG_1}$ and $\vec{x}_{TARG_2}$ from different events. The effect is particularly dramatic for the y-projection of this distribution, shown in Fig. 13. While not as striking as the y-projection, the x-projection is also narrower for

real events as compared to random events (a FWHM of 5.2cm as compared to 6.3cm).

The events that pass all cuts are written to a disk file for further processing. This forms our data base of good two-pion events from which pion source parameters are extracted through a correlation analysis.

C. Third Pass: Generation of the Correlation Function

At this stage of the analysis, we have a file of correlated, momentum-analyzed, two-pion events. In this pass, the set of two-pion events is used to construct the correlation function (defined in Chapter II). Since there is a variety of prescriptions for this construction, and since there are some subtleties involved, we begin this section with a more detailed examination of the correlation function.

In general, a normalized two-particle correlation function is defined as

$$C_2(\vec{p}_1,\vec{p}_2) = \frac{\langle n_\pi \rangle^2}{\langle n_\pi(n_\pi-1)\rangle} \cdot \frac{\dfrac{d^6n}{dp_1^3 dp_2^3}}{\dfrac{d^3n}{dp_1^3}\dfrac{d^3n}{dp_2^3}} \qquad \text{(IV.6)}$$

$$= 1 + A(\vec{p}_1,\vec{p}_2) \quad ,$$

where $\Lambda \rightarrow 0$ for large values of $|\vec{p}_1 - \vec{p}_2|$. In this expression, the number densities are defined as

$$\frac{d^3n}{dp^3} = \frac{1}{\sigma}\frac{d^3\sigma}{dp^3}$$

The presence of the factors involving the pion multiplicities insures that the numerator and denominator have the same normalization. They result from the definition of the one-particle inclusive and two-particle inclusive distribution normalizations, i.e.,

$$\int \frac{d^3n}{dp^3} d\vec{p} = \langle n_\pi \rangle$$

and

$$\int \frac{d^6n}{dp_1^3 dp_2^3} d\vec{p}_1 d\vec{p}_2 = \langle n_\pi (n_\pi - 1) \rangle$$

In principle, one could construct the correlation function by directly measuring the two-particle inclusive, one-particle inclusive, and total cross sections, then computing the ratio defined in Eqn. IV.6. In practice this is never done, for a variety of reasons. First, there is the purely practical matter of obtaining sufficient statistics in six-dimensional phase space. Second, it is known that, if the pions are well described by plane waves, then $\Lambda(\vec{p}_1, \vec{p}_2) = \Lambda(q_0, \vec{q}) = |\rho(q_0, \vec{q})|^2$, where ρ is the Fourier transform of the source density and q_0 and $\vec{q}$ are defined in Eqn. II.22. (We will use these symbols, along with $q \equiv |\vec{q}|$, for the remainder of this thesis.) Finally, there are systematic uncertainties in a simultaneous determination of three different types of cross section. In

fact, the mere requirement of one pion versus two pions leads to a substantial trigger bias. The nature of this bias is discussed in detail in Appendix D, where it is analyzed in terms of impact parameter selection. The results of that analysis indicate that a one-pion trigger for the JANUS spectrometer skews the mean impact parameter only slightly from that of an inelastic trigger, whereas the two-pion requirement (for Ar + KCl) is equivalent to the Streamer Chamber central collision trigger[78] $\sigma \simeq 180$ mb., or $b \leq 2$fm. Thus, even in the limit of an infinite amount of data, a blind application of Eqn. IV.6 would lead to an improper averaging over different event classes.

Therefore, instead of direct application of Eqn. IV.6, we seek a method for describing all features of a relative momentum spectrum for a given reaction, except the Bose-Einstein correlations. The resulting distribution $B(q_0,\vec{q})$, called the *background* distribution, would then give the correlation function when compared to the actual spectrum $A(q_0,\vec{q})$:

$$C_2(q_0,\vec{q}) = \frac{A(q_0,\vec{q})}{B(q_0,\vec{q})} \qquad \text{(IV.7)}$$

There is a variety of prescriptions for generating B, each with application in various regimes. Before describing the method we chose to use in this work, it is illustrative to examine alternative procedures.

The most direct approach to calculating B requires the presence of a complete dynamical model for the system being studied. $B(q_0,\vec{q})$ is then explicitly calculated by removing the like-particle

symmetrization from the model. Not surprisingly, the only model amenable to calculation is the statistical model (see, e.g., the results of Ref. 32). The obvious difficulty with this method is the model-dependence. The features in a $C_2(q_0,\vec{q})$ so obtained measure the deviation of $A(q_0,\vec{q})$ from the model used for the phase space population; only in the limit of a perfect model, i.e., a complete theory, does the resulting C_2 accurately reflect the Bose-Einstein enhancement.

The remaining techniques for determining B all attempt to use the data directly to obtain the expected phase space distribution for like-particle pairs in the absence of Bose-Einstein correlations. For instance, $\pi^+\pi^-$ pairs presumably reflect the same kinematic constraints as $\pi^-\pi^-$ pairs, but do not obey a symmetrization requirement. Unfortunately, the production mechanism and final state interactions of $\pi^+\pi^-$ pairs are dominated by a series of resonances (η, ρ, ω,...) not present in the like-pion channel. Nonetheless, provided the contribution from these resonances may be removed unambiguously,[45,48,47-55] this approach is often very useful (see, however, Ref. 54). Implicit in the use of this background is equal, or at least well understood, detection efficiencies for π^+'s and π^-'s. This is certainly not the case for the JANUS spectrometer, which is not capable of simultaneous measurement of opposite charged pions. Furthermore, the utility of $\pi^+\pi^-$ background generation for heavy ion physics is questionable. First, present-day energies are such that π^+-p separation is difficult over much of phase space.

Secondly, the Coulomb effects of the residual nuclear charge are opposite for π^+ and π^-, leading to observable differences in their momentum spectra.

Yet another technique for generating B from the data uses fake two pion events created by mixing individual pion tracks from different events. Since the Bose-Einstein interference does not extend from event to event, this approach should produce a background spectrum containing the actual single-particle detection efficiencies as well as the relevant phase space factors. This is the method that we chose for the analysis of our data.

While intuitively appealing, the use of pions from different events may be complicated by several possible effects. First is energy-momentum conservation, or rather, lack of it. This is indeed a valid objection for some high energy physics experiments, where the small number of produced particles, leading particle effects, jet phenomena, etc. can lead to strong kinematic constraints. In some cases, it is possible to circumvent this problem by creating a spectrum of "random" pions by the exchange of momentum components of <u>different</u> pions from the <u>same</u> event.[40,54] For heavy ion physics, this is not expected to be a serious problem, in that the energy contained by the pions is a small fraction of the total available energy. To see this, consider the collision of two nuclei of mass A in the CM system, where each nucleus has energy $\gamma_{CM} A \cdot M_N$. Assuming isospin symmetric matter, this ratio is

$$f = \frac{\langle E_\pi \rangle}{(Y_{CM}-1)M_N} \cdot \frac{3\langle n_\pi \rangle}{2A} \qquad \text{(IV.8)}$$

For central 1.8A·GeV Ar + KCl collisions, $\langle n_{\pi^-} \rangle \simeq 6$, and $\langle E_\pi \rangle \simeq 2m_\pi$, leading to f ≅ 17%. Thus, it is unlikely that any combination of two pions in a given detector will make significant inroads on this large reservoir of energy. Similar considerations apply, of course, to momentum.

The nature of the statistical errors for background events represents a second effect in different-event mixing with subtle consequences. If we begin with N pion momentum vectors, we can generate from them $\frac{1}{2}N(N-1) \cong \frac{1}{2}N^2$ pairs of background events. Say n of these pairs fall into a given bin in q_0-q space. Naively, we might assume the error on n to be given by $\sigma_n = \sqrt{n}$. However, one is always suspicious of getting something for nothing, which is just what our background mixing has done. That is, the background mixing has resulted in, for large N, a tremendous increase in the number of background pairs, while starting from what may be a quite limited statistical base. A more careful analysis shows that the actual error is given by $\sigma_n = 2n^{3/4}$. This effect has important consequences for our data analysis, which are discussed, along with a derivation of the $n^{3/4}$ rule, in Appendix E.

The third problem with different-event mixing arises when the correlation factor $\Lambda(\vec{p}_1,\vec{p}_2)$ shows little variation over the detector acceptance region. To see this, consider the extreme limit of a very narrow-band spectrometer, where all accepted pairs have small rela-

tive momentum compared to the correlation function, i.e, $|\vec{p}_1 - \vec{p}_2| \leq \frac{1}{R}$ for all accepted pairs. Then any mixed pair will inevitably be made of pions associated with another close partner in the real event. This leads to a "dilution" of the enhancement, in that the background B also contains the effects of the correlation factor Λ.

To see this mathematically, consider for convenience a discrete model for a two-pion correlation experiment. Let η_i denote the spectrometer acceptance for events with momentum $\vec{p}_i$, i.e., $\eta_i = \eta(\vec{p}_i)$. similarly, let $u_i = \frac{d^3n}{dp_i^3}$, and $C_{ij} = C_2(\vec{p}_i, \vec{p}_j)$. (This analysis assumes that C_2 is a function of the two individual momenta. This is for mathematical simplicity only. The use of q and q_0 simply introduces some additional sums and projection operators, while obscuring the physical origin of the effect.) The real one pion counting rate is then given by

$$P_1^R(i) = \eta_i u_i \tag{IV.9}$$

while, assuming $\eta_{ij} = \eta_i \eta_j$, the two-pion rate is given by

$$P_2^R(ij) = \eta_i u_i \cdot \eta_j u_j \cdot C_{ij} \tag{IV.10}$$

Clearly,

$$\frac{P_2^R(ij)}{P_1^R(i) P_1^R(j)} = C_{ij}$$

This is just the discrete form of Eqn IV.6. Now consider the results of generating a background spectrum by mixing individual pion pairs

from different two-pion events. The number of fake pions with momentum i is given by summing over all unobserved "second" pions, thus

$$P_1^F(i) = \eta_i u_i \cdot \sum_m \eta_m u_m C_{im} \qquad \text{(IV.11)}$$

The correlation function from mixing different events is then given by

$$C_{ij}^{diff} = \frac{P_2^R(ij)}{P_2^F(ij)} \qquad \text{(IV.12)}$$

where the fake two-pion distribution is given by

$$P_2^F(ij) = P_1^F(i) \cdot P_1^F(j) \qquad \text{(IV.13)}$$

$$= \left[\eta_i u_i \sum_m \eta_m u_m C_{im}\right] \cdot \left[\eta_j u_j \sum_n \eta_n u_n C_{jn}\right]$$

Writing $C_{im} = 1 + \Lambda_{im}$, we obtain

$$C_{ij}^{diff} = \frac{\sum_m \eta_m u_m \cdot \sum_n \eta_n u_n}{[1+\delta_i] \cdot [1+\delta_j]} \cdot C_{ij} \qquad \text{(IV.14)}$$

with

$$\delta_i = \frac{\sum_m \eta_m u_m \Lambda_{im}}{\sum_m \eta_m u_m} \qquad \text{(IV.15)}$$

$$= \frac{\sum_m N_m \Lambda_{im}}{\sum_m N_m}$$

Here N_m is the actual number of events measured with momentum $\vec{p}_m$. The numerator of Eqn. IV.12 is an arbitrary normalization constant whose magnitude depends on the number of pairs used to mix our background. Thus, C_{ij}^{diff} will be proportional to C_{ij} only if the

variation of δ_i and δ_j is negligible over the spectrometer acceptance. Such is not the case for the JANUS spectrometer, where the influence of the correlations on the background spectra is substantial. Monte Carlo studies for the JANUS spectrometer indicate that, assuming an initial correlation function with "typical" source parameters, the C_2^{diff} generated by different-event mixing is essentially flat. The reason for this surprising result is that the δ_i's in Eqn.and have a momentum variation similar to C_{ij}'s.

Fortunately, Eqn. IV.12 also contains the solution to these difficulties. If we had a priori knowledge of the δ_i's, then we could remove their influence by weighting each fake event by the factor

$$g_{ij} = \frac{1}{[1+\delta_i]\cdot[1+\delta_j]}$$

In practice, of course, the δ_i's are dependent on just what we're attempting to measure, i.e., the source parameters contained in Λ. Therefore, a recursive approach is required: First some initial guess for the source radius and lifetime is made. The δ_i for each event with momentum $\vec{p}_i$ is then determined by evaluating the sum given in the second line of Eqn. IV.15. The correlation function is then calculated by weighting each of the background events with the g_{ij}'s given above. A fit is then made to the correlation function to extract the new source parameters (as described in the next section), which are then used to close the loop by re-evaluating the δ_i's. Assuming a good guess is initially made, this process is rapidly convergent, requiring 2-4 iterations to obtain values of the source parameters stable with respect to further iteration. The values so

obtained are independent of the starting values, as verified by both actual data and by Monte Carlo simulation.

We close this section with a theoretical remark. The alert reader will have noted that , even in the limit of 100% detection efficiency over all 4π, the δ_i's do not vanish. This effect may be traced back to the second line of Eqn. IV.6, which is derived on the assumption of independent pion emission by the source. (Recall the passage from Eqn. II.25 to Eqn. II.26.) The validity of this assumption is measured by the size of the δ_i's. One may show, either by direct calculation using some parametrization of the C_{ij}'s and w_i's, or by the argument contained in Appendix A of Ref. 58, that these correction terms are the order of $\epsilon \simeq \frac{\langle\lambda_\pi\rangle^3}{R^3}$, where $\langle\lambda_\pi\rangle$ is the average pion wavelength, and R is the source size. (The similarity of this result to Eqn. II.4 is not coincidental.) It is further shown in Ref. 58 that $\epsilon \sim \frac{1}{A} \lesssim 5\%$ for heavy ion collisions of atomic number A.

D. Fourth Pass: Fitting the Correlation Function

The correlation functions calculated via the prescription of the previous section are fit to a function of the form

$$C_2(q_0,q) = N\left[1 + \lambda\cdot\Lambda(q_0,q)\right] , \qquad \text{(IV.16)}$$

where Λ is the squared Fourier transform of the assumed source distribution. Our canonical parametrization is a Gaussian one, viz.,

$$\Lambda(q_0,q) = e^{-q_0^2\tau^2/2 - q^2R^2/2}$$

The normalization constant N is of no physical significance, since it merely normalizes the total number of fake events over the acceptance to the total number or real events. The parameter λ is a phenomenological device introduced by Deutschmann et al.[48] to measure the "strength" of the interference effect. While for a fully chaotic source we must have $\lambda = 1$, the presence of dynamical correlations, exotic processes, final-state interactions, background contamination, etc. can all lead to deviations of λ from one. Thus, it is advantageous in the fitting procedure to leave λ as a free parameter to reflect the presence of such effects.

The method used to fit the data deserves further examination, in that there does appear to be some confusion in the literature. It is extremely dangerous to use a least-squares analysis to fit the correlation function, i.e., to minimize the quantity F, where

$$F = \sum_{q_0,q} \left[\frac{C_2(q_0,q) - K(q_0,q)}{\sigma(C_2)} \right]^2 .$$

(Here K is the assumed form for the correlation function.) The problem with this approach results from those bins where C_2 is determined by the ratio of two small numbers. In this case, the real event number $A(q_0,q)$ and the background number $B(q_0,q)$ are both Poisson-distributed variates, not Gaussian, and their ratio is certainly not a Gaussian-distributed variable.[79] This has two consequences. First, standard error-propagation formulas for $\sigma(C_2)$ no longer apply. Second, chi-squared minimization, which assumes a Gaussian distribution of errors, is no longer a valid fitting procedure.

The solution to these difficulties lies in the Principle of Maximum Likelihood (PML). In this approach, we calculate the probability that A_{ij} real events are obtained in the ij-th bin, given that the background for that bin is B_{ij} and the correlation function is C_{ij}. That is, we seek $P(A_{ij}|\bar{A}_{ij}=C_{ij}\cdot B_{ij})$. This is clearly a Poisson distribution; thus

$$P(A_{ij}|\bar{A}_{ij}) = \frac{(\bar{A}_{ij})^{A_{ij}}}{A_{ij}!} e^{-\bar{A}_{ij}} \quad . \tag{IV.17}$$

The PML formulation simultaneously solves both problems discussed in the previous paragraph: The ratio between A and B is not taken, and the Poisson statistics of A are explicitly included. Note, however, that this method assumes that B has negligible error relative to A.

A fit is obtained by maximizing the total probability $\mathcal{P}$,

$$\mathcal{P} = \prod_{ij} P(A_{ij}|\bar{A}_{ij}) \tag{IV.18}$$

In practice, one minimizes F, the negative log of $\mathcal{P}$,

$$F = -\ln(\mathcal{P}) \tag{IV.19}$$

$$= \sum_{ij} \left\{ \bar{A}_{ij} - A_{ij} \ln \bar{A}_{ij} + \ln(A_{ij}!) \right\} \quad .$$

The minimization routine used is MINUIT,[80,81] a very general and powerful program well-suited to multi-parameter minimization and error analysis.

There are two reasons for minimizing the negative log of $\mathcal{P}$, rather than $-\mathcal{P}$ itself. First, since $P(A_{ij}|\bar{A}_{ij}) < 1$ always, the pro-

duct for Φ will become very small as the number of ij-bins becomes large. Thus, to prevent machine round-off errors, and to "slow down" the variation of Φ, we perform the usual trick of dealing with the logarithm of Φ. The second reason is a more fundamental one: in the limit of large A_{ij}'s, the distribution of A_{ij} about $\bar{A}_{ij}$ becomes Gaussian, and minimization of $-\ln(\Phi)$ becomes equivalent to a conventional least-squares minimization. This is most easily seen by simply writing

$$\lim_{\bar{A}\to\infty} P(A|\bar{A}) = \frac{1}{\sqrt{2\pi\bar{A}}} e^{-(A-\bar{A})^2/2\bar{A}} ,$$

in Eqn. IV.18, then taking the logarithm as in Eqn. IV.19. In the following, we invert this procedure, i.e., the large A limit of the second line of Eqn. IV.19 is explicitly evaluated. By doing so we will derive a goodness-of-fit parameter that is the analog of chi-squared for distributions containing small numbers of events.

Using Stirling's approximation, we have for a given term of the sum for $-\ln(\Phi)$ (dropping temporarily the ij-subscripts)

$$\bar{A} - A\ln\bar{A} + \ln(A!) \cong \bar{A} - A\ln\bar{A} + \left[A\ln A - A + \tfrac{1}{2}\ln(2\pi A)\right] \qquad \text{(IV.20)}$$

$$= (A-\bar{A}) - A\ln\left[\frac{\bar{A}}{A}\right] + \tfrac{1}{2}\ln(2\pi A)$$

$$= (A-\bar{A}) - A\left[\frac{\bar{A}-A}{A} - \tfrac{1}{2}\left[\frac{\bar{A}-A}{A}\right]^2 + \ldots\right] + \tfrac{1}{2}\ln(2\pi A)$$

$$\cong \frac{(\bar{A} - A)^2}{2A} + \tfrac{1}{2}\ln(2\pi A) \quad .$$

Our sum is thus

$$F = \sum_{ij} \left\{ \frac{(\bar{A}_{ij} - A_{ij})^2}{2A_{ij}} + \tfrac{1}{2}\ln(2\pi A_{ij}) \right\} \qquad \text{(IV.21)}$$

$$\cong \tfrac{1}{2}\,(\text{chi-squared}) + (\text{constant}) \quad .$$

This leads us to suggest that the appropriate generalization of chi-squared for Poisson distributed variables is the quantity

$$(X)^2_{PML} = 2F - \sum_{ij} \ln(2\pi A_{ij}) \quad , \qquad \text{(IV.22)}$$

since in the limit of large A_{ij}'s it reduces to the conventional chi-squared. (Here F is $-\ln(P)$ as defined in Eqn. IV.19.) The (empirically observed) properties of $(X)^2_{PML}$ will be discussed in the next chapter.

CHAPTER V

RESULTS

In this chapter the methods of Chapter IV are applied to an analysis of the two-pion events. However, before doing so, we examine the single-particle spectra from both our one and two-pion triggers. By comparison to the results of other authors, we obtain information regarding the detection efficiency of our spectrometer, as well as testing our Monte Carlo calculations of the spectrometer acceptance as a function of momentum. At this point we remind the reader that all measurements reported are for a beam energy of 1.8 A·GeV. Two systems were studied: ^{40}Ar + KCl and ^{20}Ne + NaF. For the mass 40 system both $2\pi^-$ and $2\pi^+$ data were taken; for the mass 20 system only $2\pi^-$ pairs were measured.

A. Single Particle Spectra

Since the correlation function as calculated by the prescription of Eqn IV.7 is independent of the absolute normalization, measurement of the actual magnitude of various cross sections is not required to generate $C_2(q_0,q)$. This fact, combined with the restricted time available for experimental observation, argued against performing an extensive series of efficiency measurements for each component of our detection system. However, since the ion chamber output was recorded, and its calibration known, we may invert the usual procedure to obtain our overall detection efficiency. Furthermore,

since (with one important exception to be noted below) our pion detection efficiency is expected to be independent of momentum, we may extract the shapes of invariant momentum spectra as a valuable check on our understanding of the spectrometer's acceptance.

In Figures 17 through 20 the invariant cross sections for one and two pion triggers are presented. These data are presented in terms of a cross section multiplied by an unknown efficiency factor ϵ_i, where i = 1(2) for one(two)-pion trigger requirements. The two-pion results are presented in terms of the invariant momentum distribution for one of the pions, with the "second" pion anywhere in the JANUS spectrometer acceptance. The spectrum is then also incremented for the momentum corresponding to the "second" pion, thus, it is incremented twice for each two-pion event. In all cases, the spectra show the characteristic exponential decay characteristic of pion production in RHIC.[82] There are two notable deviations from this exponential behavior. The first occurs for $E_{CM} \geq 500$ MeV and is particularly prominent for the π^+ spectra. This is obviously an unremoved proton contamination. The logarithmic invariant cross section plot dramatizes the contribution of these events. To show this, in Fig. 18-20 we also present the corresponding plot of $d\sigma/dp_{LAB}$. For example, in Fig. 18, the arrow at $E_{CM} = 500$ MeV corresponds to the arrow at $p_{LAB} \cong 700$ MeV/c. The proton contamination is barely discernible in the laboratory spectrum; its contribution to the total cross section is well under 1%.

The second deviation from the exponential slope is present only in the one-pion trigger data (Fig. 17) for $E_{CM} \leq 220$ MeV. This is the momentum-dependent efficiency alluded to above. Specifically, the thresholds of the S1 and S2 trigger counters were set for the passage of two minimum-ionizing particles. Therefore, these counters became efficient for the detection of one pion only for $T_\pi^{LAB} \leq 35$ MeV, where $\frac{dE}{dx} \geq 2\left(\frac{dE}{dx}\right)_{min}$. The enhancement is observed for precisely those values of E_{CM} corresponding to the above condition in the laboratory.

To eliminate the influence of these two effects, fits were made to exponential distributions in the region 240 MeV < E_{cm} < 540 MeV. The results are presented below in Table 3.

Table 3

Results of Fits to $E\frac{d^3\sigma}{dp^3} = Ae^{-E_{CM}/E_o}$

System	Trigger	A (mb/sr-Gev^2)	E_o (MeV)	$\int d\sigma/d\Omega$ (mb/sr)
Ar+KCl	$1\pi^-$	42.5	77±1	20.9 $\times 10^3$
Ar+KCl	$1\pi^+$	24.9	80±3	10.8 $\times 10^3$
Ar+KCl	$2\pi^-$	.183	73±2	113
Ar+KCl	$2\pi^+$	.117	77±2	58.3
Ne+NaF	$1\pi^-$	7.43	79±1	3.38 $\times 10^3$
Ne+NaF	$2\pi^-$	.083	81±1	35.0

While there is some variation over the various data sets, the exponential slopes E_o are all consistent with 77 MeV, in reasonable agreement with the value of 80 MeV derived from streamer chamber measurements by the GSI group.[83] For the Ar+KCl system, E_o for π^+'s is greater than for the corresponding π^- trigger, in accord with simple models describing the effect of the Coulomb interaction between the nucleons and pions.[84] The value of E_o for the Ne+NaF system is slightly greater than that for the analogous Ar+KCl trigger condition.

Also given in Table 3 are the integrated effective cross sections, i.e.,

$$\epsilon_i \cdot \frac{d\sigma}{d\Omega} = \int_0^\infty e^{-E/E_o} \frac{p^2 dp}{E} = A \frac{K_1(z)}{z} \quad , \quad z = \frac{m^\pi}{E_o} \quad ,$$

where $K_1(z)$ is a modified Bessel function. The cross section is given in terms of an efficiency ϵ_i times $\frac{d\sigma}{d\Omega}$ for pions at $\theta_{CM} \simeq 90^o$. To determine the ϵ_i's, we use the extrapolation of Nagamiya et al.[82] of their 2.1 A·GeV Ne+NaF data to 1.8 A·GeV, thereby obtaining $\left(\frac{d\sigma}{d\Omega}\right)_{Ne} \simeq 85$ mb/sr. For the Ar+KCl data, we use the data of Ref. 78, which gives a total pion production cross section of 4.4b. Allowing for the observed angular distribution[85] of $1 + \cos^2\theta_{CM}$, this gives, for $\theta_{CM} = 90^o$, $\left(\frac{d\sigma}{d\Omega}\right)_{Ar} \simeq 263$ mb/sr. We note that the value so obtained is consistent with an $A^{5/3}$ scaling law between the Ne and Ar systems, although the overall accuracy of these arguments is probably insufficient to exclude an A^2 behavior. The ratio of π^+ to π^- yield for the AR+KCl system is taken as 1.46, the value obtained in Ref. 82

for this system at a beam energy of 800 A·MeV. While use of this ratio at 1.8 A·GeV has no strong theoretical basis, in light of the approximate equality of the corresponding slope parameters (66 MeV vs. 77 MeV) and the very rough nature of our efficiency calculations, we feel that the assumption is adequate.

To model the detection efficiencies, we assume that there are three types: ϵ_S, which accounts for the threshold bias in the S counters for singles runs; ϵ_D, which is the efficiency for obtaining a pion after S has fired, thus it reflects the performance of the MWPC's, the probability of track recognition, and the likelihood of passing the various cuts applied to a trajectory; and finally ϵ_p, which accounts for any additional inefficiencies for finding a pair of pions in a two pion event. Writing for convenience $\frac{d\sigma}{d\Omega} \rightarrow \sigma$, we can express our measured cross sections σ_i in terms of the actual cross sections $\bar{\sigma}_i$ as

$$\sigma_{1\pi} = \epsilon_S \cdot \epsilon_D \cdot \bar{\sigma}_{1\pi}$$

and

$$\sigma_{2\pi} = \epsilon_p \cdot \epsilon_D \cdot \epsilon_D \cdot \bar{\sigma}_{2\pi} .$$

We assume that the true two pion cross section $\bar{\sigma}_{2\pi}$ can be described in terms of the mean number of pion pairs $\frac{1}{2}\langle n_\pi(n_\pi-1)\rangle$, the JANUS acceptance A_{JAN}, and the mean value of the correlation function in JANUS $\langle C_2 \rangle$, as

$$\bar{\sigma}_{2\pi} = \langle n_\pi(n_\pi-1)\rangle \cdot \langle C_2 \rangle \cdot A_{JAN} \cdot \frac{\bar{\sigma}_{1\pi}}{\langle n_\pi \rangle} .$$

The last term in the above product merely represents the geometric probability of a pion-producing reaction. There is no factor of one-half on the RHS of this equation due to the definition of the two-pion cross sections given above.

For any given system, there are three unknown ϵ's and only two known quantities, $\sigma_{1\pi}$ and $\sigma_{2\pi}$. However, we may estimate ϵ_S from the low E_{CM} behavior of the invariant cross section, where the S counters become efficient for single particles. Thus, for the Ar runs, we obtain $\epsilon_S \simeq 70\%$, and for the Ne runs $\epsilon_S \simeq 40\%$. (These runs were separated in time by 7 months, and the operating voltages and thresholds for the counters were not necessarily the same.) For all data sets we then obtain $\epsilon_D \simeq 20\%$. This value, while low, is attributed to the large number of elements in our detection system, along with unfavorable operating conditions for the small MWPC's. A perfect one-pion trajectory in our spectrometer must fire three counters and 12 planes of MWPC read-out. While the cross-finding ability of the tracking program reduces the requirement on MWPC performance, it is clear that any major inefficiencies in more than one read-out plane quickly becomes a major problem. The high intensities required for sufficient event rate (10^8-10^9 incident ions/second) produce a high background of heavily ionizing particles in the small MWPC's, a condition known to lead to substantial impairments in detection efficiency for minimum ionizing tracks.

Finally, the values of ϵ_P obtained are best left expressed in terms of the pion multiplicity. This is done to make explicit the

statistical assumptions of this model for the detection process. For the Ar π^- and π^+ two-pion runs we obtain

$$\epsilon_p(2\pi^-) \simeq \frac{7\langle n_\pi \rangle}{\langle n_\pi(n_\pi-1)\rangle} \quad \text{and} \quad \epsilon_p(2\pi^+) \simeq \frac{8.5\langle n_\pi \rangle}{\langle n_\pi(n_\pi-1)\rangle} \ .$$

With $\langle n_\pi \rangle \simeq 4$, and $\langle n_\pi(n_\pi-1)\rangle \simeq 6^2$, quite reasonable numbers are obtained for the pair detection efficiencies. (Here we have used the known multiplicity biases for the one and two-pion trigger requirements obtained in Appendix D.) Such is not the case for the Ne data, where we obtain

$$\epsilon_p(2\pi^-) \simeq \frac{10\langle n_\pi \rangle}{\langle n_\pi(n_\pi-1)\rangle} \ .$$

Thus, for any reasonable values for the pion multiplicities involved, a detection efficiency of greater than 100% is obtained. This could indicate some change in detector performance between the one and two-pion data taking (the one-pion data are the results of only one run), or could indicate a breakdown of this model for efficiencies in the presence of large trigger-dependent multiplicity biases (see Appendix D).

B. Two Pion Data

B.1. Orientation

At this point we remind the reader of the variables used in our correlation analysis. The relevant quantities are the magnitude of relative momentum $q = |\vec{p}_1 - \vec{p}_2|$, and relative energy $q_o = |E_2 - E_1|$. The correlation function is fit assuming

$$C_2(q_o,q) = 1 + \lambda e^{-q^2R^2/2 - q_o^2\tau^2/2} \qquad (V.1)$$

which corresponds to a source density of the form

$$p(r,t) \sim e^{-r^2/R^2 - t^2/\tau^2} . \qquad (V.2)$$

We defer until later the interpretation of R, τ, and λ.

In Fig. 21 profiles of an ideal correlation function are shown, taking account of the JANUS spectrometer acceptance. The contours are separated by 10 MeV, and R and τ are given typical nuclear dimensions. It is apparent that only a narrow slice of the total (relative) phase space is measured. However, Fig. 21 is somewhat misleading in that only half of the q_o-q plane is kinematically accessible. To see this, consider the relative four-momentum $t = (p_2 - p_1)^2 = q_o^2 - q^2$. This quantity is of course invariant, so we may evaluate it in any frame. Calculating it in the two-pion center-of-mass frame, where $p_{1(2)} = \left(\sqrt{Q^2+m_\pi^2}, \pm\vec{Q} \right)$, we find $t = -4Q^2$. Thus, $q^2 = q_o^2 + 4Q^2 > q_o^2$ for all non-zero Q. This implies that only the region to the right of the line $q = q_o$ in Fig. 21 is allowed.

Nonetheless, the fact remains that $q \geq q_o$ for most of our two pion events. This presents a problem regarding visual presentation of the correlation function. Clearly, it makes no sense to define a slice of constant q or q_o, then present (say) $C_2(q, q_o = \text{constant})$. For our acceptance, this produces only a few points, as is readily seen from Fig. 21. Instead, we define the spectrometer-dependent

projections

$$\langle C_2(q) \rangle = \frac{\sum_{q_o} A(q_o,q)}{\sum_{q_o} B(q_o,q)} \qquad (V.3)$$

and

$$\langle C_2(q_o) \rangle = \frac{\sum_{q} A(q_o,q)}{\sum_{q} B(q_o,q)} \quad . \qquad (V.4)$$

Here $A(q_o,q)$ is the actual number of events with q and q_o, and $B(q_o,q)$ is the corresponding background. We emphasize that these are not true correlation functions; it is only a curious fact of the *JANUS* acceptance that the resemblance is a close one. For instance, if the kinematically allowed region in the q_o-q plane were completely occupied out to some large value of q and q_o, $\langle C_2(q) \rangle$ would appear much more sharply peaked than the actual correlation function, while $\langle C_2(q_o) \rangle$ would be flat. On the other hand, for our spectrometer, these projected C_2's provide some notion of the actual variation of the data, along with an indication of the accuracy of the resulting fits.

B.2. Results of The Fitting Procedure The data of momentum-analyzed two-pion events that have passed all cuts consists of approximately 6700 $2\pi^-$ pairs and 5500 $2\pi^+$ pairs from the Ar+KCl system, along with a subset from our Ne+NaF data-base consisting of ~10,000 $2\pi^-$ pairs. In each case, the background spectrum was calculated using every possible combination of pions from different events, in accord with the requirements discussed in Appendix E. The

results of fits to Eqn. V.1 are presented on the next page in Table 4.

TABLE 4

System	Fit conditions	λ	R (fm)	$c\tau$ (fm)	(χ^2)/NDF	chi-squared / NDF
Ar+KCl $2\pi^-$	No Gamow	0.40±0.05	$0.0^{+1.1}_{-0.0}$	$4.58^{+0.4}_{-1.0}$	101.4/105	57.2/80
	Gamow corrected	0.63±.04	$2.88^{+0.5}_{-0.9}$	$3.29^{+1.4}_{-1.5}$	176.7/147	98.2/89
	Gamow corrected, R fixed	0.64±.04	= 2.70	$3.54^{+0.6}_{-0.4}$	176.8/148	98.2/90
	Gamow corrected, T fixed	0.64±.04	$3.53^{+.37}_{-.35}$	= 1.91	178.0/149	98.6/90
	Gamow and Coulomb corrected	0.63±.04	$2.77^{+.6}_{-.9}$	$3.44^{+1.1}_{-1.5}$	211.2/158	80.3/96
Ar+KCl $2\pi^+$	No Gamow	0.48±.07	2.26±1.4	$4.12^{+1.2}_{-2.0}$	98.7/105	52.4/81
	Gamow corrected	0.73±.07	$4.20^{+.4}_{-.6}$	$1.54^{+2.4}_{-1.54}$	160.6/147	67.1/88
	Gamow corrected, R fixed	0.69±.09	= 2.70	$4.10^{+0.9}_{-1.8}$	161.7/148	67.1/88
	Gamow corrected, T fixed	0.72±.06	4.10±.54	= 1.91	160.4/148	67.2/89
	Gamow and Coulomb corrected	0.73±.07	4.10±0.4	$1.76^{+2.10}_{-1.76}$	180.5/145	78.5/83
Ne+NaF $2\pi^-$	No Gamow	0.46±.09	$0.0^{+3.1}_{-0.0}$	2.98±1.0	122.6/105	76.5/82
	Gamow corrected	0.59±.08	$1.83^{+.8}_{-1.6}$	$2.96^{+.90}_{-1.0}$	219.3/148	125.7/91
	Gamow corrected, R fixed	0.59±.06	= 2.14	$2.72^{+.25}_{-.31}$	219.5/149	126.1/92
	Gamow corrected, T fixed	0.60±.06	2.80±.30	= 1.52	220.9/149	126.6/92

We begin our discussion of the data in Table 4 by directing the reader's attention to the first entry for each system, labeled "No Gamow". These are the results from fits to correlation functions with no additional assumptions regarding the final-state interactions of the pions (to be clarified below). The corresponding projected C_2's are shown in Figures 22-24. For all three systems, the values of λ are significantly less than one, on the order of 0.4-0.5. Even more striking are the values of the radius R. In two cases (the two $2\pi^-$ data sets) the fitted values for R are zero, perhaps leading one to question the validity of our entire model for the two-pion correlation function.

Before taking such a drastic measure, we note that one known interaction between two like pions has been neglected to this point. That is the relative Coulomb repulsion between the two pions, which leads to a suppression of events with small relative momentum. In conventional quantum mechanics (see also Appendix F), this effect is well understood in terms of the Gamow factor,

$$G(\eta) = \frac{2\pi\eta}{e^{2\pi\eta} - 1} \quad , \quad \eta = \frac{me^2}{\hbar q} \quad , \tag{V.5}$$

which gives the ratio of the probability density at the origin to the asymptotic value for two-like charged particles of relative momentum q and mass m. Weighting the background events to account for this suppression (note that $G(\eta)$ must also be included in the δ_1 background correction factors described in Section C of Chapter IV), we obtain the results labeled "Gamow corrected" in Table 4. These data

are also presented in Figures 25-27. At this point we simply note that the parameters obtained from these fits are more in accord with our intuitive expectations based on known nuclear dimensions. However, before further discussion of these results, we pause to deal with potential objections to the use of the Gamow correction.

First there is the question of resolution. The characteristic range of the Gamow suppression is for those relative velocities $\beta_{rel} \simeq \frac{1}{137}$. To see structure on this scale requires very good relative momentum resolution. However, there is a subtlety to this requirement, in that β_{rel} is the relative velocity in the center-of-mass frame of the two pions, not the nucleon-nucleon center-of-mass. An extension of the arguments presented in Section B.1 of this chapter shows that the invariant form for β_{rel} is

$$\beta_{rel} = \frac{\sqrt{4m_\pi^2 - t}}{-t}, \qquad (V.6)$$

where $t \equiv q_o^2 - q^2$. Thus, the large Gamow correction extends along the diagonal of the $(q_o\text{-}q)$ plane, not just for those events satisfying $q \simeq \frac{m_\pi}{137}$. At any rate, we have made Monte Carlo studies which show that our resolution is indeed capable of observing the Gamow suppression, and that no systematic biases are introduced by correcting for the same.

A second objection lies in the precise space-time picture used to describe the pion source. If the pions are emitted by an extended source in space and time, the Gamow suppression must be reduced, in that the pion wave-packets never fully overlap. In Appendix F it is

shown that this is a small effect for RHIC, on the order of a 2-3% correction to G(q) as calculated via Eqn. V.5.

The final source of error in performing the Gamow correction arises not from the correction itself, but from its interaction with a known two-particle track-finding bias in our analysis programs. Since the tracking program considers two-wire crosses as well as three-wire triangles as valid wire chamber hits, it is possible that it will accept a cross formed from the vertical wire of the second hit and the horizontal wire (recall that this plane of wires extends completely across the face of the small MWPC's) from the first hit. This of course always acts to reduce the relative momentum between the two pions, by eliminating the vertical component of $\vec{q}$. Fortunately, the JANUS acceptance in the vertical direction is quite limited, so that this is a small effect relative to our resolution except for those pairs with $q_o \approx 0$. Resolving the relative momentum into components transverse and parallel to the average momentum of the two pions, we have for this change

$$\frac{\delta q}{q} = \frac{q_t \delta q_t}{q^2} < \frac{q_t^2}{q_t^2 + q_o^2} \cdot \frac{\delta q_t}{q_t} .$$

Even in the worse case, where all of q_t is in the vertical direction, the change in q is small for all except the first two bins of q_o, since $\langle q_t \rangle$ is small for our acceptance. In reality, those events with large $\frac{\delta q_t}{q_t}$ are rare, so that average error in δq is negligible for all but the first q_o bin.

Nonetheless, this poses a problem for the Gamow correction on the lowest bin in q_o, in that the the value of q used in the G(q) is underestimated, precisely where the Gamow function is most rapidly varying. This leads to a dramatic over-correction on the first bin of $\langle C_2(q) \rangle$ for the Ar+KCl data, e.g., $\langle C_2(q=5\ \mathrm{MeV/c}) \rangle = 3.3$ for the $2\pi^-$ data. The effect is smaller but still present for the $2\pi^+$ events. It is instructive to note that corresponding $\langle C_2(q_o) \rangle$'s are quite well behaved, in that the first few bins in q have been included by this projection. Further note that the over-correction is missing from the Ne+NaF data, due to improved wire chamber efficiency, and thus improved track identification, for that running period.

To eliminate the bias due to this effect, the first bin has been excluded from all fits reported here. Exclusion of additional low q_o bins does not substantially affect the extracted fit parameters, in accord with our understanding of the origin of this tracking bias.

B.3. Discussion of Source Sizes

At this point the reader is referred to Appendix G, where the basic tools necessary for Gaussian parametrization of sources are presented. In particular, it is shown that 1.) A radius R defined for a Gaussian source as in Eqn. V.2 is equivalent to a source with uniform density of radius $R_u = 1.52R$, 2.) A schematic model for pion production predicts $\tau \geq \frac{R}{\sqrt{2}\beta_{cm}\gamma_{cm}}$, where β_{cm} and γ_{cm} are the velocity and Lorentz gamma factor for the incident ions in the nucleon-nucleon

center-of-mass, and 3.) More realistic Monte Carlo cascade calculations give values of τ 2-3 times larger than the above prediction. Assuming $R_u = 1.2A^{1/3}$fm, and using the value of τ calculated from the model mentioned in Point 2 above, we would have

$$R \simeq 2.70\text{fm}, \qquad \tau \geq 1.91\text{fm/c} \quad \text{for Ar}; \tag{V.7}$$

$$\simeq 2.14\text{fm}, \qquad \geq 1.52\text{fm/c} \quad \text{for Ne}.$$

Examining the entries in Table 4 labeled "Gamow corrected", we find values of R and τ more or less consistent with the above geometric results. (The least consistent value is the R value for the Ar+KCl, which is $4.20^{+.4}_{-.6}$fm.) However, in some cases, particularly the lifetimes, this consistency is obtained at least as much through the large errors as through the fitted values. The nature of these errors is shown graphically in Figures 29-31, which give the 68% and 95% confidence levels for the determination of R vs. τ. It is apparent that our maximum sensitivity is to some combination such as $R^2 + \tau^2$; the orthogonal combination (the variable $\phi = \tan^{-1}(\frac{\tau}{R})$) is only weakly determined. This is a direct result of our narrow acceptance in q_o versus q illustrated in Figure 21.

By fixing either R or τ to some assumed value the errors in the extraction of the conjugate parameter are significantly reduced. For instance, the entries in Table 4 labeled "R fixed" have the radius fixed to the geometric values given above. We note that both the PML quality of fit indicator $(X^2)_{PML}$, defined in the last section of Chapter IV, and the traditional chi-squared show no significant vari-

ation when R or τ are so restricted, verifying the qualitative information provided by the likelihood contours. (The chi-squared entries of Table 4 are calculated by a restricted sum over only those bins with at least 5 real events, in accord with the usual prescription[86] for the validity of this statistic.)

In general, the Ne+NaF size parameters are smaller than the corresponding ones for the Ar+KCl system. The ratio of sizes is roughly consistent with the expected $A^{1/3}$ scaling. A good estimate of the magnitude and significance of this effect may be obtained by comparing Fig. 31 to Fig. 29. The lifetimes for the $2\pi^-$ data are intermediate between the minimum value of $\frac{R}{\sqrt{2}\beta_{cm}\gamma_{cm}}$. and the Monte Carlo prediction of 5.55 fm/c (for Ar+KCl). The value of τ for the $2\pi^+$ data is smaller than one would expect from geometric considerations, although the errors on this quantity are large: $\tau = 1.54^{+2.4}_{-1.54}$ fm/c.

Finally, we briefly discuss the external Coulomb corrections. Until now we have neglected the interaction of the pions with the nuclear charge of the pion source. This is clearly an approximation, albeit a good one for relative momentum. While the existence of strong Coulomb effects in single-particle momentum spectra may be quite striking,[2] to first order both pions receive the same momentum impulse from the Coulomb interaction with the nuclear charge (particularly for $q \simeq 0$). Thus, the change in relative momentum should be quite small. Nonetheless, in an attempt to increase the consistency between our $2\pi^-$ and $2\pi^+$ results, we have corrected each individual

pion momentum vector for the momentum shift produced by the residual nuclear charge. We do this using the formalism of Ref. 84 to calculate the change in the μ-th component of four-momentum δp_μ as a function of the final momentum p_f:

$$\delta p_\mu(p_f) = \frac{Z_i}{137}\left[p^f_\mu - (p^f u_i)u_{i\mu} \right] \cdot \frac{(p^f u_i)R_{eff}}{1 + \left[(p^f u_i)^2 - m_\eta^2\right]R_{eff}^2} \qquad (V.8)$$

In this expression Z_i is the charge of the i-th nuclear fragment, which is assumed to be moving with four-velocity u_i in the frame in which we are calculating δp_μ. The notation $(p^f u_i)$ denotes the four-product between p_f and u_i. The effective radius R_{eff} is the reciprocal of the mean inverse radius of the source, i.e.,

$$R_{eff} = \left\langle \frac{1}{r} \right\rangle^{-1} .$$

This may be evaluated for our Gaussian source density to obtain

$$R_{eff} = \frac{\sqrt{\pi}}{2} R.$$

We assume the nuclear charges consists of three fragments, a fraction f of the initial charge 2Z at rest in the center-of-mass, and two fragments $\frac{1}{2}(1-f)Z$ moving with the target and projectile velocities. Guided by the considerations of Appendix D, we choose $f = 0.80$. Calculating the correlation function with momenta corrected according to this prescription produces the results in Table 4 labeled "Gamow and Coulomb corrected". The changes in the radii and lifetimes are small, ($\lesssim 0.2$fm), especially with respect to the statistical errors on these quantities. This confirms our intuitive arguments that the so-called external Coulomb correction

has a small effect on relative momentum determinations. In the interest of completeness, we note that this is at best a crude method for handling the very complicated three-body final state interaction problem between the two pions and the nuclear charges. The reader is referred to Ref. 84 for further details.

We close this section by examining the data of other authors for this energy. No direct comparison is available, in that the results reported elsewhere in the literature are streamer chamber measurements for the reactions $Ar+BaI_2 \rightarrow 2\pi^- + X$ and $Ar+Pb_3O_4 \rightarrow 2\pi^- + X$. The authors of Ref.59 find $R = 3.05 \pm 1.1$fm for the BaI_2 target, and $R = 3.3 \pm .9$fm for the Pb_3O_4 target, both fits being performed with $c\tau = 1.5$fm. Allowing τ to vary for the Pb target, they find $R = 3.98 \pm .78$fm and $c\tau = 0.6^{+1.2}_{-0.5}$fm. In Ref.61 , the multiplicity dependence of R for the $Ar+Pb_3O_4 \rightarrow 2\pi^- + X$ system is studied, again with $c\tau = 1.5$fm. For $N_\pi = 2$-4 they obtain $R = 3.12 \pm 1.1$fm, while for $N_\pi = 5$-8 $R = 4.00 \pm .72$fm. These numbers are quite compatible with ours for the Ar+KCl system, especially when it is recalled that $\langle n_\pi \rangle \simeq 6$ for the JANUS two-pion trigger. This reinforces our view, as expressed in Appendix D, that the mean pion multiplicity is proportional to the number of participants in a reaction.

B.4. Implications for Coherence

A number of authors have suggested that value of λ may be related to the degree of coherence of the pion source.[58,67] For example, in both of the references cited, the result

$$\lambda = 1 - \left[\frac{n_{coh}}{n_{coh} + n_{ch}}\right]^2 \qquad (V.9)$$

is derived, which expresses λ in terms of the number of coherent and chaotic pion emitters n_{coh} and n_{ch}, respectively. Taking $\lambda \approx 0.64$, we obtain $\frac{n_{coh}}{n_{ch}} = \frac{3}{2}$. This is a surprisingly large result but not inconsistent with some λ values as measured in hadron-hadron reactions.

The determination of the coherent component is complicated by several systematic effects. First, and perhaps most obvious, is the interaction between λ and the Gamow correction. These are clearly closely coupled, so that any small error in performing the Gamow correction may lead to a large change in the value obtained for $\frac{n_{coh}}{n_{ch}}$. A second, more devious effect, results from the role played by λ in the background correction sums given in Eqn. IV.15. The errors in λ feed back into the process, which tends to increase the error on λ to roughly twice the statistical values given in Table 4. Finally, we should mention that recent work by Gyulassy[71] shows that averaging over unobserved dynamical variables can lead to large deviations of λ from 1, even in the absence of a coherent component to the pion source. Therefore, we feel that any strong statement concerning the significance of our value for λ would be unwarranted.

CHAPTER VI

CONCLUSIONS AND FUTURE RESEARCH

In this chapter we briefly summarize the important points of this thesis, then discuss future directions for the use of intensity interferometry in RHIC.

We have demonstrated in this work that the Bose-Einstein correlation between identical pions leads to an an enhancement for such pairs at low relative momentum. A simple model for the production process, i.e., independent particle emission over some region distributed in space and time, allows us to interpret this enhancement in terms of the source size. The sizes so obtained are consistent with normal nuclear dimensions. This is already an interesting result, in that it indicates that the pions we see are created more or less at normal nuclear density, not some very compressed phase. The measured lifetimes are intermediate between the minimum values allowed (in a geometric model consistent with the extracted sizes) and the predictions of a Monte Carlo cascade code.

These results are complicated by the existence of several effects. First, the influence of the correlation on the background spectrum is large, and must be included. Second, there are subtle aspects to the fluctuations in the background spectrum, with important consequences for data analysis. Thirdly, the two-pion mutual Coulomb interaction requires that a Gamow correction must be made to

the low relative momentum events. Finally, the data may indicate the presence of a substantial degree of coherence for the pion source, thereby obscuring direct geometric interpretation of the source size.

Nonetheless, we feel that there is reason for cautious optimism regarding future experiments. A spectrometer configuration with greatly increased acceptance is currently being planned. This will open a much larger region of relative momentum phase space, with two important consequences. First, as the phase space increases, the correction to the background spectrum due to the correlation function decreases. This fact means that analysis will be more straightforward, leading to greater reliability for our estimates of the source paremeters, and in particular, the degree of coherence. Secondly, an increase in the relative momentum phase space decouples q from q_o. In addition to decoupling the radius from the lifetime in the fitting procedure, this may allow separate extraction of transverse and longitudinal dimensions of the source, thereby providing further tests of the geometric picture of the collision process as determined by Monte Carlo calculations. Such comparisons can only increase our understanding of this developing field.

This work was supported by the Director, Office of Energy Research, Division of Nuclear Physics of the Office of High Energy and Nuclear Physics of the U.S. Department of Energy under Contract DE-AC03-76SF00098.

APPENDIX A

IONIZATION CHAMBER CALIBRATION

The ionization chamber mentioned in Chapter III has been used by our group and others for several years. In that time, the calibration constants for a wide variety of incident beams and energies have been obtained. (See the labeled points on Fig. 5.) The usual procedure for calibrating the ion chamber consists of comparing the current measured at low beam intensities to the number of counts registered by scintillators counting the beam-particles pasaing through the chamber. Dark current corrections were sometimes made, although they were found to have virtually no effect on the calibration obtained. The end result of such a procedure is a number giving the charge collected per incident ion. Fig. 5 shows that the ion chamber response is well described by

$$R_{fit} = \frac{(dE/dx)_{ion}}{3 \times 10^{16} \text{ions/coul}}$$

where $(dE/dx)_{ion}$ is the dE/dx of the beam particle (in Mev/gm cm^{-2}) in Argon.

One may also calculate the theoretical ion chamber response, knowing that the chamber uses a 80% Ar - 20% CO_2 gas mixture at 800mm Hg, with an active area between the collection plates L_{IC} = 3.18cm. To an excellent degree of approximation, one may consider the chamber to contain pure Ar. Using the ionization constant of 26 eV/ion pair for Ar,[87] and writing ρ_{Ar} for the density of the Ar gas, we obtain

$$R = \frac{26\text{eV/ion pair}}{\rho_{Ar} \cdot L_{IC} \cdot 1.6 \times 10^{-19}\ \text{coul/ion pair}}$$

$$= 1.01 \cdot R_{fit},$$

in complete agreement with the experimentally derived value.

APPENDIX B

TRACKING METHODS

1. Track Recognition

Track recognition is performed using a simple geometric model for orbits in the magnetic field. The relevant geometry is given in in Fig. 6, which is a schematic illustration of the JANUS spectrometer configuration. An incoming ray, defined by $\overline{AB}$, intersects the beginning of the effective field region at the point X_{IN}. Similarly, the outgoing ray $\overline{CD}$ intersects the end of the effective field at the point X_{OUT}. Since the effective field is constant by definition, the trajectory in the field region is a segment of a circle. Therefore, the perpendiculars to $\overline{AB}$ at X_{IN} and to $\overline{CD}$ at X_{OUT} both lie along radii of this circle, and their intersection point O is the center of the circle. This of course means that $R_{IN} = |\vec{X}_{IN} - \vec{O}|$ and $R_{OUT} = |\vec{X}_{OUT} - \vec{O}|$ are the same length.

The tracking program calculates R_{IN} and R_{OUT} for each pair of ingoing rays, then examines the ratio

$$\delta r = \frac{R_{OUT} - R_{IN}}{\frac{1}{2}(R_{OUT} + R_{IN})}$$

Monte Carlo results indicate that δr is a sharply peaked quantity for real tracks, with an rms width of 3%. The tracking program makes the loose requirement that $|\delta r| \leq 10\%$, which selects real tracks from the uniform distribution in δr created by random association of unrelated

incoming and outgoing rays.

2. Momentum Determination for Planar Orbits

Consider a particle of momentum p and charge e traversing a magnetic field. Assume the motion is confined to the x-y plane, i.e., $\vec{B} = (0,0,B_z(x,y))$ and $\dot{z} = 0$. The trajectory in space is then described by some function $y = y(x)$, as shown in Fig. 7. The Lorentz force law tells us that the inverse local curvature is proportional to the value of B_z at that point, i.e,

$$\frac{1}{R(x,y)} = \frac{eB_z(x,y)}{cp} .$$

Using the standard result for geometric curvature, we have

$$\frac{eB_z(x,y)}{cp} = \frac{|y''|}{\left[1 + y'^2\right]^{3/2}} ,$$

where $y' = dy/dx$, etc. If $y'' > 0$ everywhere, we may integrate this expression immediately, thus

$$\frac{e}{pc}\int_{x_1}^{x_2} B_z(x,y)dx = \int_{x_1}^{x_2} \frac{y''dx}{\left[1 + y'^2\right]^{3/2}}$$

$$= -\frac{y'(x_1)}{\sqrt{1 + y'(x_1)^2}} - \frac{y'(x_2)}{\sqrt{1 + y'(x_2)^2}}$$

$$= \sin\theta_{IN} - \sin\theta_{OUT} .$$

Taking account of the signed quantities, this may be written as

$$p = \frac{e}{c} \cdot \frac{\int_{x_1}^{x_2} B_z(x,y)\,dx}{|\sin\theta_{IN} - \sin\theta_{OUT}|} .$$

This is a general expression for any planar orbit. If the field region is essentially contained between x_1 and x_2, and if the effective edge approximation is valid, we may write for the integral

$$\int_{x_1}^{x_2} B_z(x,y)\,dx = B_o \cdot X_{eff} ,$$

where B_o is the central value of the field. Alternatively, we may use this expression to define the effective edge for a set of trajectories, thereby obtaining Eqn. 1 of Chapter IV, with $X_{eff} = 2(L + L_{eff})$.

3. Vertical Focusing

The motion in the vertical plane of the spectrometer (i.e., perpendicular to the pole tips) is well described by first-order geometrical optics. In this approximation, the effect of non-normal entry to a magnetic field on the vertical motion is equivalent to that of a thin lens of focal length $f = \frac{R}{\tan\theta}$, where R is the radius of curvature in the bend plane, and θ is defined as in Fig. 7.

To describe the focusing forces quantitatively, consider the schematic cross-section of the JANUS spectrometer system shown in Fig. 8. Defining the usual vertical motion vector

$$\vec{Z} = \begin{bmatrix} z \\ z' \end{bmatrix},$$

where $z' = dz/dx$, the effect of a thin lens of focal length f is given by the transfer matrix

$$F = \begin{bmatrix} 1 & 0 \\ \frac{-1}{f} & 1 \end{bmatrix}$$

Similarly, the matrix for a drift-space of length L is given by

$$D = \begin{bmatrix} 1 & L \\ 0 & 1 \end{bmatrix}$$

Thus, given the vector $\vec{Z}_2$ at MWPC2, the vector at MWPC4 is given by

$$\vec{Z}_4 = D_4 \cdot F_{out} \cdot D_B \cdot F_{in} \cdot D_2 \cdot \vec{Z}_2$$

Written out explicitly,

$$\begin{bmatrix} z_4 \\ z_4' \end{bmatrix} = \begin{bmatrix} 1 & l_4 \\ 0 & 1 \end{bmatrix} \begin{bmatrix} 1 & 0 \\ -1/f_{out} & 1 \end{bmatrix} \begin{bmatrix} 1 & 2L \\ 0 & 1 \end{bmatrix} \begin{bmatrix} 1 & 0 \\ -1/f_{in} & 1 \end{bmatrix} \begin{bmatrix} 1 & l_2 \\ 0 & 1 \end{bmatrix} \begin{bmatrix} z_2 \\ z_2' \end{bmatrix}$$

Monte Carlo studies indicate that the value of z_4 predicted by this algorithm has an rms distribution of approximately 2cm about the actual z_4 value. Roughly 75% of this deviation comes from multiple-scattering in the target, counters, chambers and air; the remainder is attributable to the intrinsic accuracy of this approach.

APPENDIX C

Monte Carlo Methods

This appendix describes some of the assumptions and features of a Monte Carlo program written to simulate the performance of the JANUS spectrometer system. This program was used to study the momentum acceptance and resolution of the system, as well as to provide ideal trajectories used in the Chebyshev parametrization.

1. The Field Map

The magnetic field of the JANUS spectrometer was measured using a conventional apparatus provided by the LBL Magnetic Measurements Group. This device measures the field components by digitizing the voltage induced on three orthogonal search coils as they are moved through the field region. The measurements were made on a grid of 1.0032in, 1.00in, and 1.00in in the x,y, and z directions, respectively. (The coordinate system is that of Fig. 3) Because the physical travel of the mapper was limited to 30 inches in the z-direction, it was necessary to map the JANUS volume in three separate passes, requiring a mechanical realignment and magnetic recalibration of the apparatus. The digitized voltages are written to magnetic tape by a PDP-8 computer.

These tapes are analyzed off-line to provide files of magnetic field data. Before using this data as a field map in a Monte Carlo, every effort must be made to remove systematic errors from the

measurement process. For instance, we know that (to within the alignment errors of the coils and pole tips) the B_z component must be anti-symmetric about the midplane of JANUS. In particular, we must have $B_z(x,y=0,z) = 0$. If, due to some normalization error, this is not the case for the field map data, net drifts in the y-direction will be produced by the Monte Carlo program in tracking particles through the field, even if the initial conditions are $\dot{y} = y = 0$. An artificial motion such as this can produce pathological problems in performing the Chebyshev parametrizations. Additional sources of systematic error result from the relative normalization of the three separate map regions, the precise alignment of the search coils, etc.

To circumvent these problems, each component was processed as follows: Obviously bad points and normalization errors were removed, so that the field profiles were continuous across the three map regions. Next, the field was explicitly symmetrized across the three orthogonal planes passing through the center of the JANUS magnet. For example, B_x is required to be symmetric in x and z, and anti-symmetric in y. Since it each component of the field satisfies $\nabla^2 B_i = 0$, a iterative Laplacian smoothing algorithm was used to calculate the interior regions of the field.[89] This algorithm is based on the observation that the discrete version of Laplace's equation gives the value of the field at any point according to the weighted average of the neighboring points, thus

$$B(i,j,k) = \frac{1}{\frac{2}{a^2}+\frac{2}{b^2}+\frac{2}{c^2}}\left\{ \frac{1}{a^2}\Big[B(i+1,j,k) + B(i-1,j,k)\Big] + \frac{1}{b^2}\Big[B(i,j+1,k) + B(i,j-1,k)\Big] + \frac{1}{c^2}\Big[B(i,j,k+1) + B(i,j,k-1)\Big] \right\}$$

Here a,b, and c are the lattice spacings in the x,y, and z directions, and B is any (rectangular) component of the field. The appropriate boundary conditions require specifying the field on the boundary of the mapped region, then using the above expression to propagate the boundary values to the interior region. This process is iterated until the desired degree of stability against further computation is reached. The properties of Laplace's equation assure us that the method is indeed convergent, and that the effect of measurement errors is maximal on the boundary. Thus, any interior point is better determined by this smoothing process than by actually making a measurement of the field at that point.

The smoothed field is stored on disk for use by the Monte Carlo program. When the field value is requested at some point $\vec{x}$, linear interpolation across the lattice cell containing $\vec{x}$ is used to obtain the field. The only exception to the rule is when the lattice cell borders a plane of (positive) symmetry for that component. In this case, of course, the local variation must be quadratic. Since the physical size of the mapper does not allow us to come closer than 1.5in from the pole-tips, some trajectories pass outside the region of the map. The B-field for $|y| > 3$in is obtained by using linear

extrapolation based on Maxwell's equations, i.e.,

$$\frac{\partial B_y}{\partial x} = \frac{\partial B_x}{\partial y}$$

$$\frac{\partial B_y}{\partial y} = -\left[\frac{\partial B_x}{\partial x} + \frac{\partial B_z}{\partial z}\right]$$

$$\frac{\partial B_y}{\partial z} = \frac{\partial B_z}{\partial y} \quad .$$

Thus, the computation of derivatives that would require points outside the lattice is replaced by derivatives of other field components on the face of the lattice.

2. Tracking Methods

The motion of charged particles through the magnetic field is governed by the Lorentz force law

$$\frac{d\vec{p}}{d\tau} = \left[\vec{p} \times \vec{B}\right] ,$$

where τ is the proper time and $\vec{p} = m\frac{d\vec{x}}{d\tau}$. Introducing the differential arc-length of the trajectory, $ds = |d\vec{x}|$, we can convert the Lorentz law to a form containing only spatial quantities:

$$\frac{d^2\vec{x}}{ds^2} = \frac{e}{pc}\left[\frac{d\vec{x}}{ds} \times \vec{B}\right] \quad .$$

Here we have written $|\vec{p}| = p$, which we know to be a conserved quantity in the absence of electric fields.

However, a straightforward first-order integration of the above form does not lead to momentum conservation. Consider the new momentum $\vec{p}'$ obtained by first-order integration over a step size δs:

$$\vec{p}' = \vec{p} + \delta\vec{p} = \vec{p} + \frac{d\vec{p}}{ds}\delta s$$

$$= \vec{p} + \frac{d}{ds}\left[p\frac{d\vec{x}}{ds}\right]\delta s = \vec{p} + p\frac{d^2\vec{x}}{ds^2}\delta s \quad .$$

Then

$$|\vec{p}'|^2 = |\vec{p}|^2 + \vec{p}\cdot\delta\vec{p} + \left[\frac{d\vec{p}}{ds}\right]^2\delta s^2$$

$$= p^2\left[1 + \left[\frac{d^2\vec{x}}{ds^2}\right]^2\delta s^2\right] \quad .$$

One can easily show that, in describing a circle of radius R in a constant field, this produces an error of order

$$\frac{\delta(p^2)}{p^2} \sim 2n\frac{\delta s}{R} \quad ,$$

which would be on the order of a few percent for δs = 1cm and typical JANUS pions.

This error clearly results from ignoring second-order and higher terms in our expansion for $\vec{p}'$. Defining $\vec{u} = \frac{d\vec{x}}{ds}$ and $\epsilon = \frac{e}{pc}$ (note that $\vec{p} = p\vec{u}$), we can write a second-order expansion for both $\vec{x}$ and $\vec{u}$ as

$$\vec{x}(s+\delta s) = \vec{x}(s) + \frac{d\vec{x}}{ds}\delta s + \tfrac{1}{2}\frac{d^2\vec{x}}{ds^2}\delta s^2 + \ldots \qquad (C.1)$$

$$\vec{u}(s+\delta s) = \vec{u}(s) + \frac{d\vec{u}}{ds}\epsilon s + \tfrac{1}{2}\frac{d^2\vec{u}}{ds^2}\delta s^2 + \ldots$$

In this notation, the Lorentz law is $\frac{d\vec{u}}{ds} = \epsilon\left[\vec{u} \times \vec{B}\right]$. This may be used to expand the second derivative in the equation for $\vec{u}(s+\delta s)$:

$$\frac{d^2\vec{u}}{ds^2} = \varrho\frac{d}{ds}\left[\vec{u} \times \vec{B}\right] \qquad (C.2)$$

$$= \varrho\left[\frac{d\vec{u}}{ds} \times \vec{B}\right] + \varrho\left[\vec{u} \times \frac{d\vec{B}}{ds}\right]$$

$$= \varrho^2\left[\left[\vec{u} \times \vec{B}\right] \times \vec{B}\right] + \varrho\left[\vec{u} \times \frac{d\vec{B}}{ds}\right]$$

Our final form for the equations of motion is then

$$\vec{x}(s+\delta s) = \vec{x}(s) + \vec{u}(s)\delta s + \tfrac{1}{2}\varrho\left[\vec{u} \times \vec{B}\right]\delta s^2 + \ldots \qquad (C.3)$$

$$\vec{u}(s+\delta s) = \vec{u}(s) + \varrho\left[\vec{u} \times \vec{B}\right]\delta s$$

$$+ \tfrac{1}{2}\varrho\left\{\left[\vec{u} \times (\vec{u}\cdot\nabla)\vec{B}\right] + \varrho\left[\left[\vec{u} \times \vec{B}\right] \times \vec{B}\right]\right\}\delta s^2 + \ldots$$

One may show that step-by-step integration of this system around a circle of radius R leads to a relative error in squared momentum of order $2\pi\left[\frac{\delta s}{R}\right]^3$, a substantial improvement over first-order integration. Typical step sizes of 1cm then lead to negligible tracking errors in propagating $\vec{x}$ and $\vec{p}$ through the field.

3. Energy Loss and Multiple Scattering

The Monte Carlo calculates the energy loss and multiple scattering in the target, the air, and all detectors. The detectors are assumed sufficiently thick so that the effect of interactions within them are well described by an integrated distribution (as opposed to a probability distribution for different types of interactions that create the cumulative distribution). Thus, the energy loss distribution is assumed to be given by Landau theory,[87] i.e.,

$$P(\lambda)d\lambda = \frac{1}{\sqrt{(2\pi)}} e^{-\frac{1}{2}\left[\lambda + e^{-\lambda}\right]} d\lambda \qquad (C.4)$$

Here, λ is a reduced energy loss variable,

$$\lambda = \frac{\Delta E - \Delta E_p}{Bx} ,$$

x is the thickness, B is a constant for a given material, ΔE_p is the most probable energy loss, and ΔE is the actual energy loss. In the limit of very large x, most ΔE values lead to $\lambda < 1$, and it easy to show that Eqn. C.4 becomes a Gaussian centered on ΔE_p. This condition is seldom met in practice, thus necessitating use of the complete theory. This leads to a broader distribution in energy loss, with a characteristic high energy loss tail. For the sake of completeness, we give the detailed forms of the parameters used: The most probable energy loss for a projectile of charge Z_{inc} and velocity β, incident on a material of atomic number Z, atomic mass A, and density ρ, is given by

$$\Delta E_p = Bx \left\{ \log \frac{mc^2 \beta^2 Bx}{I^2(1-\beta^2)} - \beta^2 + 0.37 \right\} , \qquad (C.5)$$

where

$$B = \frac{Z}{A} \rho \frac{K}{\beta^2} ,$$

$$K = \frac{2\pi N_A Z_{inc}^2 e^4}{mc^2} \cong 0.154 \text{MeV/gm cm}^{-2} .$$

The ionization potential I is well-approximated by $I \cong 16 \cdot (Z)^{0.9}$ eV.

Multiple scattering is included through a Gaussian approximation[90] to the actual Moliere distribution. Thus, the probability of

scattering into a solid-angle element $d\Omega$ in traversing a thickness L of material is given by

$$P(\Omega)d\Omega = \frac{1}{\pi\theta_o^2} e^{-\theta^2/\theta_o^2} d\Omega \qquad (C.6)$$

where L_R is the radiation length of the material and

$$\theta_o = \frac{20 \text{ MeV/c}}{p\beta} \cdot z_{inc} \sqrt{\frac{L}{L_R}} \left[1 + \frac{1}{9} \log_{10} \left(\frac{L}{L_R} \right) \right] .$$

This approximation is good to 10% or better. The effects of nuclear single scattering, either through the strong or the Coulomb interaction, are neglected. In magnitude, these effects are the order of 1-2%. They are further reduced in the data analysis through the imposition of cuts such as the " δr-cut " and target traceback requirements.

4. Muon Decay

The Monte Carlo allows us to estimate what percentage of our pions are actually muons coming from the decay $\pi^- \rightarrow \mu^- + \bar{\nu}_\mu$, and what the effect of these muons are on our momentum resolution. Approximately 10% of the pions accepted after all cuts are in actuality muons. However, those cuts, in particular the δr-cut, are such that only those muons are accepted which come from a decay on the exit side of the spectrometer, and which have a direction essentially in that of the original pion. Thus, the momentum resolution is not substantially degraded. All resolutions quoted in Chapter IV and presented in Figures 9-11 include the effects of these decay muons.

APPENDIX D

MEAN MULTIPLICITY DISTRIBUTIONS

In this appendix we show that our two-pion trigger requirement is equivalent to a central collision trigger. We do so by first establishing the correlation between pion multiplicities and total charge multiplicities, then show that our requirement of two pions in the JANUS spectrometer biases the event selection strongly towards those events containing a high pion multiplicity, and thus a high total charge multiplicity. The total charge multiplicity is then converted to a mean impact parameter via a geometrical model for the collision process.

As shown in Figure 14, the results of Ref. 78 demonstrate that $\langle M_\pi \rangle$, the mean negative pion multiplicity, is linearly proportional to Q, the total number of participant protons. (Incidentally, this result, for 1.8 A·GeV ^{40}Ar + KCl, indicates that pion reabsorption is not a significant effect for this reaction.) Due to the hundreds of contributing partial waves, geometric concepts for total cross-sections are expected to apply in this energy regime.[3] We may therefore interpret the total proton multiplicity in terms of impact parameter by using an analytic result due to Swiatecki (as presented in Ref. 91) for the number of participant protons Q in a collision at impact parameter b between two equal-mass ions of charge Z:

$$Q(b) \approx 2Z(1-\beta)^2\left[1+\left(\frac{3}{\sqrt{2}}-1\right)\beta\right] \qquad (D.1)$$

where $\beta \equiv b/b_m$, and b_m is the maximum impact parameter, i.e., $b_m = 2R$. Here the normalization is such that $Q(b=0)=2Z$.

In light of the very rough nature of these arguments, and in the interests of simplicity, we propose to further approximate Eqn. D.1 as

$$\begin{aligned} Q(b) &\approx (1-\beta)^2\left[1+1.12\beta\right] \\ &\approx (1-\beta)\cdot(1-\beta^2) \\ &\approx (1-\beta) \quad \text{for } \beta \ll 1. \end{aligned} \qquad (D.2)$$

This approximation is good to (at worst) 20% for $\beta < 0.5$. Since we will be largely concerned with central collisions, this linear form for Q(b) will be adequate for our purposes.

To estimate the mean pion multiplicity for our trigger, we use the data of the UCR streamer chamber group.[92] This data consists of approximately 3000 1.8 A·GeV ^{40}Ar + KCl events taken in the inelastic trigger mode, which corresponds to roughly 85% of the total reaction cross section. All negative tracks in each event have been scanned and momentum-analyzed. We may therefore selectively examine those events that satisfy a one or two pion trigger in the JANUS spectrometer. From those events we may also obtain the total negative pion multiplicity, and thereby determine the mean multiplicity for the two triggers. The JANUS trigger requirement is defined as all pions satisfying $35^\circ \lesssim \theta_\pi \lesssim 55^\circ$ and 200 MeV/c $\lesssim p_\pi \lesssim$ 1000 MeV/c, where both

quantities are measured in the lab.

The results of such an analysis are shown in Figure 15, along with fits to a Poisson distribution. Figure 15a shows that the pion multiplicity distribution associated with the one-pion trigger for JANUS. The distribution is approximately Poisson, with a mean of 4.30 ± 0.05. This already represents a bias away from peripheral collisions, in that the unbiased pion multiplicity for this reaction is only slightly greater than 3. The results for a two-pion trigger "in" JANUS is are shown in Figure 15b. This is actually the multiplicity for all events with two pions satisfying the above trigger cuts, regardless of the azimuthal angle between the two pions. Therefore, the conclusions drawn from Figure 15b depend on the assumption of statistical independence of the pion momentum spectrum as a function of azimuthal angle between the pions. While this independence is not strictly the case, (fortunately, for the author of this thesis), the net effect on trigger bias considerations should be small. At any rate, the mean pion multiplicity for the JANUS two-pion trigger is 6.14 ± 0.18.

Now that our pion multiplicity bias is established, we may use Eqn. D.2 in conjunction with Fig. 14 to relate the mean pion multiplicity as a function of Q, $\langle M_\pi(Q) \rangle$, to Q(b). In our approximation, the relation is linear, thus

$$\langle M_\pi(Q) \rangle = n_{max}(1 - \beta) \qquad (D.3)$$

with $n_{max} \simeq 7.2$ for this data. We have taken the liberty of placing the impact parameter scale so derived on the upper horizontal axis of

Fig. 14. This allows us to translate a given pion multiplicity directly into impact parameter. For example, for the two-pion trigger, $\langle M_\pi \rangle = 6.14$ implies $Q \simeq 29$, which gives $\frac{b}{b_m} = \frac{1}{4}$. Assuming $b_m \simeq 2r_o A^{1/3}$, we get, with $r_o = 1.2$fm, $\langle b \rangle \simeq 1.2$fm. Similariy, a one-pion trigger gives $\langle b \rangle \simeq 3.3$fm, while an unbiased trigger would give $\langle b \rangle = \frac{2}{3} b_m = 5.5$fm.

As a consistency check on Eqn D.3, we note that it gives a definite prediction for $\langle n_\pi \rangle$, the average pion multiplicity over all impact parameters:

$$\langle n_\pi \rangle = \frac{\int d^2b \, \langle M_\pi(b) \rangle}{\int d^2b} \qquad (D.4)$$

$$= n_{max} \cdot \frac{\int d^2b \left[1 - \frac{b}{b_m} \right]}{\int d^2b}$$

$$= n_{max} \cdot \left[1 - \frac{\langle b \rangle}{b_m} \right]$$

$$= \frac{1}{3} n_{max} \quad .$$

This gives $\langle n_\pi \rangle \simeq 2.4$, as opposed to the observed value of 3. However, given the schematic features of this model, we feel that this is an acceptable degree of consistency, particularly in light of the experimental difficulties in obtaining bias-free multiplicity distributions. (The trigger requirement is usually such that the most peripheral collisions are missed).

Lest one regard these conclusions as completely model dependent, we present an alternative approach. The GSI streamer chamber central collision trigger corresponds to a reaction cross section of approximately 180mb.[93] Assuming $\sigma = \pi b^2$, this is equivalent to a maximum impact parameter of 2.4fm. The observed pion multiplicity distribution for this trigger is Poisson, with $\langle n_\pi \rangle = 5.81$. The mean impact parameter is 2/3 this value, or 1.6fm. Thus, a mean pion multiplicity of roughly 6 is indeed consistent with a mean impact parameter of about 1.5fm, as determined by actual cross section measurements.

APPENDIX E

BACKGROUND FLUCTUATIONS

In this appendix, we address the question of statistical errors in the background spectrum generated by the mixing of pions from different events. What we wish to determine is "Given n background events in some bin, what is the expected error σ_n?" In the following we show that: 1.) A simple model for background generation shows that $\sigma_n \simeq n^{3/4}$, not $\sqrt{n}$; 2.) The fluctuations in the actual background events support the $n^{3/4}$ model; and 3.) This has non-trivial consequences for the generation and analysis of correlation functions.

1. A Model for Background Errors

To understand the origin of the $n^{3/4}$ rule, consider the following thought experiment:[94] Assume we wish to calculate the area of the region Ω in Fig. 16 using a Monte Carlo technique. For simplicity, we assume Ω is rectangular, with sides of length l_x and l_y, contained within a square region of linear extent L. The most straightforward integration method consists of picking M random points in the large square region. The expected number in Ω is of course then given by $m_\Omega = \frac{l_x l_y}{L^2}$, with fluctuations about this value of order $\sigma_m \simeq \sqrt{m}$. This is precisely in accord with our usual notions of the statistical behavior of large numbers.

Now suppose we try to circumvent the requirement of generating M random points in the plane by instead picking only N random numbers r_i , $i = 1 \rightarrow N$, then generating $\frac{1}{2}N(N-1)$ "random" points in the plane via $\vec{x}_{ij} \equiv (r_i L, r_j L)$. It would appear that for only $N \simeq \sqrt{2M}$ random numbers, we could obtain the same statistical accuracy in determining Ω as by generating all M random points. Certainly this approach will produce the correct mean value for Ω: The mean number of random numbers along the x-axis will be $n_x = \frac{l_x}{L}N$, similarly $n_y = \frac{l_y}{L}N$. The mean number of points in Ω is then $n_\Omega = n_x n_y$, and thus the average value obtained for Ω is $\Omega = \frac{n_\Omega}{N^2} \cdot L^2 = l_x l_y$. However, being properly suspicious of getting something for nothing, we now use standard error propagation methods to calculate how accurately this method determines Ω. Assuming for now that n_x and n_y are statistically independent, and that their individual errors go as $\sqrt{n}$, we have

$$\sigma^2(n_\Omega) = \left[\frac{\partial n_\Omega}{\partial n_x}\right]^2 \sigma^2(n_x) + \left[\frac{\partial n_\Omega}{\partial n_y}\right]^2 \sigma^2(n_y) \qquad \text{(E.1)}$$

$$= n_y^2 n_x + n_x^2 n_y$$

$$= (n_y n_x) \cdot [n_x + n_y]$$

$$= n_\Omega \left[(l_x + l_y)\frac{N}{L} \right]^{1/2} .$$

Specializing to the case where $l_x = l_y$, we immediately obtain from the above $\sigma(n_\Omega) = \sqrt{2} \cdot n_\Omega^{3/4}$. Thus, the errors due to this method are

much larger than those from the usual Monte Carlo estimate of area. It should come as no surprise that to get the same relative accuracy as from M truly random points requires $N \simeq M^2$.

In the above derivation, we have assumed that Ω is located far from the diagonal line given by x=y. If this is not the case, as in the case of Ω' in Fig. 16, we cannot regard n_x and n_y as statistically independent, and the above result becomes $\sigma(n_{\Omega}) = 2n_{\Omega}^{3/4}$. It is easy to show that in d dimensions, the fluctuations in n_V, the mean number in a sub-volume V, are given by $\sigma(n_V) = \sqrt{n_V^p}$, with $p = 1 - \frac{1}{2d}$.

2. Numerical Studies

While the derivation of the previous section is quite straightforward, it is by no means clear that it applies directly to different-event mixing in the analysis of two-pion correlation data. There certainly are suggestive similarities: The N random numbers correspond to N pion momenta, the region Ω then is analogous to a given bin in $\vec{p}_1 - \vec{p}_2$, etc. However, a typical correlation analysis projects the difference of 3-dimensional momentum vectors into some complicated sub-space of relative momentum and energy. We now show that it is at least plausible that the background fluctuations are consistent with an $n^{3/4}$ rule.

We investigate the background errors using the variable Γ^2, where

$$\Gamma^2 = \sum_{ij} \frac{\left[A_{ij} - B_{ij} \right]^2}{\sigma^2_{ij}(A) + \sigma^2_{ij}(B)} \quad , \tag{E.2}$$

and the sum over i and j represents a summation over the q and q_o bins of the relative momentum spectrum. Here B_{ij} is the number of background events in that bin, and A_{ij} is some other distribution that should be identical to B_{ij} in the limit of infinite statistics. We assert without proof that, provided the σ's are properly chosen, 1.) The mean value of Γ^2 is n_D, and 2.) Γ^2 should be distributed as a chi-squared distribution for n_D degrees of freedom, where n_D is the number of bins in our sum over i and j. To support these assumptions we note that a.) The expectation value of Γ^2 is n_D, since if A and B are independent quantities with the same mean value, $\left\langle (A_{ij} - B_{ij})^2 \right\rangle = \sigma^2(A_{ij}) + \sigma^2(B_{ij})$; and b.) Γ^2 is indeed distributed as chi-squared for n_D if A and B are from Gaussian distributions with the same mean and dispersion for a given bin.

As our known distribution, we take the real events for $|\vec{q}| > 150$ MeV/c, where we have every expectation of no correlation. (The advantage of this choice is that the σ_A's are known.) We test this against a scaled background distribution over the same interval. By varying the functional form of $\sigma_B(B)$, we can find what form for σ_B produces $\Gamma^2 \simeq n_D$. As our functional form for σ_B we take the general d-dimensional result, i.e., $\sigma_B = d \cdot B^{1 - \frac{1}{2d}}$. For two different data sets we find $p = 0.75 \pm .02$ and $p = 0.77 \pm .02$, where $p = 1 - \frac{1}{2d}$. The errors are assigned by invoking Assumption #2 detailed above, then varying d until the change in Γ^2 corresponds to a 68% confidence

level for a chi-squared variate of n_D degrees of freedom.

It would thus appear that statistical errors of the background support the $n^{3/4}$ result from the first section. We note that the value of p derived above depends only on Assumption #1. Assumption #2 is required to assign errors to the value of p so obtained, but its validity does not affect the value of p.

3. Implications for Correlation Analyses

In this section we show that the $n^{3/4}$ form of the background errors has non-trivial consequences for the analysis of two-pion data. More specifically, we obtain two simple rules governing the number of events required in the generation of background spectra via mixing momenta from different events.

Suppose we wish to create a background spectrum with negligible fluctuations relative to those in the corresponding bin for the real events. We assume that the background is being created from the same data set as the real events. Let the number of real events be N, and let f denote the fraction of these events that fall into some bin i, i.e., $n_i = fN$. Say we take some fraction of real events $M = gN$ to generate a background containing a total of $\frac{g^2}{2}N(N-1)$ combinations. The expected number in the i-th bin is then $m \simeq \frac{f}{C_2} \cdot \frac{g^2}{2} \cdot N^2$. Here C_2 is the value of the correlation function for this bin. The correlation function is of course proportional to $\frac{n}{m}$, with errors proportional to

$$\sigma^2(C_2) \sim \left(\frac{n}{m}\right)^2 \left[\left(\frac{\sigma_n}{n}\right)^2 + \left(\frac{\sigma_m}{m}\right)^2 \right] \quad . \tag{E.3}$$

We desire a background such that the error on C_2 is determined almost entirely by the real events. This implies that

$$\left(\frac{\sigma_m}{m}\right)^2 << \left(\frac{\sigma_n}{n}\right)^2 \quad .$$

Substituting the above values for m and n, and assuming $\sigma_m = 2n^{3/4}$, we obtain the condition

$$\frac{1}{g}\sqrt{2C_2 f} << \frac{1}{4} \quad . \tag{E.4}$$

This result is independent of the original number of events N, but it does depend on both the fraction g used in the background generation and f, the bin size. The requirement that g should be as large as possible certainly is in accord with our intuition. The surprising result is the bin-size dependence. Setting g = 1, the above condition becomes

$$C_2 f < \frac{1}{32} \simeq 3\% \tag{E.5}$$

This inequality is satisfied for most, but not all, of the bins used in our correlation analysis. Since the Principle of Maximum Likelihood fitting procedure requires that the background fluctuations be negligible compared to the those of the real events, one might object to inclusion of these bins in the fit. However, by explicitly minimizing a quantity that includes the background errors (the Γ^2 defined in the previous section), we have shown that in all cases the fitted parameters are substantially the same as those obtained by PML

methods.

To summarize the results of this section, it has been shown that 1.) The bin sizes in this form of correlation analysis must be kept as small as possible (keeping in mind the requirements of resolution and reasonable statistics per bin) and 2.) Point 1 usually means that all, rather than some subset, of the real events must be used to create the background spectrum.

APPENDIX F

GAMOW COULOMB CORRECTIONS

In this appendix we discuss in further detail the Gamow correction for the two-pion relative Coulomb interaction. In particular, we are interested in the effects of emission by a pion source distributed in space and time over typical nuclear dimensions. We begin by briefly reviewing the usual derivation of the Gamow factor. The approach is that of Davydov,[95] although the notation has been somewhat altered. We use units such that $\hbar$ appears explicitly.

The Schrodinger equation for the relative motion of two like-charged particles in their mutual Coulomb field is

$$-\frac{\hbar^2}{2\mu}\nabla^2\psi_k(\vec{r}) + \frac{e^2}{r}\psi_k(\vec{r}) = \frac{\hbar^2 k^2}{2\mu}\psi_k(\vec{r}) \quad , \tag{F.1}$$

where

$$\mu = \frac{m_1 m_2}{m_1 + m_2} = \tfrac{1}{2} m_\pi$$

and

$$\vec{k} = \frac{m_2\vec{p}_1 - m_1\vec{p}_2}{m_1 + m_2} = \tfrac{1}{2}(\vec{p}_1 - \vec{p}_2) = \tfrac{1}{2}\vec{q} \quad .$$

In the above, the expressions for μ and $\vec{k}$ have been specialized to the case $m_1 = m_2 = m_\pi$. We note in passing that the relativistically correct equation for the relative motion of two pions is the Klein-Gordon equation. However, as we shall see, the Gamow correction is important only for relative velocities $v_{rel} \simeq \frac{c}{137}$, so that the non-

relativistic approximation is expected to be valid. Also neglected here is the symmetrization requirement on the two-pion wave function. This may be imposed at a later stage of the calculation with no loss of information.

The solution to Eqn. F.1 corresponding to initial motion along the z-axis is most easily obtained in parabolic coordinates defined by $(u,v) = (r-z, r+z)$. Writing

$$\Psi_k(\vec{r}) = e^{\frac{ik}{2}(v-u)} \phi(u) \quad ,$$

one may show that ϕ must solve the equation

$$u\phi'' + (1-iku)\phi' - \eta k\phi = 0 \tag{F.2}$$

with $\eta = \frac{\mu e^2}{\pi^2 k}$. The solution to the above equation is given by the confluent hypergeometric function F, thus $\phi(u) = CF(-i\eta, 1, iku)$, where C is a normalization constant.

The Gamow factor G_o, defined as the ratio of the density at the origin to the asymptotic density,

$$G_o = \frac{|\Psi_k(\vec{r} = 0)|^2}{|\Psi_k(\vec{r} \to \infty)|^2} \tag{F.3}$$

may then be calculated using the known asymptotic properties of the confluent hypergeometric function. It is thus straightforward to show that

$$G_o = \frac{|\phi(u = 0)|^2}{|\phi(u \to \infty)|^2} = \frac{2\pi\eta}{e^{2\pi\eta} - 1} \tag{F.4}$$

This is the usual Gamow factor.

The above derivation suggests that the effect of a distributed source may be incorporated by smearing the density at the origin over the source size, that is,

$$|\Psi_k(\vec{r}=0)|^2 \rightarrow \int |\Psi_k(\vec{r})|^2 \rho(\vec{r})\,d\vec{r} \quad , \tag{F.5}$$

where $\rho(\vec{r})$ gives the distribution of relative separations between the two pions. The above equation has been derived more rigorously by Koonin,[5] along with an explicit form for $\rho(\vec{r})$ that includes the effects of temporal separation between the two pions. Taking Gaussians for the space and time distributions for the individual pion emission points $(t_i,\vec{r}_i)$,

$$\rho_r(\vec{r}_i) \sim e^{-r_i^2/R_o^2}$$

and

$$\rho_t(t_i) \sim e^{-t_i^2/\tau^2} \quad ,$$

he obtains

$$\rho(\vec{r}) = \int d\vec{R}\,dt_1\,dt_2\; \rho_r(\vec{R}+\tfrac{1}{2}\vec{r}+\vec{V}t_2)\rho_r(\vec{R}-\tfrac{1}{2}\vec{r}+\vec{V}t_1)\rho_t(t_1)\rho_t(t_2) \tag{F.6}$$

$$= \frac{1}{(2\pi)^{3/2}sR_o^2} \exp\left\{ \frac{-1}{2R_o^2}\left[r^2 - \left[\frac{\vec{V}\cdot\vec{r}}{s}t\right]^2\right]\right\} \quad .$$

Here the frame is assumed such that the individual pion sources are at rest, $\vec{V} = (\vec{p}_2 + \vec{p}_2)/2m_\pi$, and $s^2 = V^2\tau^2 + R_o^2$. The normalization is such that $\int \rho(\vec{r})\,d\vec{r} = 1$.

Before proceeding with explicit evaluation of the integral in Eqn F.5, we must now incorporate the symmetrization requirement into

the relative motion wave function ϕ. Using the small u expansion for $F(-i\eta,1,iku)$, we have for the unsymmetrized ϕ

$$\phi(u) \cong C\left[1 + (-i\eta)(iku) + \frac{1(-i\eta)(-i\eta+1)}{2!}(iku)^2 + \ldots\right]$$

Since $u = r-z$, the symmetrization is accomplished via $z \rightarrow -z$, so the symmetrized form with the same value as $u \rightarrow 0$ is given by

$$\phi_s(u) \cong C\left[1 + ik\eta u + \frac{i\eta}{4}k^2(r^2+z^2) + \ldots\right]$$

so that

$$|\phi_s(u)|^2 \cong |C|^2\left[1 + 2k\eta r + \tfrac{1}{2}k^2\eta^2(r^2+z^2) + \ldots\right] . \qquad (F.7)$$

The modified Gamow factor G_{mod} is then given by

$$\begin{aligned} G_{mod} &= \int d\vec{r}\rho(\vec{r})\,|\phi_s(u)|^2 \qquad (F.8)\\ &\cong G_o\int d\vec{r}\rho(\vec{r})\left[1 + 2k\eta r + O(k\eta r)^2 + \ldots\right]\\ &\cong G_o\left[1 + 2k\eta\langle r\rangle + \ldots\right] . \end{aligned}$$

(This result has been obtained by a somewhat different argument by the authors of Ref. 84)

This form is in accord with our intuitive expectations. The suppression for low relative momentum due to the Gamow function is reduced due to the spatial extent of the source. Before evaluating the integral for $\langle r\rangle$, we may estimate the size of the correction to G_o:

$$2k\eta\langle r\rangle = 2k\,\frac{\mu e^2}{\pi^2 k}\langle r\rangle \qquad (F.9)$$

$$= \frac{1}{137} \cdot \frac{m_\pi <r>}{\hbar c} \cong \tfrac{1}{2}\,\% \text{ per fermi of } <r> \quad .$$

Therefore, we anticipate that so long as $c\tau \sim R_o$, this correction will be small for nuclear dimensions. Explicit evaluation of <r> using $\rho(\vec{r})$ gives

$$<r> = \sqrt{\frac{2}{\pi}}\, R_o \left[\frac{s}{R_o} + \frac{R_o}{2V\tau} \log\left[\frac{s + V\tau}{s - V\tau} \right] \right] \quad .$$

Substitution of realistic nuclear parameters shows that <r> is not drastically different from R_o or τ, leading to the conclusion that the effect of the distributed source in indeed small for RHIC.

APPENDIX G

THE INTERPRETATION OF GAUSSIAN SOURCE PARAMETERS

In this appendix, we relate the use of Gaussian source density distributions to more conventional descriptions of nuclear density profiles. We also explore the relation between the R and τ parameters, and examine the time-development of pions in Monte Carlo cascade calculations.

1. Gaussian Spatial Distributions

The normalized Gaussian source distribution used in this analysis is given by

$$\rho(\vec{r}) = \frac{1}{\pi^{3/2} R^3} \cdot e^{-r^2/R^2} \quad . \tag{G.1}$$

We wish to find the value of R such that this distribution best describes a uniform distribution of radius R_u. Equating the first moments of these two distributions, we obtain

$$R = \frac{3\sqrt{\pi}}{8} R_u \simeq \frac{R_u}{1.50} \quad .$$

Similarly, equating second moments, the result is

$$R = \sqrt{\frac{2}{5}} R_u \simeq \frac{R_u}{1.58} \quad .$$

More generally, in Ref. 27 it is shown that for $R = R_u/1.52$, the squared Fourier transform of the Gaussian distribution differs from the corresponding transform of the uniform distribution everywhere by less than 2%. Since the squared Fourier transform is the actual

observable of interest in a correlation analysis, the use of the Gaussian parametrization is quite adequate. Furthermore, we note that while nuclear matter in its ground state is to first order described by a uniform distribution, a Gaussian ensemble of productions sites may indeed be a better approximation of the pion source in a heavy ion collision.

2. The Time Dependence of the Pion Source

In this section we motivate the use of a Gaussian to describe the temporal distribution of pion sources based on a heuristic model for the collision process. Consider the collision of two equal-mass nuclei in the center-of-mass frame. Assume that each nucleus is described in this frame by a Lorentz-contracted Gaussian spatial distribution, moving with velocities $\pm\beta_{cm}$. Thus,

$$\rho_{\pm}(\vec{r}) = e^{-\left[x^2 + y^2 + \gamma_{cm}^2(z \pm \beta_{cm} t)^2\right]/R^2} .$$

The pion production rate at some point $\vec{r}$ is then given by

$$\frac{dn_{\pi}(\vec{r})}{dt} = \rho_{-}(\vec{r})\rho_{+}(\vec{r})\sigma v_{rel} .$$

If we ignore the velocity dependence of σv and pion reabsorption, the total pion production rate is given by

$$\frac{dn_{\pi}}{dt} \sim \int d\vec{r}\, \rho_{-}(\vec{r})\rho_{+}(\vec{r}) \sim e^{-2\beta_{cm}^2\gamma_{cm}^2 t^2/R^2} \cdot \left[\text{ a spatial integral }\right] \quad \text{(G.2)}$$

We have therefore obtained the not too surprising result that the collision of two Gaussian spatial distributions gives a collision rate that is Gaussian in time, $p(t) \sim e^{-t^2/\tau^2}$, with $\tau = \dfrac{R}{\sqrt{2}\beta_{cm}\gamma_{cm}}$. In

reality, this should be viewed as a lower limit for τ, as we have ignored effects such as reabsorption and deceleration of the colliding nuclei, which will tend to increase τ.

3. Comparison to Monte Carlo Calculations

The cascade code of Cugnon et al.[96] provides a quantitative picture for the space-time evolution of a heavy ion collision. Their results for the collision of $^{40}Ca + {}^{40}Ca$ ions are presented in Fig. 28. Two curves are shown, the solid one giving the production of free pions plus delta resonances, while the dotted curve gives the just the number of free pions as a function of time. Maximum overlap occurs for $t \simeq 5.1$ fm/c. The circular and triangle points are the results of integrating

$$\frac{dN}{dt} = N_o e^{-t^2/\tau^2}$$

for appropriately chosen values of τ. Thus, e.g., for the $N_\pi + N_\Delta$ curve we have for $t > 5.1$ fm/c

$$N(t) = \tfrac{1}{2} N_\infty \left[1 + \mathrm{erf}\left(\frac{t-5.1}{\tau}\right) \right] ,$$

with $\tau = 2.31$ fm/c. A similar expression is obtained for the free pion production curve, with $\tau = 5.55$ fm/c.

These expressions fit the observed time dependences quite well, particularly for the total production rate (the closed circles). The value of τ required, 2.31 fm/c, is reasonably close to that predicted by the method of the previous section, which gives $\tau \geq 1.91$fm/c. The code predicts a much slower production rate of free pions than one

would expect from the simple overlap of the nuclear densities. This is due to the reabsorption, energy dependent production cross sections and finite delta lifetimes. Nonetheless, the time development corresponds roughly to that predicted by a Gaussian model.

We close by noting that the initial spatial distribution of nucleons in this cascade code is assumed to be a spherical, not Gaussian region. However, the results of Fig. 28 are obtained by averaging over a number of "runs", with one run per collision. Presumably the approach to a Gaussian temporal development of the cascade is a consequence of the Central Limit theorem.

REFERENCES

1. Proceedings of the Second High Energy Heavy Ion Summer Study, LBL-3675, Berkeley, July 15-26, 1974.

2. J.P. Sullivan, J.A. Bistirlich, H.R. Bowman, R. Bossingham, T. Buttke, K.M. Crowe, K.A. Frankel, C.J. Martoff, J. Miller, D.L. Murphy, J.O. Rasmussen, W.A. Zajc, O. Hashimoto, M. Koike, J. Peter, W. Benenson, G.M. Crawley, E. Kashy and J.A. Nolen, Jr., Phys. Rev. C25, 1499 (1982).

3. S. Nagamiya and M. Gyulassy, LBL-14035, to appear as a chapter in Advances in Nuclear Physics, Plenum pub. Corp., New York, NY.

4. I. Tanihata, S. Nagamiya, S. Schnetzer, and H. Steiner, Phys. Lett. 100B, 121 (1981).

5. S.E. Koonin, Phys. Lett. 70B 43 (1977).

6. Z.Zarbaksh, A.L. Sagle, F. Brochard, T.A. Mulera, V. Perez-Mendez, I. Tanihata, J.B. Carroll, K.S. Ganezer, G. Igo, J. Oostens, D. Woodard, and R. Sutter, Phys. Rev. Lett. 46, 1268 (1981).

7. M. Gyulassy, K.A. Frankel, and H. Stocker, Phys. Lett. (in press), [Preprint, Lawrence Berkeley Laboratory Report LBL-13379 (1981)].

8. T.D. Lee and G.C. Wick, Phys. Rev. D9, 2291 (1974).

9. B. Banerjee, N.K. Glendenning, and M. Gyulassy, Nucl. Phys. A361, 326 (1981).

10. M. Gyulassy, Nucl. Phys. A354, 395 (1981).

11. A. Pais, Rev. Mod. Phys. 51, 863 (1979).

12. Thermal Physics, C. Kittel, John Wiley and Sons, New York, p. 260 (1969).

13. The Quantum Theory of Light, R. Loudon, Clarendon Press, Oxford (1973).

14. A. Einstein, Sitzungsber. Preuss. Akad. Wiss. Phys. Math. Kl., p.3 (1925).

15. R. Glauber, private communication.

16. The Intensity Interferometer, R. Hanbury Brown, Taylor and Francis, London (1974).

17. R. Hanbury Brown, R.C. Jennison, M.K. Das Gupta, Nature, 170, 1061 (1952).

18. Threshold Signals, J.L. Lawson and G.E. Uhlenbeck, McGraw-Hill, New York (1950).

19. The Principles of Quantum Mechanics, P.A.M. Dirac, Oxford at the Clarendon Press, Oxford (1949).

20. A. Adam, L. Janossy, and P. Varga, Acta Phys. Hung. 4, 301 (1955).

21. E. Brannen and H.I.S. Ferguson, Nature, 178, 481, (1956).

22. G.I. Taylor, Proc. Cam. Phil. Soc. Math. Phys. Sci. 15, 114, (1909).

23. E.M. Purcell, Nature, 178, 1449 (1956).

24. Rutherford Memorial Lecture, as contained in Rutherford at Manchester, J.B. Birks, ed., W.A. Benjamin Inc., New York (1963).

25. G.I. Kopylov and M.I.Podgoretskii, Sov. JETP 69, 414 (1975).

26. G. Cocconi, Phys. Lett. 49B, 459 (1974).

27. G. Goldhaber, S. Goldhaber, W. Lee, A. Pais, Phys. Rev. 120, 300 (1960).

28. E. Fermi, Prog. Theor. Phys. 5, 570 (1950).

29. G.R. Lynch and N.H. Xuong, Phys. Rev. 128, 1849, (1962).

30. T. Ferbel, A. Firestone, J. Sandweiss, H.D. Taft, M. Gailloui, T.W. Morris, W.J. Willis, A.H. Bachman, P. Baumel, and R.M. Lea, Phys. Rev. 143, 1096 (1966).

31. R.A. Donald, D.N. Edwards, R.S. Moore, E.J.C. Read, S. Reucroft, T. Buran, A.G. Frodesen, S. Sire, P. Saetre, A. Bettini, S. Limentani, L. Peruzzo, R. Santangelo, and S. Sartori, Nucl. Phys. B11, 551 (1969).

32. J. Bartke, O. Czyzewski, J.A. Dansyz, A. Eskreys, J. Loskiewicz, P. Malecki, J. Zaorska, K. Eskreys, K. Juszczak, D. Kisielewska, W. Zielinski, M. Szeptycka, K. Zalewski, G. Pichon, and M. Rumpf, Phys. Lett. 24B, 163 (1967).

33. K. Boesebeck, G. Kraus, K. Rumpf, P. Kostka, J. Schreiber, K. Bockmann, H. Drevermann, H. Plothow, B.U. Stocker, P.F.Dalpiaz, W. Kittel, D.R.O. Morrison, R. Stroynowski, H. Wall, T Coghen, K. Dziunikowska, J. Loskiewicz, J. Zaorska, A. Wroblewski, and W. Wojcik, Nucl. Phys. B52, 189 (1973).

34. W.J. Knox, Phys. Rev. 10D, 65 (1974).

35. V.G. Grishin, G.I. Kopylov, and M.I. Podgoretskii, Yad. Fiz. 13, 1116 (1970).

36. G.I. Kopylov and M.I. Podgoretskii, Yad. Fiz. 15, 392 (1972).

37. G.I. Kopylov and M.I. Podgoretskii, Sov. J. Nucl. Phys. 18, 336 (1974).

38. G. I. Kopylov, Phys. Lett. 50B, 472 (1974).

39. G.I. Kopylov and M.I. Podgoretskii, Sov. J. Nucl. Phys. 19 215 (1974).

40. G.I. Kopylov and M.I. Podgoretskii, JINR-E2-9285 (1975).

41. G.I. Kopylov, JINR-E2-8549 (1975).

42. The Feynman Lectures on Physics, R.P. Feynman, R.B. Leighton and M. Sands, Addison-Wesley, Reading, Mass., Vol. 3, p. 4-6 (1965).

43. N.N Biswas, J.M. Bishop, N.M. Carson, V.P. Kenney, W.D. Shepard, L.R. Fortney, A.T. Goshaw, J.W. Lamsa, J.S. Loos, W.J. Robertson, W.D. Walker, G. Levman, V.A. Sreedhar, T.S Yoon, G. Hartner, and P.M. Patel, Phys. Rev. Lett. 37, 175 (1976).

44. E. Calligarich, G. Cecchet, R. Dolfini, A. Giovannini, S. Ratti, M. Tirelli, R. Gessaroli, G. Parrini, S. Squarcia, G. Costa, L. Perini, J.L. Lloyd, and R.G. Thompson, Lett. Nuovo Cimento 16, 129 (1976).

45. M. Deutschmann, R. Honecker, H. Kirk, M. Klein, R. Nahnhauer, R. Hartmann, H. Plothow, V.T. Cocconi, M.J. Counihan, S. Humble, G. Kellner, D.R.O. Morrison, P. Schmid, R. Stroynowski, L. Aniola, T. Coghen, K. Dziunikowska, J. Figiel, A. Zalewska, E. Leitner,, J. Stiewe, J. Krolikowski, A. Para, and A.K. Wroblewski, Nucl. Phys. B103, 198 (1976).

46. F. Grard, V.P. Henri, J. Schlesinger, R. Windmolders, E. De Wolf, F. Verbeure, D. Drijard, Y. Goldschmidt-Clermont, A. Grant, and A. Stergiou, Nucl. Phys. B102, 21 (1976).

47. C.Ezell, L.J. Gutay, A.T. Laasanen, F.T. Dao, P. Schublein, and F. Turkot, Phys. Rev. Lett. 38, 873 (1977).

48. M. Deutschmann, H. Kirk, P. Kostka, R. Nahnauer, R. Hartmann, H. Plothow, V.T. Cocconi, J. Figiel, D.R.O. Morrison, J. Bartke, T. Coghen, P. Stopa, K.W.J. Barnham, B. Pollock, B. Bushbeck, M. Markytan, H. Abramowicz, K. Doroba, A. Para, and A.H. Wroblewski, CERN/EP/PHYS 78-1 (1978).

49. M. Goossens, E. De Wolf, J.J. Dumont, M. Gysen, C. Dujardin, F. Grard, H. Blumenfeld, N.K. Nguyen, Z. Strachman, J.P. Laugier, I.V. Ajinenko, G.N. Khromova, V.M. Kubic, S.R. Lugovsky, N.G. Minaev, and V.I. Riadovikov, Nuovo Cimento 48A, 469, (1978).

50. U. Becker, J. Burger, M. Chen, G. Everhart, F.M. Heimlich, T. Lagerlund, J. Leong, D. Novikioff, L. Rosenson, W. Toki, M. Weimer, and D. Lowenstein, Nucl. Phys. B151 357 (1979).

51. N. Angelov, N.O. Akhababyan, O. Balea, V. Boldea, V.G. Grishin, M. Kowalski, T. Ponta, L. Simic, and S. Khakman, Sov. J. Nucl. Phys. 33, 1257 (1981).

52. Yu. D. Bayukov, V.B. Gavrilov, P.V. Degtyarenko, Yu. M. Zaitsev, G.A. Leksin, and D.A. Suchkov, Sov. J. Nucl. Phys. 33, 377 (1981).

53. A.A. Kuznetsov, JINR E1-81-405, submitted to the International Conference on High Energy Physics, Lisbon 9-15 July, 1981).

54. M. Deutschmann, P. Kostka, R. Nahnhauer, K. Bockmann, V.T. Cocconi, D.R.O. Morrison, J. Bartke, T. Coghen, J. Figiel, P. Stopa, K.J.W. Barnham, B. Pollock, R. Buschbeck, M. Markytan, A. Para, and A.K. Wroblewski, CERN/EP/PHYS 82-43 (1982).

55. G. Goldhaber, LBL-13291, presented at the European Physical Society International Conference on High Energy Physics, Lisbon, Portugal, July 9-15 (1981).

56. A. Giovannini, G.C. Mantovani, and S.P. Rattti, La Rivista del Nuovo Cimento, 2, No. 10 (1979).

57. F.B. Yano and S.E. Koonin, Phys. Lett. 78b, 556 (1978).

58. M. Gyulassy, S.K. Kauffmann, and L.W. Wilson, Phys. Rev. C20, 2267 (1979).

59. S.Y. Fung, W. Gorn, G.P. Kiernan, J.J. Lu, Y.Y. Oh, and R.T. Poe, Phys. Rev. Lett. 41, 1592 (1978).

60. Alma-Ata-Baku-Belgrade-Bucharest-Budapest-Cracow-Dubna-Moscow-Prague-Sofia-Tashkent-Tbilisi-Ulan-Bator-Varna- Warsaw-Yerevan Collaboration, JINR-E1-12548 (1979).

61. J.J. Lu, D. Beavis, S.Y. Fung, W. Gorn, A. Huie, G.P. Kiernan, R.T. Poe, and G. VanDalen, Phys. Rev. Lett. 46, 1268 (1981).

62. R. Renfordt, private communication.

63. H. Sato and K. Yazaki, short lecture at the Kikuchi-INS Summer School, FujiYoshida, (1980).

64. T. Nakai and H. Yokomi, Osaka University preprint OUAM-81-4-2, (1981).

65. E.A. Bartnik and K. Rzazewski, Phys. Rev. D18, 4308 (1978).

66. A. Giovannini and G. Veneziano, Nucl. Phys. B130, 61 (1977).

67. G.N. Fowler and R.M. Weiner, Phys. Lett. 70B, 201 (1977).

68. G.N. Fowler, N. Stelte, and R.M. Weiner, Nucl. Phys. A319, 349 (1978).

69. G.N. Fowler and R.M. Weiner, Phys. Rev. D17, 3118 (1978).

70. M. Biyajima, Phys. Lett. 92B, 193 (1980).

71. M. Gyulassy, Phys. Rev. Lett. 48 454 (1982).

72. J. O. Rasmussen, private communication

73. S.R. Olsen, F.A. Kirsten, E.P. Binall, K.L. Lee, N.N. Bhandari, and C.C. Nunnally, LBL-2445 (1973).

74. M. Kellogg, M.M. Minor, S. Schlaer, N. Spencer, R.F. Thomas, H. van der Beken, Los Alamos report LA-7001-M (1978).

75. A.P. Banford, "The Transport of Charged Particles", London, Spon, 1966.

76. H. Wind, Function Parametrization, in Proc. of 1972 CERN Computing and Data Processing School, CERN Report 72-21.

77. J.C. Alder, B. Gabioud, C. Joeseph, J.F. Loude, N. Morel, A. Perrenoud, J.P. Perroud, M.T. Tran, B. Vaucher, E. Winkelmann, D. Renker, H. Schmitt, C. Zupancic, H. Von Fellenberg, A. Frischknecht, F. Hoop, G. Strassner, and P. Truol, Nucl. Instr. and Meth. 160, 93 (1979).

78. K. Van Bibber and A. Sandoval, LBL-12883, to appear in "Heavy Ion Science", Plenum Press, New York, 1982.

79. F. James and M. Roos, Nucl. Phys. B172, 475 (1980).

80. F. James, Comp. Phys. Comm. 20, 29 (1980).

81. CERN Program Library Long Write-up D506 and D516, (1971).

82. S. Nagamiya, M.-C. Lemaire, E. Moeller, S.Schnetzer, G. Shapiro, H. Steiner, and I. Tanihata, Phys. Rev. C24, 971 (1981).

83. R. Brockman, private communication.

84. M. Gyulassy and S.K. Kauffmann, Nucl. Phys. A362, 503 (1981).

85. R. Stock, in Proceedings of the 5th High Energy Heavy Ion Study, LBL-12652, May 18-22, 1981.

86. Probability and Statistics in Particle Physics, A.G. Frodesen, O. Skjeggestad, and H. Tofte, Universitetsforlaget, Bergen (1979).

87. F. Sauli, Principles of Operation of Multiwire Proportional and Drift Chambers, CERN 77-07.

88. F. Sauli, CERN Report #77-09 (1977).

89. The author is indebted to James Miller for suggesting this approach.

90. Particle Properties Data Booklet, p. 81, Particle Data Group, Lawrence Berkeley Laboratory, (1980).

91. L.F.S. de Oliveira, University of California Ph.d thesis, LBL-8561, (1977).

92. This data has been generously provided by Dr. Dana Beavis of the University of California, Riverside. The author wishes to acknowledge Dr. Beavis for making this data available, as well as for valuable conversations regarding its interpretation.

93. A. Sandoval, R. Stock, H.E. Stelzer, R.E. Renfordt, J.W. Harris, J.P. Brannigan, J.V. Geaga, L.J. Rosenberg, L.S. Schroeder, and K.L. Wolf, Phys. Rev. Lett. 45, 874 (1980).

94. The author wishes to acknowledge a valuable conversation with Miklos Gyulassy concerning this model.

95. Quantum Mechanics, A.S. Davydov, translated, edited, and with additions by D. ter Haar, 2nd ed., London, Pergamon Press (1976).

96. J. Cugnon, D. Kinet, and J. Vandermeulen, Nucl. Phys. A379, 553 (1982).

FIGURE CAPTIONS

(1) Schematic diagram of a stellar interferometer using the Hanbury-Brown--Twiss technique. Two points P1 and P2 on a star of radius R are assumed to emit chaotic light. The light is detected at points A and B with the apparatus shown.

(2) Alternate paths for the detection of pions with $\vec{p}_1$ at $\vec{x}_1$ and $\vec{p}_2$ at $\vec{x}_2$. The pions are assumed to originate from an extended source encompassing $\vec{r}_1$ and $\vec{r}_2$.

(3) Plan view of the JANUS spectrometer system.

(4) Block diagram of the fast electronics used in conjunction with the JANUS spectrometer.

(5) Ion chamber calibrations for a variety of projectiles and beam energies.

(6) Schematic plan view of the JANUS spectrometer, along with the geometric method used in track recognition.

(7) Definition of angles used in determining momentum via the effective prescription.

(8) Vertical trajectories through the JANUS spectrometer, illustrating the effect of focusing by fringe fields.

(9) Momentum resolution for pions as a function of the laboratory momentum.

(10) Resolution for relative momentum and energy in the center-of-mass, as a function of the same quantities, again in the center-of-mass.

(11) a.) Fractional relative momentum resolution as a function of relative momentum and b.) Resolution for invariant relative momentum (used in the Gamow correction) as a function of relative momentum in the center-of-mass.

(12) Distribution in y and x of accepted events at the target as determined by traceback. Horizontal scale is in centimeters.

(13) Histogram of mean separation in y between two pion pairs at the target for real events and random (mixed) events, as determined by target traceback. Horizontal scale is in centimeters.

(14) Relation between total charge multiplicity Q and mean pion multiplicity $\langle M_{\pi}(Q) \rangle$, as given in Ref. 78. Also shown is schematic impact parameter scale.

(15) Pion multiplicity distributions from Ref. 92 for 1.8 A·GeV Ar+KCl events, for the JANUS 1 and 2 pion trigger requirements.

(16) Schematic illustration of area calculations by Monte Carlo techniques similar to two-pion background event generation. See Appendix E for further details.

(17) Invariant cross sections for $1\pi^-$ events as a function of center-of-mass (total) energy. The cross sections are scaled by an efficiency factor ϵ_1. The errors are statistical only.

(18) Invariant cross section for $2\pi^-$ events from Ar+KCl collisions as a function of total energy in the center-of-mass. The cross section is scaled by an efficiency factor ϵ_2. The errors are statistical only. Also shown is the corresponding laboratory momentum spectrum. This is the raw spectrum of events observed in JANUS, thus it has not been corrected for the acceptance. The arrow at E_{cm} = 500 MeV transforms to the arrow at p_{lab} = 700 MeV/c.

(19) As in Fig. 18, for Ne+NaF collisions.

(20) As in Fig. 18, for Ar+KCl$\rightarrow 2\pi^+ +X$.

(21) Profiles of a theoretical $C_2(q_o,q)$ with typical nuclear dimensions evaluated over the JANUS acceptance for relative momentum. The region on the left-hand-side of the ridge is kinematically forbidden.

(22) Projected correlation functions in q and q_o for Ar+KCl$\rightarrow 2\pi^- +X$, with no Gamow correction applied.

(23) As in Fig. 22, for $2\pi^+$ events.

(24) As in Fig. 22, for Ne+NaF$\rightarrow 2\pi^- +X$.

(25) Projected correlation functions in q and q_o for Ar+KCl$\rightarrow 2\pi^- +X$, with the Gamow correction applied.

(26) As in Fig. 25, for $2\pi^+$ events.

(27) As in Fig. 25, for Ne+NaF$\rightarrow 2\pi^- +X$.

(28) Monte Carlo calculations from Ref. 96 for production rates for pions and deltas for 1.8 A·GeV ^{40}Ca + ^{40}Ca collisions. Points are predictions assuming a Gaussian source in time. See Appendix G for further details.

(29) Confidence contours for fits to

$C_2(q_o,q) = 1 + \lambda e^{-q^2R^2/2 - q_o^2\tau^2/2}$ for the reaction

Ar+KCl→$2\pi^-$ +X. The inner contour represents the 68% likelihood contour; the outer band is the 95% likelihood contour.

(30) As in Fig. 29, for $2\pi^+$ events.

(31) As in Fig. 29, for Ne+NaF→$2\pi^-$ +X.

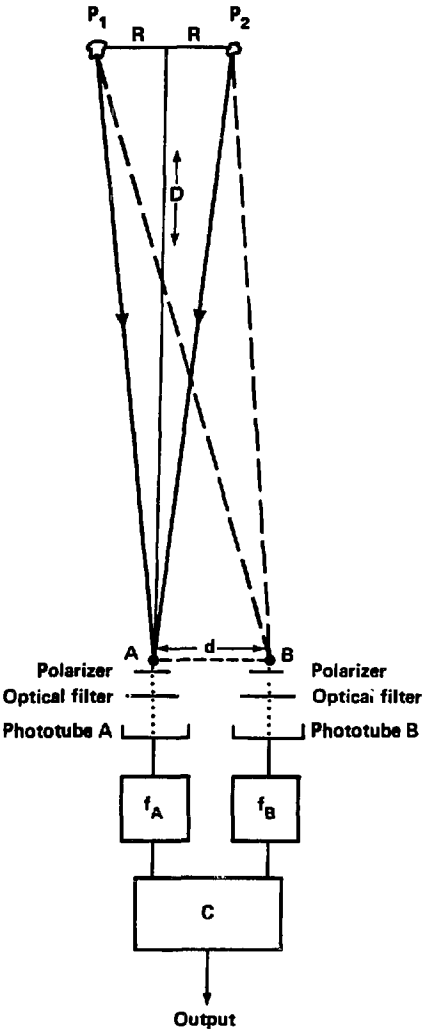
P1
R
R
P2
D
A
d
B
Polarizer
Optical filter
Phototube A
Polarizer
Optical filter
Phototube B
fA
fB
C
Output
XBL 827-7032

Figure 1

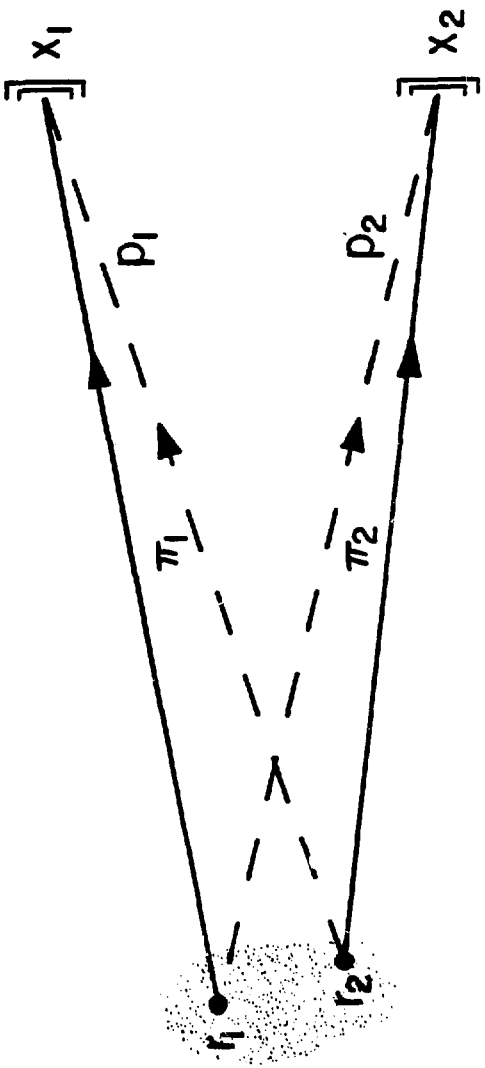

XBL 815-9836

Figure 2.

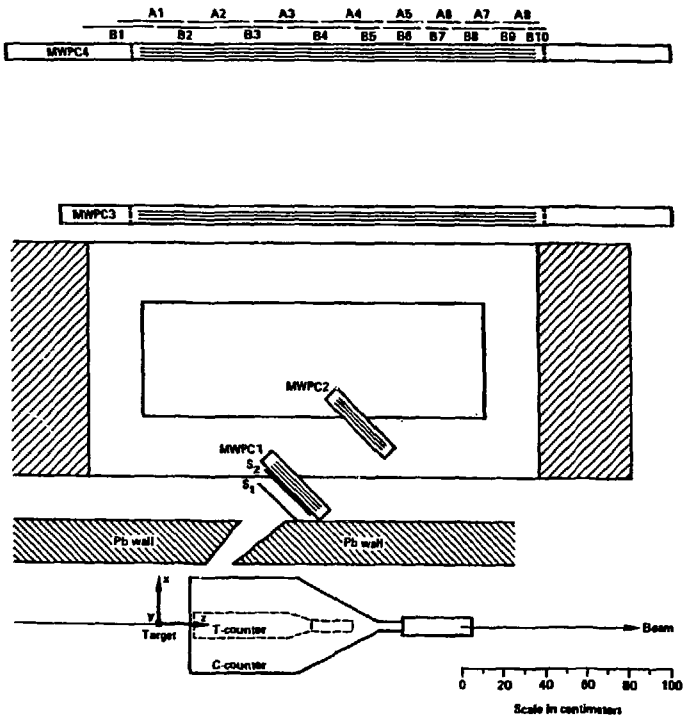
A1
A2
A3
A4
A5
A6
A7
A8
B1
B2
B3
B4
B5
B6
B7
B8
B9
B10
MWPC4
MWPC3
MWPC2
MWPC1
S_2
S_1
Pb wall
Pb wall
x
y
z
Target
T-counter
C-counter
Beam
0
20
40
60
80
100
Scale in centimeters
KBL 827-7089

Figure 3

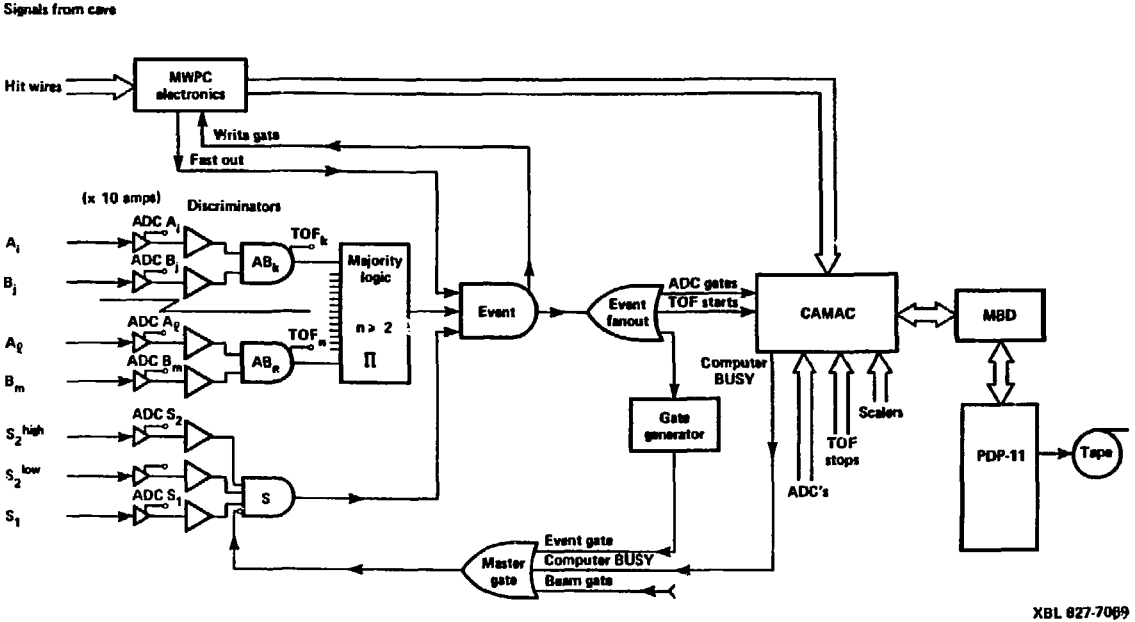
Signals from cave
Hit wires
MWPC electronics
Write gate
Fast out
(x 10 amps)
Discriminators
ADC A_i
ADC B_j
A_i
B_j
AB_k
TOF_k
ADC A_ℓ
ADC B_m
A_ℓ
B_m
AB_ℓ
TOF_ℓ
Majority logic
n > 2
Π
Event
Event fanout
ADC gates
TOF starts
CAMAC
MBD
Computer BUSY
Gate generator
Scalers
TOF stops
ADC's
PDP-11
Tape
ADC S_2
S_2^{high}
S_2^{low}
ADC S_1
S_1
S
Master gate
Event gate
Computer BUSY
Beam gate
XBL 827-7069

Figure 4

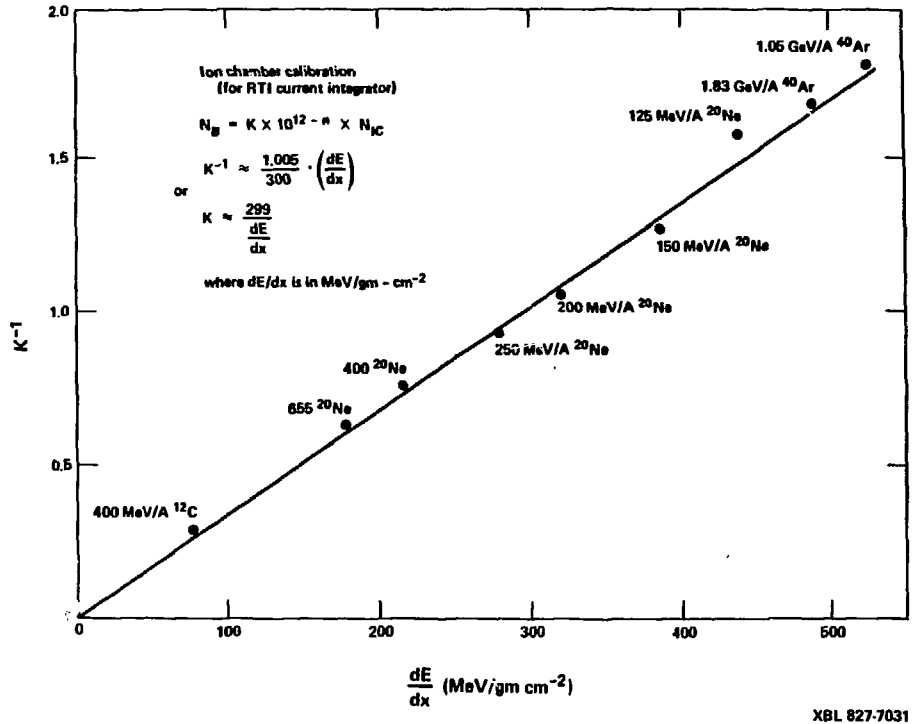

XBL 827-7031

Figure 5

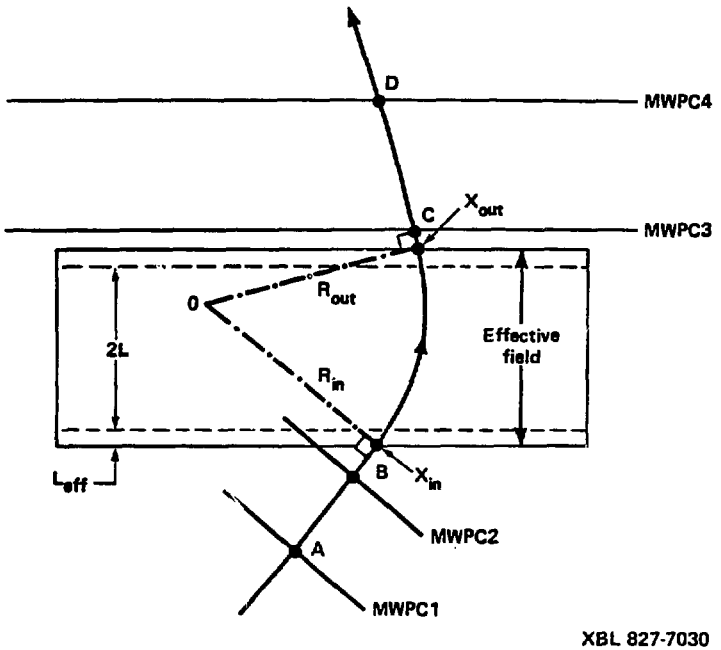
D
MWPC4
C
X_{out}
MWPC3
0
R_{out}
2L
Effective field
R_{in}
L_{eff}
B
X_{in}
MWPC2
A
MWPC1
XBL 827-7030

Figure 6

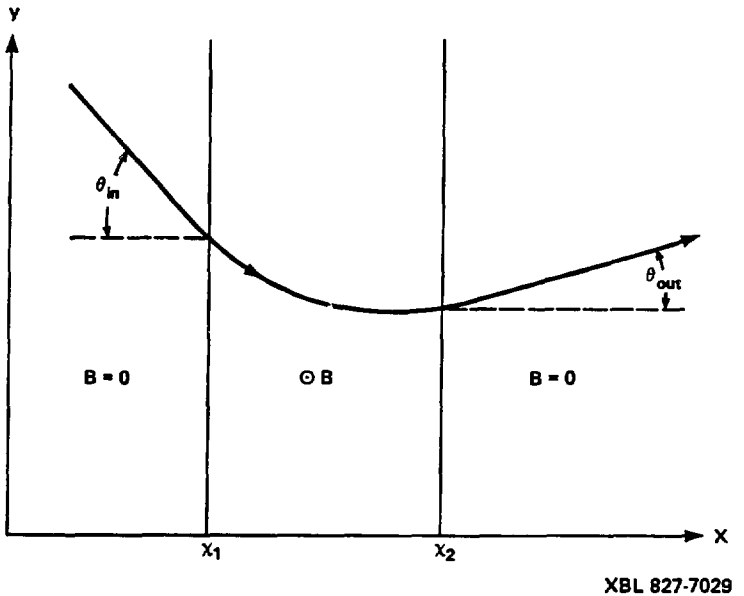

Figure 7

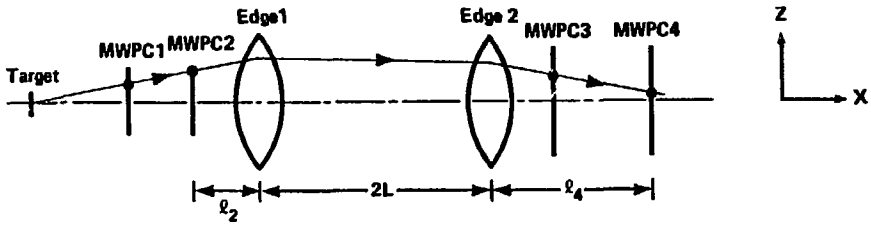

XBL 827-7087

Figure 8

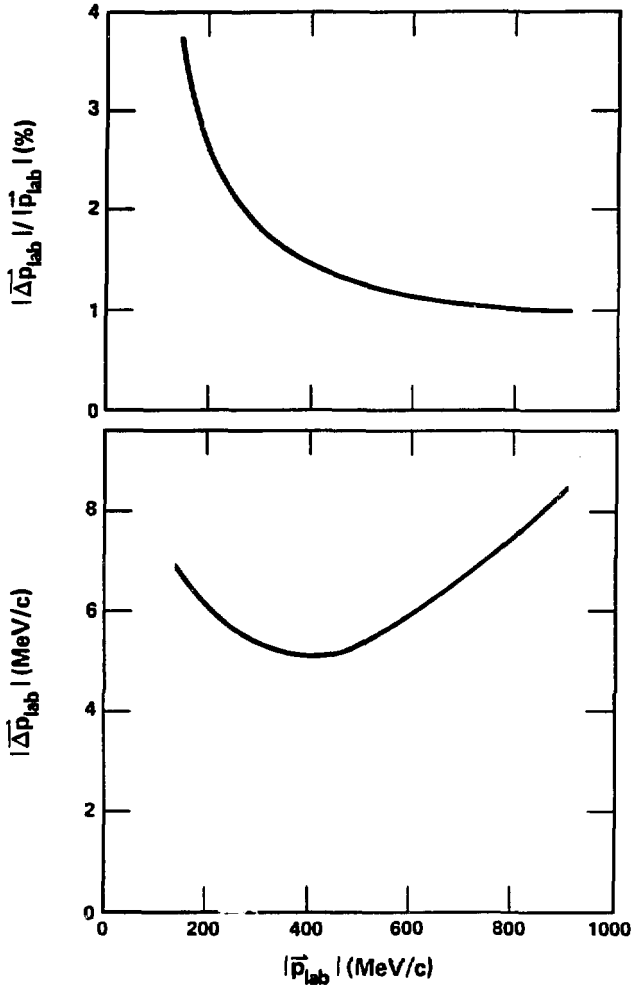
4
3
2
1
0
$|\vec{\Delta p}_{lab}|/|\vec{p}_{lab}|$ (%)
8
6
4
2
0
$|\vec{\Delta p}_{lab}|$ (MeV/c)
0
200
400
600
800
1000
$|\vec{p}_{lab}|$ (MeV/c)
XBL 827-7086

Figure 9

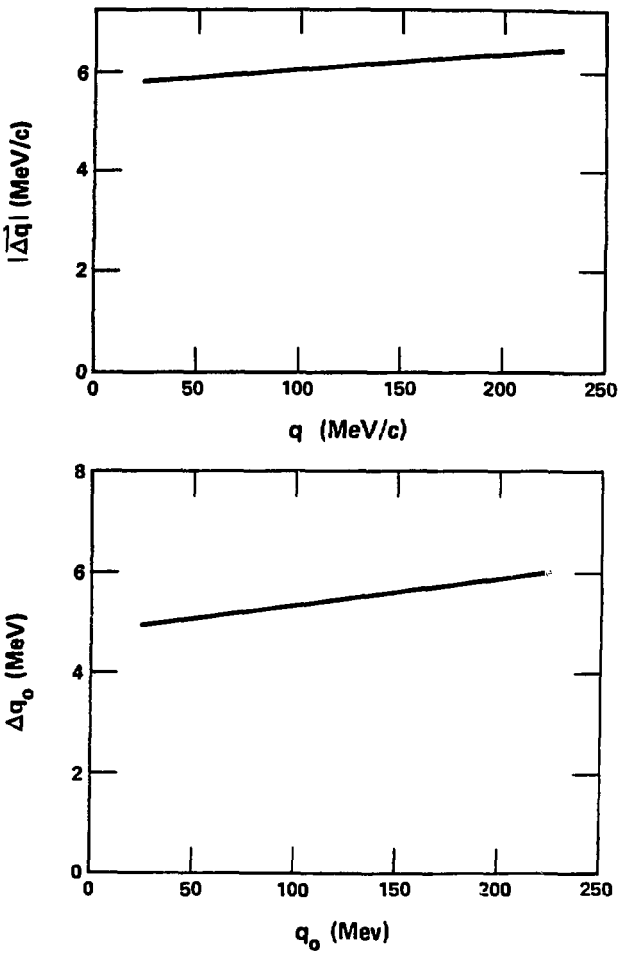
$|\vec{\Delta q}|$ (MeV/c)
0
2
4
6
0
50
100
150
200
250
q (MeV/c)
Δq_o (MeV)
0
2
4
6
8
0
50
100
150
200
250
q_o (Mev)
XBL 827-7090

Figure 10

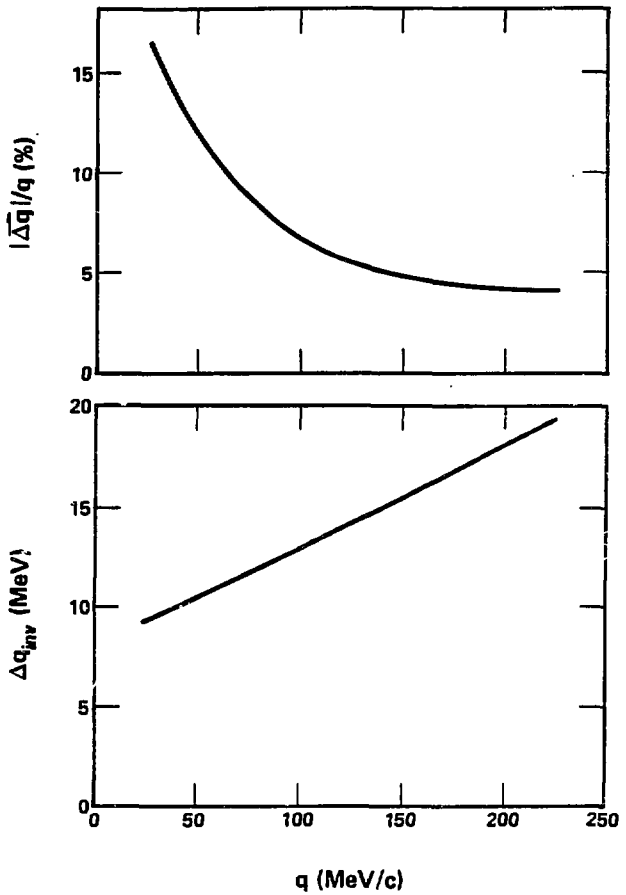
15
10
5
0
$|\bar{\Delta q}|/q$ (%)
20
15
10
5
0
Δq_{inv} (MeV)
0
50
100
150
200
250
q (MeV/c)
XBL 827-7091

Figure 11

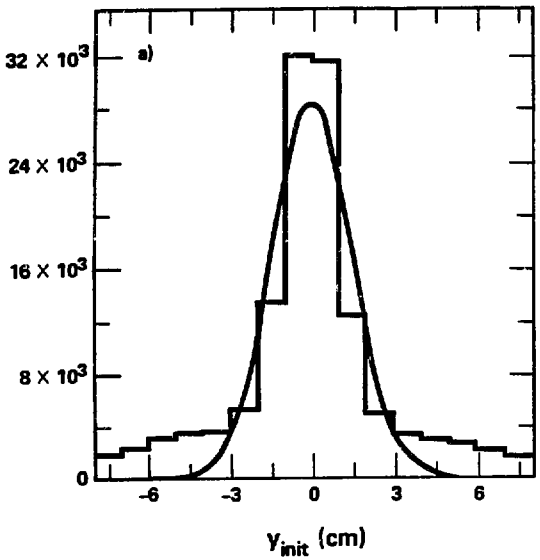

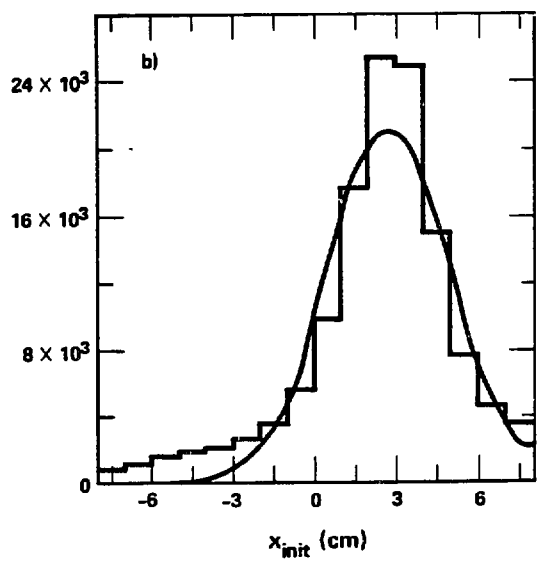

Figure 12 XBL 827-7085

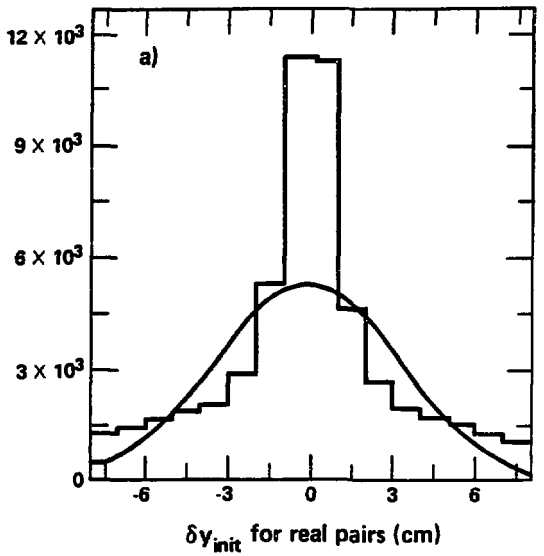

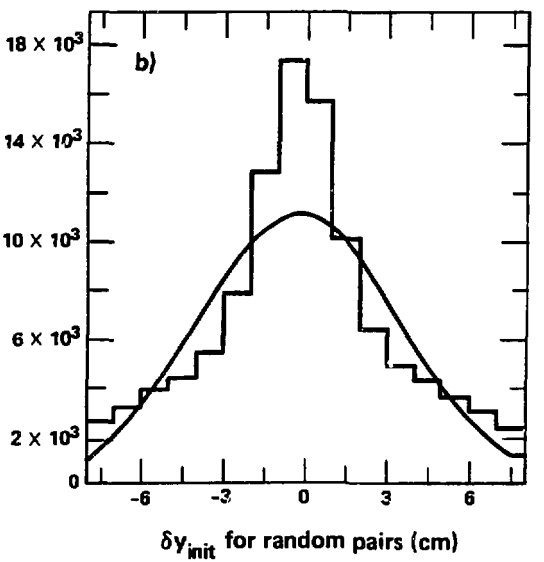

Figure 13 XBL 827-7078

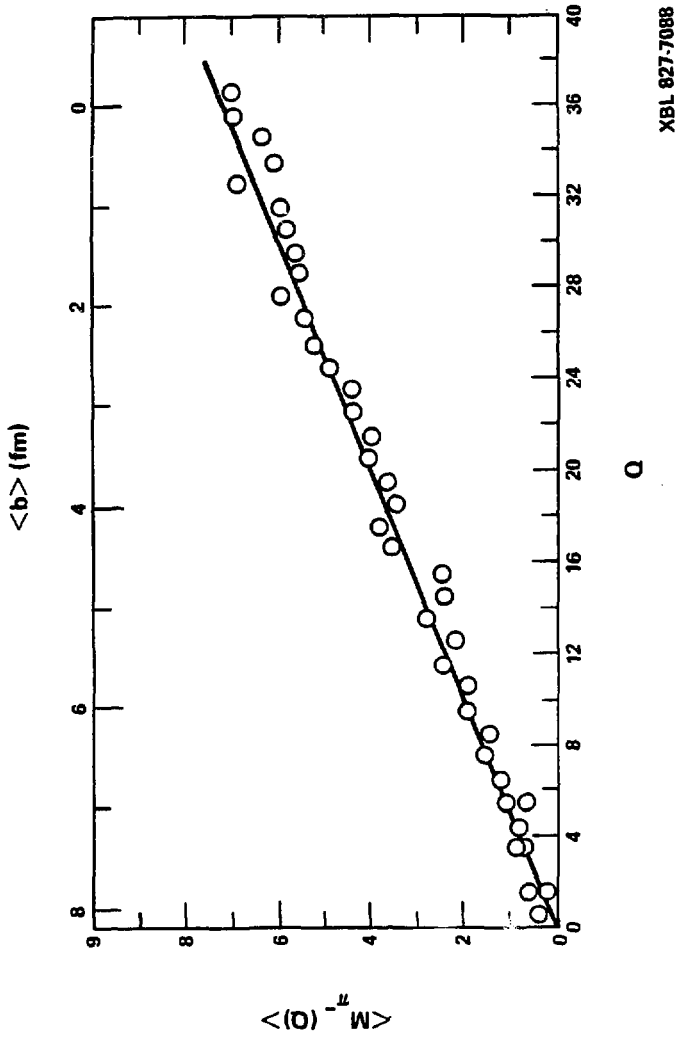

Figure 14

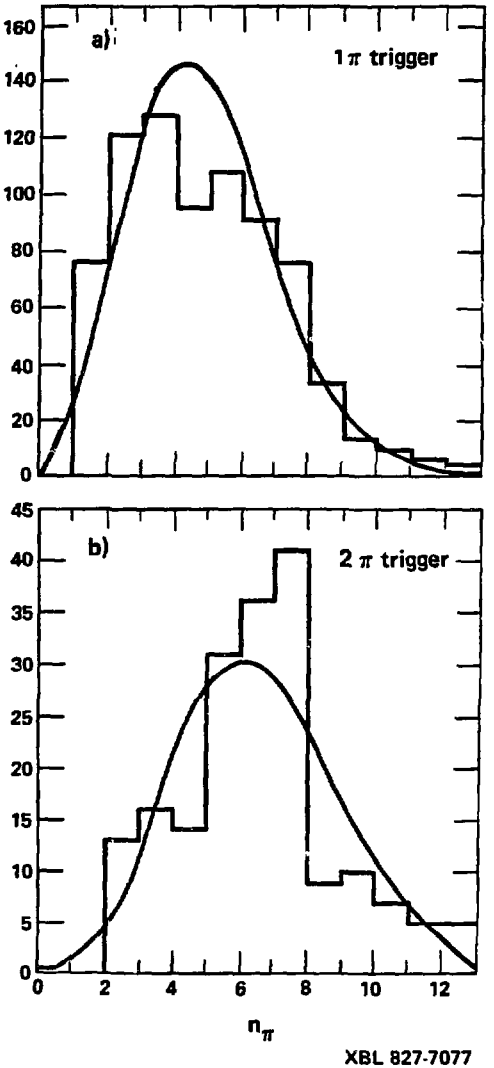
a)
1π trigger
160
140
120
100
80
60
40
20
0
b)
2π trigger
45
40
35
30
25
20
15
10
5
0
0
2
4
6
8
10
12
n_π
XBL 827-7077

Figure 15

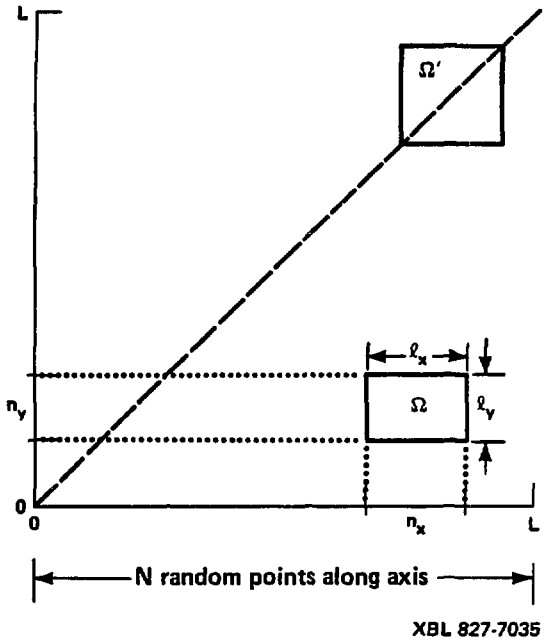
L
Ω'
ℓ_x
ℓ_y
Ω
n_y
0
0
n_x
L
N random points along axis
XBL 827-7035

Figure 16

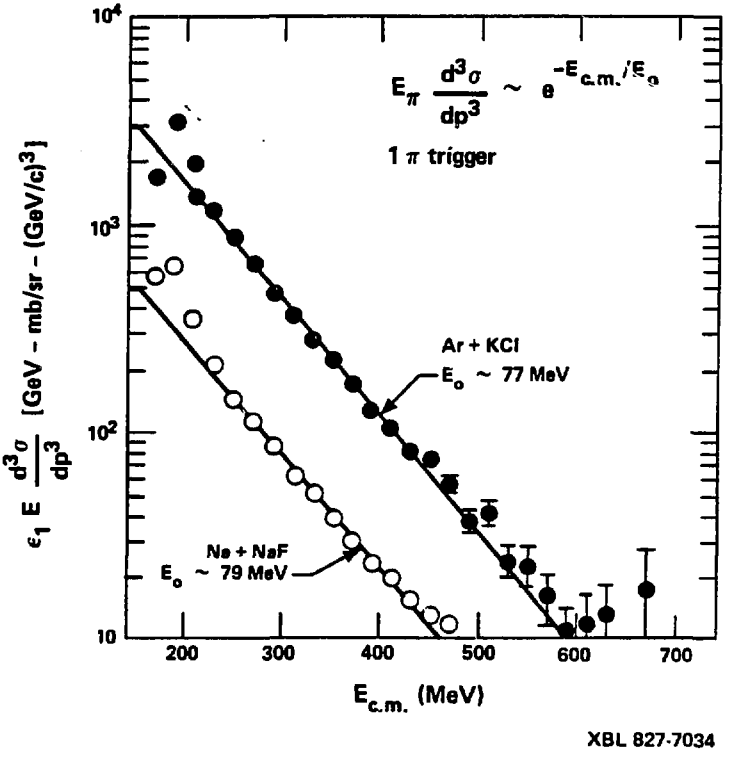
$E_\pi \frac{d^3\sigma}{dp^3} \sim e^{-E_{c.m.}/E_o}$
1 π trigger
Ar + KCl
E_o ~ 77 MeV
Ne + NaF
E_o ~ 79 MeV
$\epsilon_1 E \frac{d^3\sigma}{dp^3}$ [GeV - mb/sr - (GeV/c)^3]
$E_{c.m.}$ (MeV)
10^4
10^3
10^2
10
200
300
400
500
600
700
XBL 827-7034

Figure 17

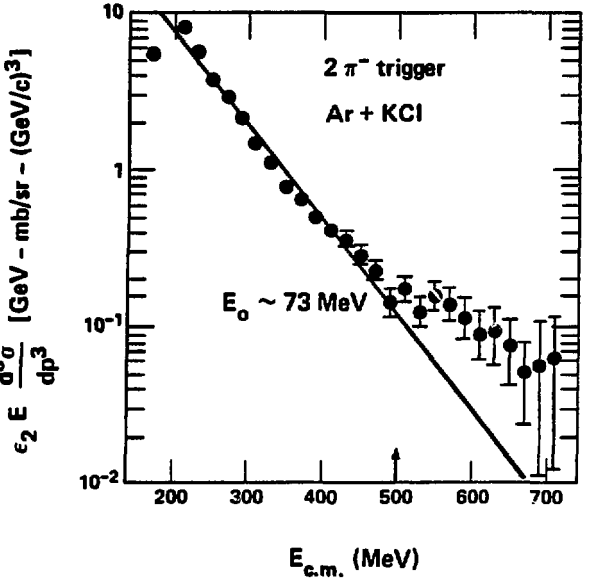

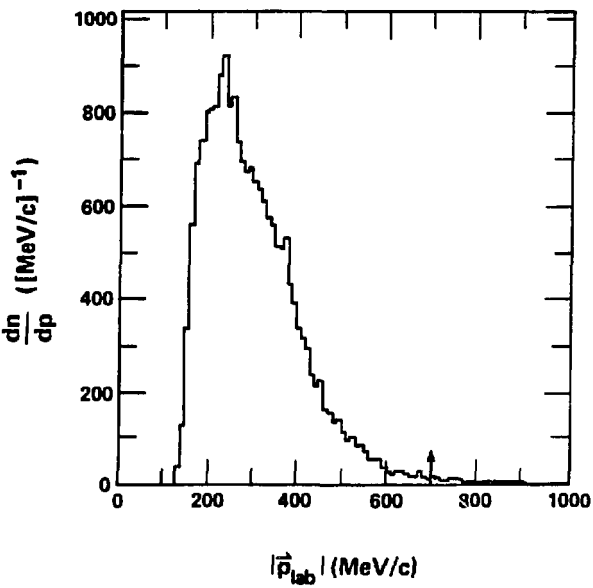

Figure 18 XBL 827-7072

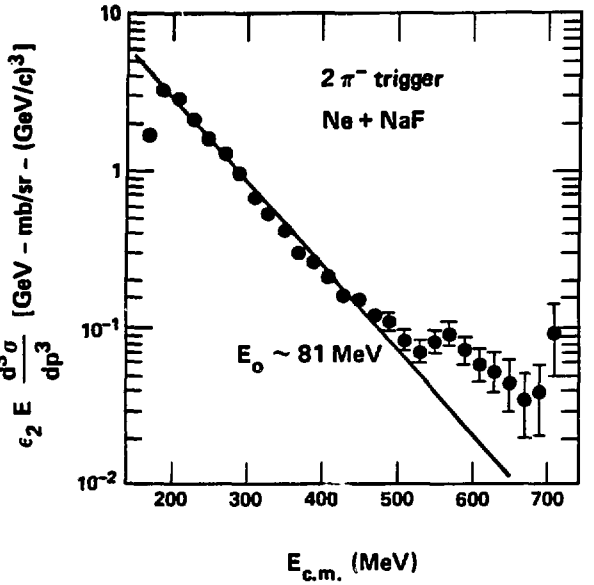

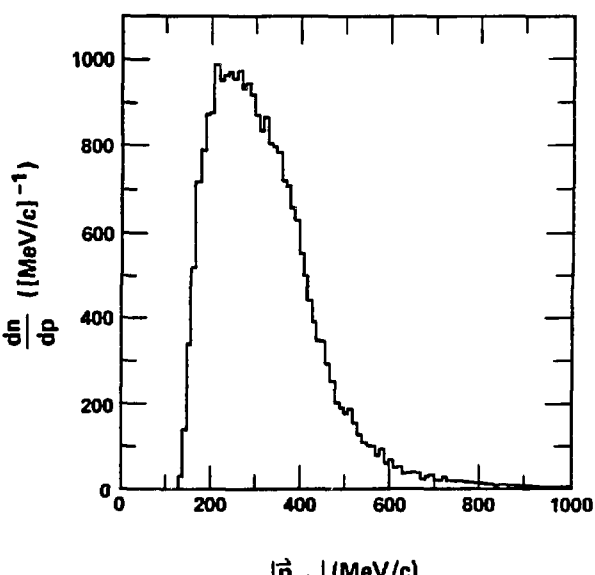

Figure 19 XBL 827-7073

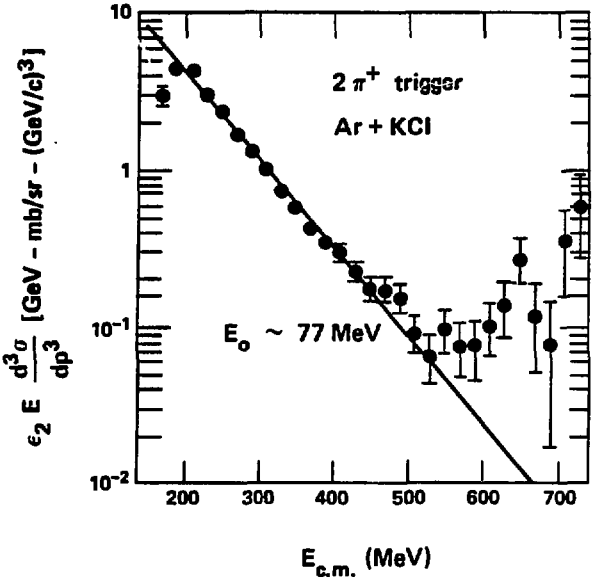

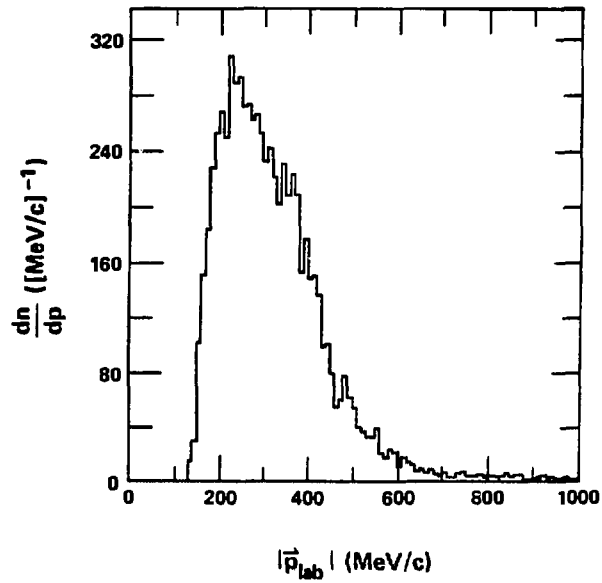

Figure 20 XBL 827-7074

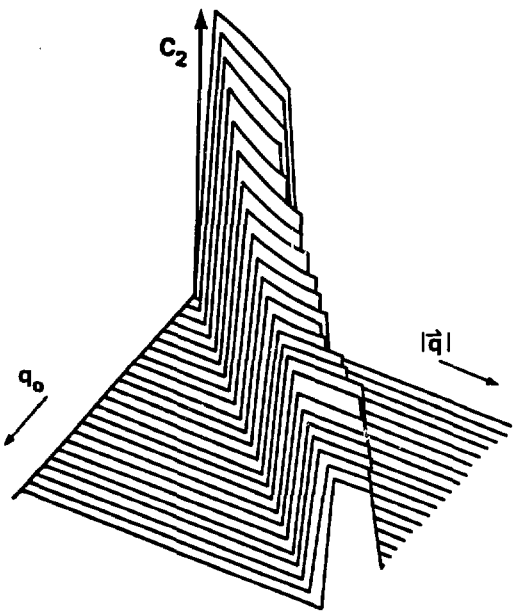

Figure 21

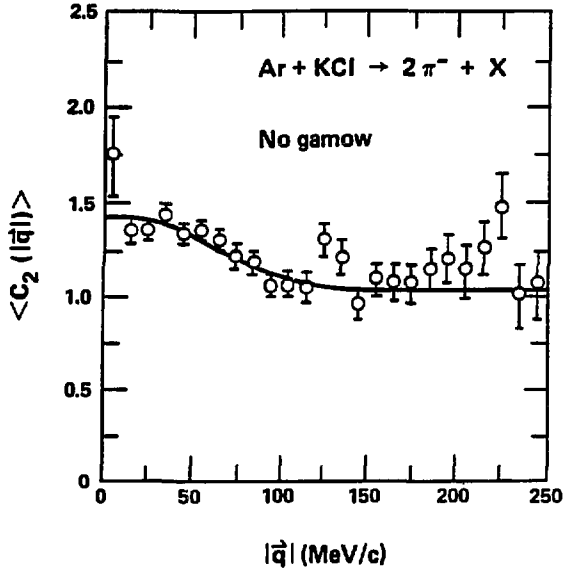

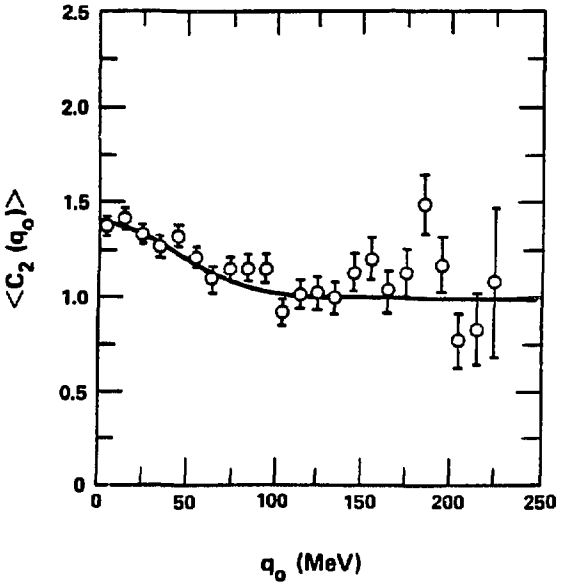

Figure 22 XBL 827-7026

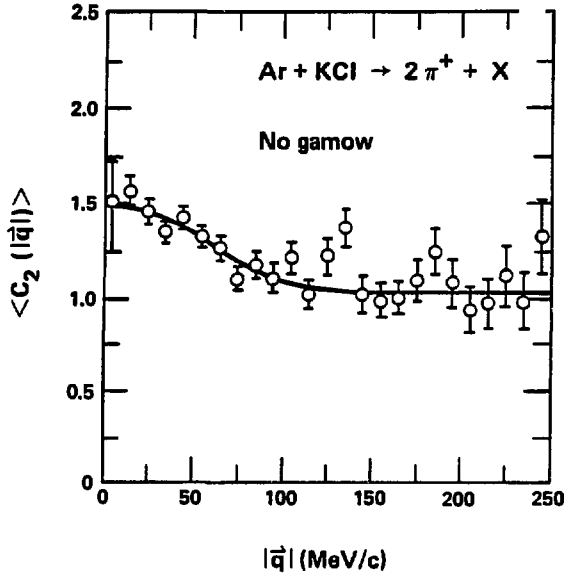

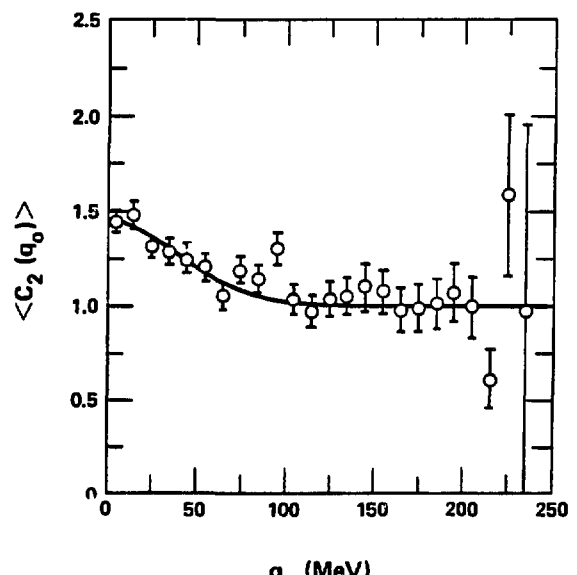

Figure 23 XBL 827-7027

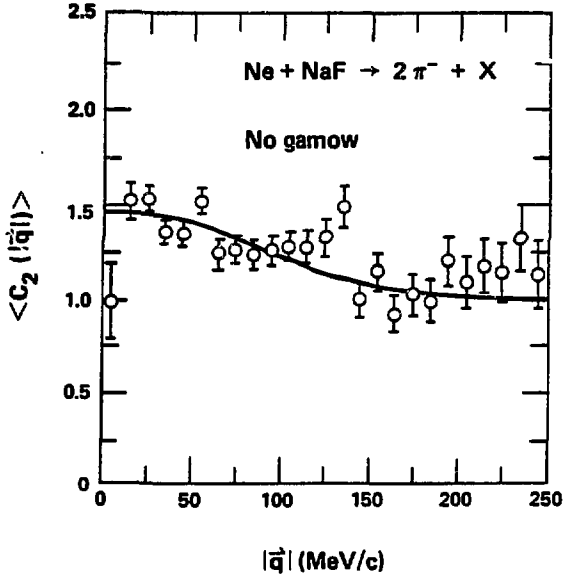

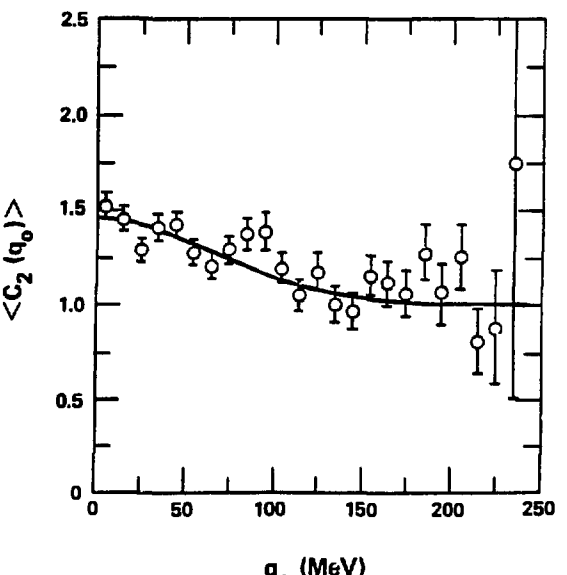

Figure 24 XBL 827-7028

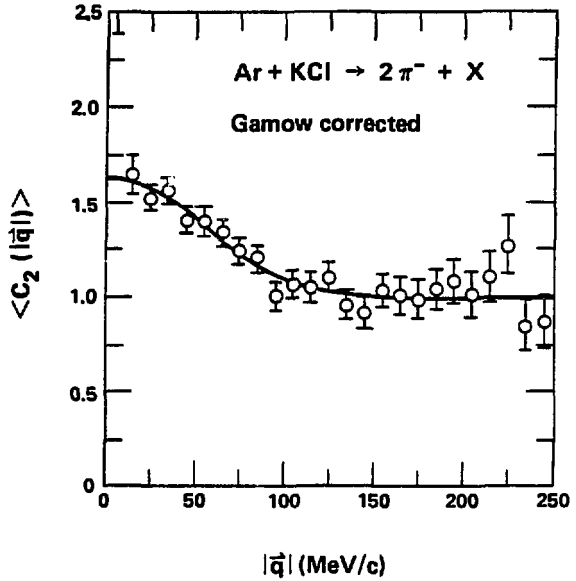

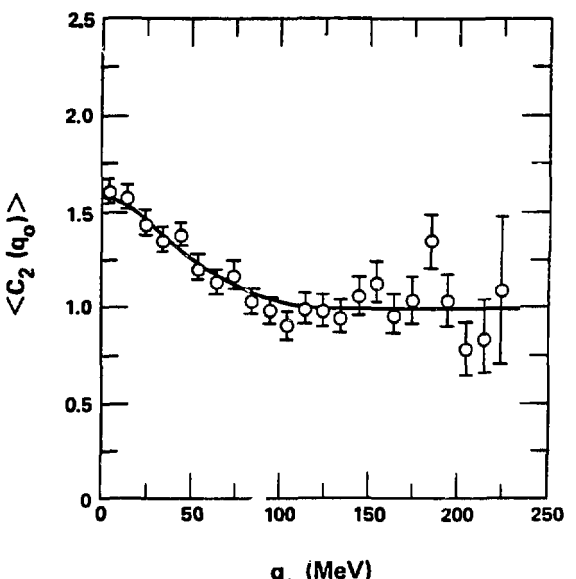

Figure 25 XBL 827-7023

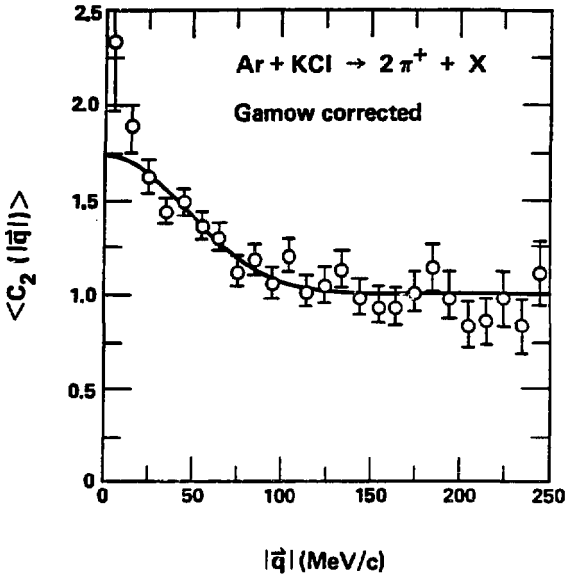

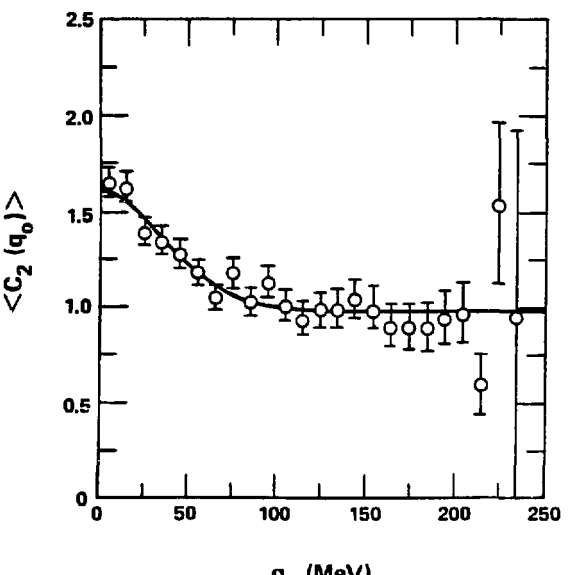

Figure 26 XBL 827-7025

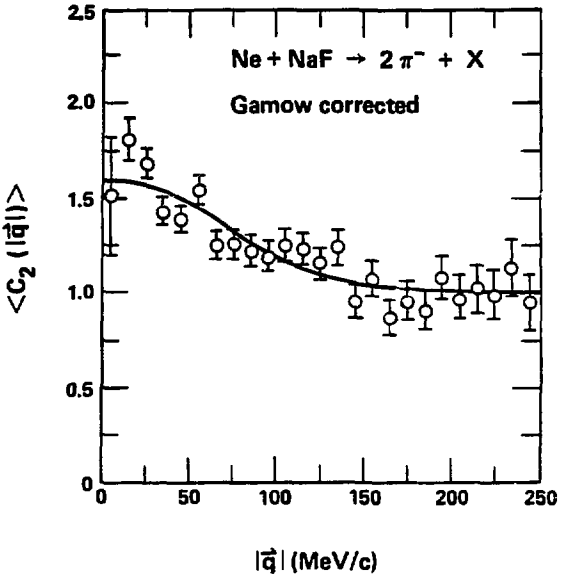

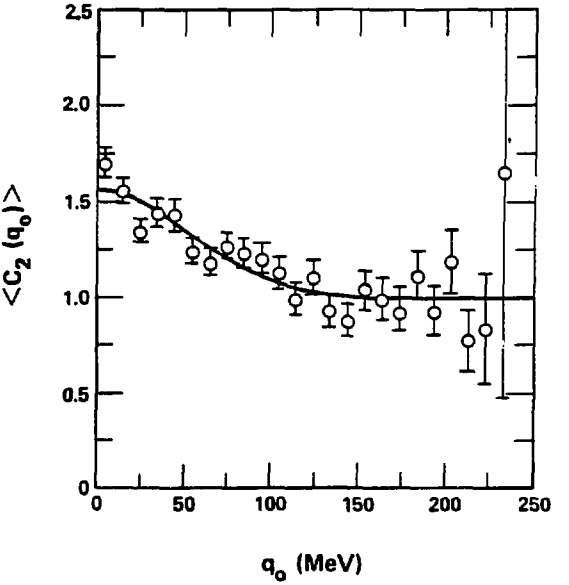

Figure 27 XBL 827-7024

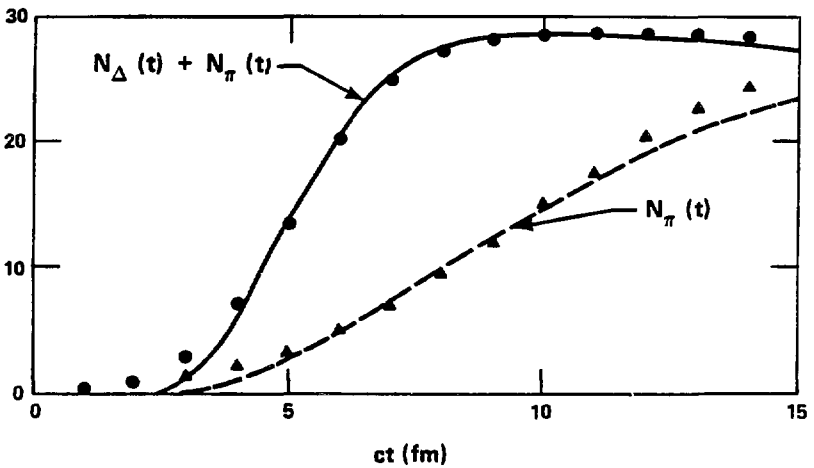

XBL 827-7021

Figure 28

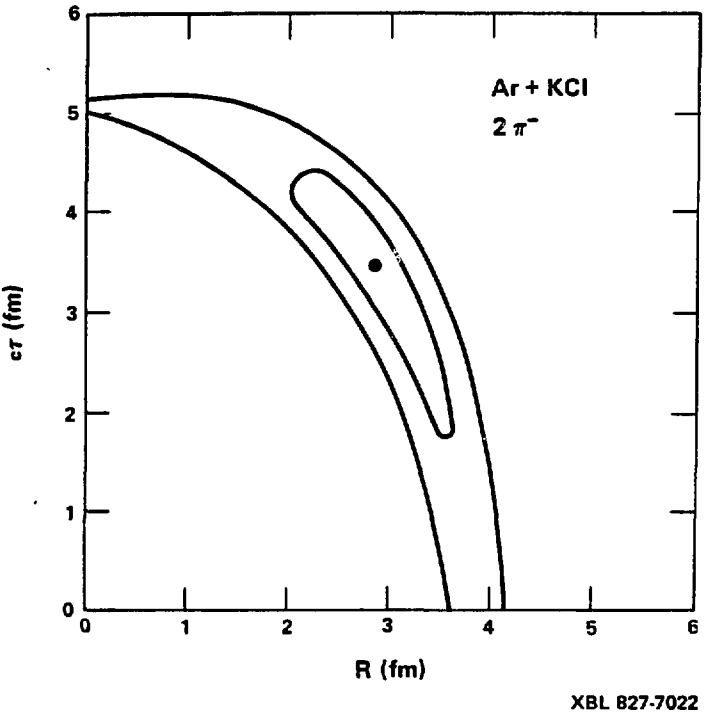

Figure 29

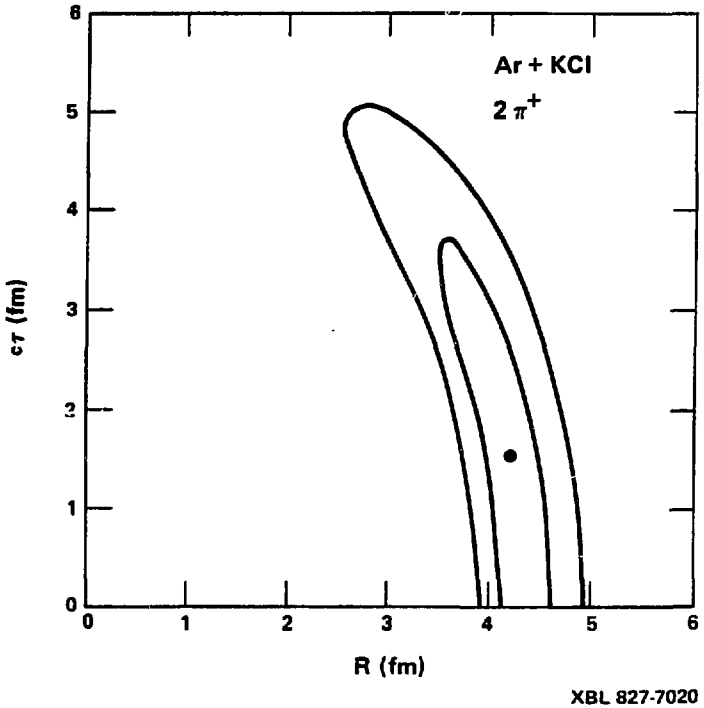

Figure 30

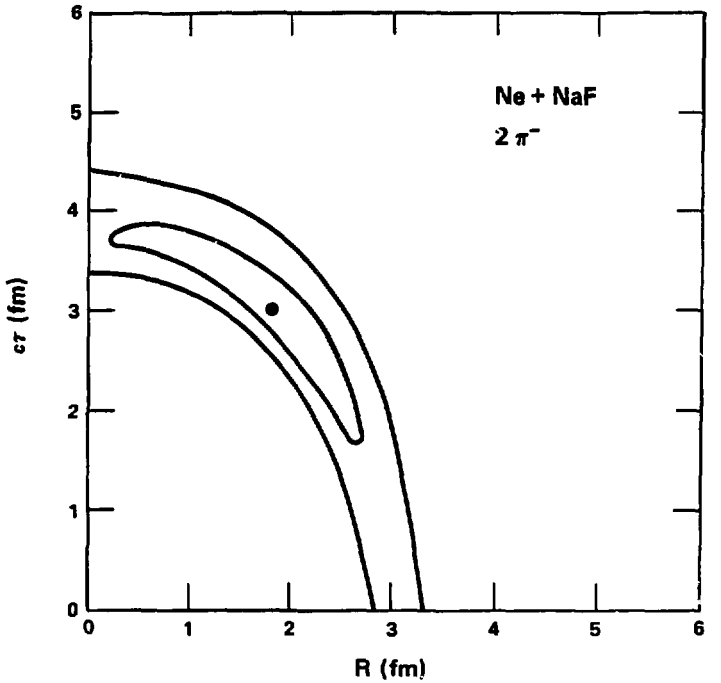

Figure 31